Signal Integration and Diversification by Melanopsin-Expressing Retinal Ganglion Cells

Signal Integration and Diversification by Melanopsin-Expressing Retinal Ganglion Cells

A dissertation presented

by

Alan Joseph Emanuel

to

The Division of Medical Sciences

in partial fulfillment of the requirements

for the degree of

Doctor of Philosophy

in the subject of

Neurobiology

Harvard University

Cambridge, Massachusetts

April 2016

Dissertation Advisor: Professor Michael Tri Hoang Do Alan Joseph Emanuel

Signal Integration and Diversification by Melanopsin-Expressing Retinal Ganglion Cells

Abstract

There are three classes of light-sensing cells in the mammalian retina: rods, cones, and intrinsically photosensitive retinal ganglion cells (ipRGCs). This dissertation focuses on the signals generated by the ipRGCs, which are important for the regulation of many non-image-forming visual functions such as regulation of the circadian clock, pupillary light reflex, sleep, locomotor activity, and hormone levels. Dysregulation of these functions can have profound effects on health. How ipRGCs regulate these functions remains incompletely understood because many of their basic properties have not yet been established. To better understand ipRGCs, I conducted a quantitative electrophysiological examination of their light responses within the *in vitro* mouse retina.

Chapter 2 presents evidence that melanopsin, the light-sensing pigment that initiates phototransduction within ipRGCs, has three stable states that are interconverted by light. Two of these states are silent and have distinct spectral sensitivities, which allows ipRGCs to integrate over a relatively broad range of wavelengths. The stability of the active state results in the production of a persistent response that long outlasts the offset of the stimulus and allows ipRGCs to integrate light over time. Most light stimuli, including short-wavelength and white light produce a large fraction of the active state and its associated persistent response. In contrast, long-wavelength light produces a much smaller fraction of the active state and can be used to decrease the persistent response. The effects of melanopsin tristability appear to be particularly suited for the functions regulated by ipRGCs. These effects are absent in other known photoreceptors, which have pigments with only one or two stable states.

IpRGC phototransduction persists for minutes even after illumination has ceased because the signaling state of melanopsin is thermally stable. In Chapter 3, I describe experiments that examine how this persistence influences two fundamental aspects of ipRGC function: activation and adaptation. I found that increased persistence is associated with ipRGC activation that encodes a narrower band of light intensities. Thus, although persistence endows ipRGCs with temporal integration, it does so at the cost of dynamic range. In addition, persistence drives adaptation to desensitize the cell. Accordingly, acutely

decreasing the persistent response with long-wavelength light can result in a subsequent recovery of sensitivity. However, this effect is highly variable across the population; some cells show greater desensitization from the long-wavelength light than resensitization from its reduction of the persistent response. Therefore, the balance of activation and adaptation differs among ipRGCs, such that light history may diversify the signals generated by the population.

There are multiple subtypes of ipRGCs, but even a single subtype regulates many distinct functions. In Chapter 4, I describe a systematic approach for examination of the diversity in the biophysical parameters governing ipRGC signaling, including phototransduction, synaptic input, passive membrane properties, and spike generation. Comparison of these parameters across cells revealed a large degree of heterogeneity both between and within two morphologically-defined ipRGC subtypes. The diversity in ipRGC signal generation does not appear to divide among ipRGCs that project to different brain regions that control distinct functions; ipRGCs that project to the hypothalamus have diverse physiological properties that are highly overlapping with the ipRGCs that project to the pretectum. This suggests that functions driven by both areas have access to information from ipRGCs with a similar, broad range of characteristics.

In summary, the research described within this dissertation has revealed that visual pigments can be tristable in physiological conditions and this tristability has unique consequences for signal generation. Furthermore, it has provided insight into the high degree of biophysical diversity that can be present even within a single, molecularly-defined type of neuron. These findings contribute to the emerging understanding of ipRGCs and their distinctions from the classical rod and cone photoreceptors.

Table of Contents

Acknowledgments

I am incredibly grateful for the many people who have helped make my progress to and through my time in graduate school enjoyable and productive.

I would like to thank Michael Do. He is an incredible mentor and I have been very lucky to be part of lab during its nascent period. I admire his ability to think clearly and know where to push to get the best out of a research project. I also greatly appreciate that he cares deeply about not only the productivity, but also the well-being of the people in his lab.

I would also like to thank the members of the Do lab, past and present: Ryan Adams, Michael Brown, Greg Bryman, Verda Bursal, Elizabeth Egan, Molly Kwiatkowski, Andy Liu, Wendy Liu, and E.S. Milner. These people have always given me high-quality feedback and support and have made the Do lab an invigorating place to spend time in the last few years.

I would like to thank the members of my dissertation advisory committee, Drs. Gary Yellen, Rachel Wilson, and Clifford Saper for the highly valuable advice they have provided as I have progressed through my time in graduate school.

Thank you to my dissertation examination committee, Drs. David Berson, Clint Makino, Joshua Sanes, and Clifford Saper, for agreeing to read this thesis.

I also want to acknowledge Sue Ritter, who was my undergraduate mentor at Washington State University, for her mentorship. Sue nurtured my scientific side and gave me an extraordinary opportunity in allowing me to pursue my own project as a first-year undergraduate. While providing this option for me to take ownership of my research seems risky to me at a time when I had no idea what I was doing, I learned so much and will always be grateful for her trust and mentorship during those years.

My classmates and friends in the Program in Neuroscience have made graduate school some of the best years of my life, and I thank them for that.

My family, including my parents, Jeff Emanuel, Stephanie Lyon, and Amelia Webster, my brothers, George and Peter Emanuel, as well as members of my extended family has been highly supportive throughout my life. I greatly appreciate the time that they have made for me and I wish I lived closer so that I could visit more often.

Lastly, I would like to thank my wonderful wife, Kaori, for her love and support. She helps me focus on the important things in life and I am grateful for every moment I get to spend with her.

Chapter 1: Introduction

Alan Joseph Emanuel

The Retina, the Site of the First Steps of Mammalian Vision

Light plays an immensely important role in everyday life. Our actions are guided by the ability to sense light because it allows us to perceive the location of objects in space, communicate using visual signals, and detect the time of day. To accomplish these tasks we must transduce light into a neural signal. This is achieved, in humans and other mammalian species, exclusively within the eye. A thin piece of neural tissue, called the retina, sits at the posterior end of the eye. This tissue is made up of highly-organized layers of neural cell bodies and processes. The conversion of light into electrical signals for conscious vision begins with the rod and cone photoreceptors in the most posterior layer of the retina. These cells express specialized G protein-coupled receptors called opsins that associate with a retinaldehyde derivative chromophore molecule (reviewed by Palczewski, 2006). The absorption of a photon by this chromophore molecule results in its isomerization and an ensuing change in the conformation of the opsin (Palczewski et al., 2000). This activates a G protein signaling cascade which, in rods and cones, culminates in the closing of cyclic-guanine-monophosphate-gated channels to produce a hyperpolarization of the cell's membrane potential (reviewed by Yau and Hardie, 2009).

Signals evoked by this hyperpolarization propagate through the layers of the retina. Downstream of rods and cones, horizontal cells, bipolar cells, and amacrine cells serve as interneurons in the retina. These interneurons process and relay light responses to retinal ganglion cells (RGCs), which are situated in the most anterior cell layer and are the only output neurons of the retina. RGCs convert their synaptic inputs into action potentials that are propagated along their axons, which form the optic nerve, to convey processed information about light to the brain.

The retina is composed of cells of many different types, even within the broadly-defined classes just mentioned (Masland, 2012). For example, in human eyes, in addition to one type of rod photoreceptor there are three types of cone photoreceptors, which allow us to see in rich colors due to the differences in the spectral absorbance properties of the opsins they express (Nathans et al., 1986). In rodents and rabbits, where retinal cell types have been studied most intensively using modern techniques, there are 2 cone types, 2 horizontal cell types, approximately 12 different bipolar cell types (Helmstaedter et al., 2013; Masland, 2012), approximately 30 amacrine cell types (Masland, 2012), and

at least 20 different RGC types (Baden et al., 2016; Sanes and Masland, 2015). There are highly specific connections between these diverse cells that allow them to extract salient features about the visual environment and send processed information to the brain.

The subject of this dissertation is a type of RGC that produces an intrinsic response to light in addition to receiving synaptic inputs from the aforementioned retinal circuitry. In all mammalian species studied, these intrinsically photosensitive retinal ganglion cells (ipRGCs) constitute a small fraction of the total RGC population and, due to the large size of their overlapping dendritic fields, cover the retina; the notable exception is the fovea, the site of high-acuity vision in humans and other primates, which excludes all RGCs (Berson et al., 2010; Dacey et al., 2005; Hannibal et al., 2002; Hattar et al., 2002; Liao et al., 2016; Morin et al., 2003). IpRGCs have been established as critically important regulators of a number of visual functions. Most of these functions are subconscious and non-image-forming, such as the regulation of the circadian clock. Even though these functions are subconscious, their proper regulation is vitally important. For example, dysregulation of the circadian clock has been implicated in higher incidence of cancer as well as metabolic and psychiatric disorders (reviewed by Takahashi et al., 2008). Development of an understanding of how ipRGCs encode and send information about light to the brain, which is the goal of this thesis, is essential for understanding how these visual functions normally operate. The experiments described in this dissertation are designed with a quantitative and biophysical approach that provides mechanistic insights into ipRGC phototransduction.

Melanopsin, the Light-Sensor of IpRGCs

IpRGCs express the protein, melanopsin, to capture photons and initiate phototransduction. Melanopsin belongs to the opsin class of G protein-coupled receptors (Provencio et al., 1998; Provencio et al., 2000), and uses 11-*cis* retinal as its chromophore. In this dissertation, the combination of the opsins and chromophore will also be referred to as pigments.

Melanopsin was determined to be the light sensor of ipRGCs through a series of influential experiments. Soon after its expression in the mammalian retina was discovered (Provencio et al., 2000), it was found to be expressed within ganglion cells that project directly to the suprachiasmatic nucleus of the hypothalamus (SCN), the site of the circadian clock (Gooley et al., 2001). It was then demonstrated

that the ganglion cells that express it are intrinsically photosensitive because they depolarize in response to light even when all synaptic transmission is eliminated (Berson et al., 2002). Furthermore, visual behaviors that persisted in rod- and cone-deficient mice were completely absent when these animals were crossed with melanopsin knockout mice (Hattar et al., 2003; Lucas et al., 2003; Mrosovsky and Hattar, 2003; Panda et al., 2002). These findings indicate that melanopsin is necessary for visual functions driven by the intrinsic photosensitivity of these ganglion cells. In addition, heterologous expression of melanopsin makes a number of cell lines and types photosensitive (Bailes and Lucas, 2013; Melyan et al., 2005; Panda et al., 2005; Qiu et al., 2005; Tsunematsu et al., 2013; Ye et al., 2011). Another line of evidence that indicates melanopsin is the photoreceptor of ipRGCs is that the spectral sensitivity of purified melanopsin (Matsuyama et al., 2012; Walker et al., 2008) is similar to that of ipRGCs (Berson et al., 2002; Dacey et al., 2005; Emanuel and Do, 2015), that of functions driven by light in the absence of rod and cone photoreceptors (Freedman et al., 1999; Hattar et al., 2003), and that of cells photosensitized with expression of melanopsin (Bailes and Lucas, 2013; Melyan et al., 2005; Panda et al., 2005; Qiu et al., 2005).

Despite melanopsin's discovery in a vertebrate species (*Xenopus laevis*), the sequence of melanopsin has higher homology to rhabdomeric opsins, which are typically found in invertebrates, than to ciliary opsins, which are typically found in vertebrates (Provencio et al., 1998; Provencio et al., 2000). The phototransduction cascade that converts photon absorptions by melanopsin into an electrical signal is also thought to be similar to that of rhabdomeric photoreceptors, such as those of *Drosophila* and *Limulus*. Although the identity of the G protein has yet to be determined, it appears to be of the $G_{q/11}$ family (Chew et al., 2014; Graham et al., 2008; Panda et al., 2005). In mice, phospholipase C acts as a second messenger (Graham et al., 2008; Xue et al., 2011) and the cascade culminates in the opening of cation channels (Perez-Leighton et al., 2011; Sekaran et al., 2007; Xue et al., 2011) and a depolarization of the membrane voltage that can drive spiking and calcium signaling (Berson et al., 2002; Sekaran et al., 2003). By contrast, the ciliary opsins in rod and cone photoreceptors use a cascade that relies on the closing of cyclic-nucleotide-gated channels to produce a hyperpolarization in response to light (reviewed by Yau and Hardie, 2009).

While the signaling cascade of melanopsin in ipRGCs differs from that of opsins in rods and cones, there are a number of similarities in the light responses of these three photoreceptors. The intensity-response relations are fit well with the Michaelis-Menten equation in all three (Do et al., 2009; Luo et al., 2008), and the single-photon response of ipRGCs, measured directly and using fluctuation analysis on dim-flash responses that are in the linear range of the intensity-response relation, is approximately 1 pA (Do et al., 2009). This is two-fold larger than the single-photon response amplitude of mouse rod photoreceptors (Chen et al., 1999). However, ipRGCs are approximately six orders of magnitude less sensitive than rods, which is largely due to the difference in pigment density of these cells; rods contain 10^8 rhodopsin molecules per cell, whereas ipRGCs contain approximately 10^4 melanopsin molecules per cell (Do et al., 2009; Luo et al., 2008). Another similarity between ipRGC and rod and cone phototransduction is the nature of response adaptation. The intrinsic light response of ipRGCs adapts strongly (Do and Yau, 2013; Wong et al., 2005); the steady response to ongoing light exposure is only a small fraction of the initial transient response. Furthermore, the sensitivity of ipRGCs decreases on top of a background light in a manner that is well-described by the Weber-Fechner relation (Do and Yau, 2013), identical to the change in sensitivity due to adaptation in rods and cones (Shapley and Enroth-Cugell, 1984). This similarity in phototransduction between these photoreceptors is quite remarkable given that they use very different transduction cascades. Indeed, there are also differences; the melanopsin-driven single-photon response is much slower (Do et al., 2009), and adaptation of ipRGC phototransduction is still apparent in the absence of calcium (Do and Yau, 2013).

A striking difference between rhabdomeric and ciliary photoreceptors is that the opsins in rhabdomeric cells are bistable; upon photon absorption, the active, meta, state of rhabdomeric opsins remains bound to the all-*trans* retinal isomer and can continue to signal for hours (Hillman et al., 1983). Subsequent photon absorptions by the active state result in re-isomerization of its chromophore back to 11-*cis* retinal, returning the opsin to its ground state (Hillman et al., 1983). The ground and active states are often spectrally distinct, so it is possible to use spectrally-filtered light to produce an equilibrium that is dominated by one or the other. In contrast to rhabdomeric opsins, ciliary opsins dissociate from the isomerized chromophore, a process known as bleaching (Saari, 2000). Reconstitution of these opsins

requires re-isomerization of the chromophore molecule in accessory tissues. Bleaching and bistability are not mutually exclusive; some opsins are intermediate, with a relatively thermally stable active state that bleaches over time, such as butterfly rhodopsin (Bernard, 1983).

It was suggested that melanopsin is also bistable because its highest homology is with the rhabdomeric opsins and because ipRGCs are far from the major known source of chromophore (Mure et al., 2009; Mure et al., 2007; Provencio et al., 1998). However, the evidence for melanopsin bistability was not conclusive. Light responses in brain areas immediately downstream from ipRGCs appear to be potentiated with long-wavelength light exposure, which suggests that long-wavelength light shifts thermally-stable active melanopsin to an inactive state (Mure et al., 2007), but when ipRGC spiking was measured in responses to the same stimuli, such potentiation was not observed (Mawad and Van Gelder, 2008). It has been suggested that mouse melanopsin is resistant to bleaching (Sexton et al., 2012), but also that mammalian melanopsin has a relatively loose association with its chromophore (Tsukamoto et al., 2015). The sensitivity of the intrinsic response of ipRGCs can also be increased by exposure to 11-*cis* retinal, suggesting that melanopsin is bleachable (Do et al., 2009; Fu et al., 2005). To understand the signals generated by ipRGCs, it is necessary to know the properties of melanopsin. Therefore, the first part of my dissertation, described in Chapter 2, examines the question of whether melanopsin in mouse ipRGCs has bistable properties. Surprisingly, we found evidence that, unlike any other known opsin, melanopsin in ipRGCs is interconverted between three stable states with light and is, thus, tristable and not bistable (Emanuel and Do, 2015). One of these three states is active and produces a persistent response that allows ipRGCs to integrate light over long periods of time. Chapter 3 of this dissertation describes experiments designed to determine the consequences that the persistently active state of melanopsin has for signal generation in ipRGCs.

IpRGCs Combine Intrinsic and Extrinsic Photosensitivity to Serve Many Functions

In addition to their melanopsin-driven intrinsic photosensitivity, ipRGCs receive rod- and cone-driven synaptic input. The roles of rod and cone signaling versus melanopsin-driven signaling have been intensively researched. The contribution of melanopsin to a number of visual physiological effects and behaviors has been studied by using melanopsin knockout mice, which only have rod- and cone-mediated

phototransduction intact (Hattar et al., 2003). In general, the behavioral light responses assayed in these mice do not reach the normal level of saturation and have attenuated responses to high intensity illumination (Hattar et al., 2003; Lucas et al., 2003; Mrosovsky and Hattar, 2003; Panda et al., 2002). Some behaviors, such as the pupillary light reflex and negative masking of locomotor activity, are also less sustained during ongoing illumination (Lucas et al., 2003; Mrosovsky and Hattar, 2003). These studies demonstrate a role for melanopsin in these behaviors, but there is also evidence for the involvement of rods and cones, as no visual effect was completely eliminated by the melanopsin knockout.

IpRGCs appear to be necessary for relaying rod and cone signals to brain areas that regulate several non-image-forming functions. This was demonstrated by selective lesion of ipRGCs with diphtheria toxin or saporin toxin expressed in or targeted to melanopsin-expressing cells (Goz et al., 2008; Güler et al., 2008; Hatori et al., 2008). Partial lesions produced highly attenuated light-induced circadian phase shifts and pupil constriction (Goz et al., 2008; Güler et al., 2008) and complete lesion completely abolished both of these behaviors (Hatori et al., 2008). These mice have intact rods, cones, and conventional RGCs as well as normal visual acuity (Goz et al., 2008; Güler et al., 2008; Hatori et al., 2008). Therefore, conventional RGCs are not sufficient for these behaviors and the rod and cone input relies on the presence of ipRGCs.

The relative role of each pigment in behavioral light responses has been further studied using spectral measurements. However, the spectral sensitivity of the opsin expressed in the medium-wavelength sensing cone is quite similar to melanopsin, so results of spectral measurements could only be adequately interpreted with genetic modifications of the medium-wavelength cone opsin. This has been done by using mice in which the medium-wavelength cone opsin is not expressed (Dkhissi-Benyahya et al., 2007), as well as by replacing it with the human long-wavelength cone opsin (Smallwood et al., 2003). These manipulations demonstrate roles for the medium-wavelength cone in circadian photoentrainment to short pulses of light, but it appears to have a much weaker influence on the clock than rhodopsin and melanopsin (Dkhissi-Benyahya et al., 2007; Lall et al., 2010). At high intensities, melanopsin appears to be the sole regulator of the clock and other visual functions (Lall et al.,

2010; McDougal and Gamlin, 2010). Much of the focus of this thesis is on the melanopsin-driven intrinsic response to light in ipRGCs.

Diversity of IpRGCs

While ipRGCs can be defined by the expression of a single gene, they do not make up a homogeneous population. There are at least five morphologically-defined ipRGC subtypes in the mouse, currently designated M1-M5 (Figure 1.1), and at least some of these subtypes are conserved in primates (Baver et al., 2008; Berson et al., 2010; Dacey et al., 2005; Ecker et al., 2010; Liao et al., 2016; Schmidt et al., 2014; Schmidt and Kofuji, 2009, 2011; Tu et al., 2005). M1 ipRGCs place their dendrites in a specific section of the plexiform layer between RGCs and bipolar cells, called the OFF sublamina of the inner plexiform layer (IPL; Figure 1.1). M1 ipRGCs have the highest and densest melanopsin expression among melanopsin subtypes and are understood to be distinguishable, as a population, from other subtypes by their physiological properties, such as large light responses, high membrane resistance, and low firing frequency (Baver et al., 2008; Berson et al., 2010; Ecker et al., 2010; Schmidt and Kofuji, 2009; Tu et al., 2005; Zhao et al., 2014). M2 ipRGCs have dendrites that stratify in the ON sublamina of the IPL (Figure 1.1), have lower melanopsin expression levels, and have physiological properties that differ from M1 ipRGCs, such as small intrinsic light responses and the capability to fire at high frequencies (Berson et al., 2010; Schmidt and Kofuji, 2009; Zhao et al., 2014). M3 ipRGCs have dendrites that stratify both the ON and OFF sublaminae of the IPL (Figure 1.1) and have physiological properties that are similar to M2 ipRGCs (Berson et al., 2010; Schmidt and Kofuji, 2011).

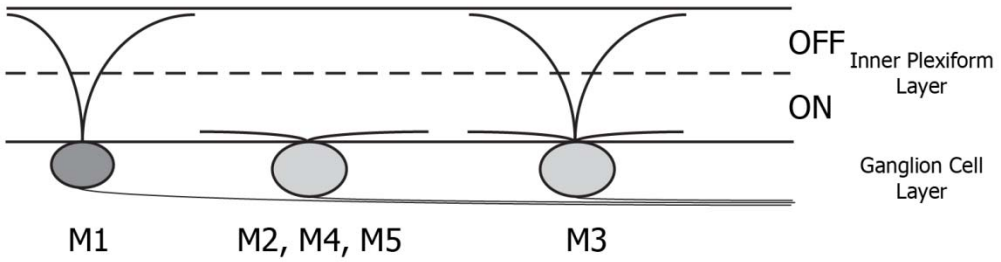

Figure 1.1. Dendritic Stratification of IpRGC Subtypes.

Schematic illustrating dendrite stratification of the inner plexiform layer of five known ipRGC subtypes. The dendrites of M1 ipRGCs stratify the OFF sublamina of the inner plexiform layer, those of M2, M4, and M5 ipRGCs stratify the ON sublamina of the inner plexiform layer, and the M3 ipRGCs stratify both layers. M1 ipRGCs express more melanopsin and have smaller somas than non-M1 ipRGCs, which is indicated by the shading and size of the cell bodies, respectively.

IpRGC subtypes designated M4 and above have such low levels of melanopsin that the sensitivity of conventional immunohistochemistry is not sufficient for their identification. Instead, they can be labeled with tyramide-amplified immunohistochemistry or in a Cre-reporter mouse in which Cre recombinase is expressed in the melanopsin gene locus and expression of a fluorescent reporter protein is driven in a Cre-dependent manner (Ecker et al., 2010). It has recently been determined that M4 ipRGCs convey information to the visual thalamus and play a role in contrast vision (Ecker et al., 2010; Estevez et al., 2012; Schmidt et al., 2014). M5 ipRGCs have been described anatomically and physiologically, but the functions they regulate are thus far unknown (Ecker et al., 2010; Zhao et al., 2014).

The synaptic inputs onto ipRGCs also differ between subtypes. Due to technical reasons, it is difficult to assess the rod input to ipRGCs. IpRGCs are sparse, so they generally require a fluorescent label for their identification for targeted patch-clamp recording, the ideal technique for measuring synaptic inputs. The imaging light used to identify the cells completely bleaches rod phototransduction, and the rods in the *in vitro* mouse retina do not recover. Currently, the best evidence for rod-driven responses in mouse ipRGCs comes from recordings performed with a multielectrode array, which does not require any fluorescence identification of ipRGCs (Weng et al., 2013), and evaluation of the pupillary light reflex and photoentrainment of the circadian clock (Altimus et al., 2010; Lall et al., 2010), which are wholly dependent on ipRGCs (Goz et al., 2008; Güler et al., 2008; Hatori et al., 2008). Whole-cell recordings from ipRGCs identified with two-photon microscopy, which bleaches rods to a lesser extent, also provide evidence that the threshold for ipRGC activation with synaptic transmission intact is within the scotopic range, and the intensity at which a rod-driven response is detected is similar across ipRGC subtypes (Zhao et al., 2014). In all, these studies suggest that ipRGCs receive input from the most sensitive rod pathway.

The cone input to ipRGCs is less susceptible to the technical limitations because cones can adapt and continue to signal in very bright light and recover their chromophore within the isolated retina (Wang and Kefalov, 2011). Therefore, the cone input can be assessed even when ipRGCs are identified with fluorescence. Despite different dendritic stratification patterns of the IPL, which typically allow one to

predict the polarity of the synaptic input at the ganglion cells, all ipRGCs receive ON input (i.e., depolarization in response to an increment in light intensity; Dumitrescu et al., 2009; Estevez et al., 2012; Hoshi et al., 2009; Schmidt and Kofuji, 2010; Schmidt et al., 2008). M1 ipRGCs generally have weaker cone-driven synaptic input than M2 or M3 ipRGCs, as revealed by pharmacology as well as by recordings performed in mice lacking melanopsin (Schmidt and Kofuji, 2010, 2011). M4 ipRGCs also have strong, cone-driven synaptic input (Estevez et al., 2012). In these cells, the spectral sensitivity of the synaptic inputs was measured and it reflects the gradient in short-wavelength and medium-wavelength cones observed in the mouse retina (Estevez et al., 2012). In macaque retina, ipRGCs receive a rare combination of cone inputs. Short-wavelength cones drive an OFF response in some cells, while medium- and long-wavelength cones drive an ON response (Dacey et al., 2005). Macaque ipRGCs were able to signal at scotopic light intensities, suggesting that they are also driven by rods (Dacey et al., 2005). Although multiple morphological subtypes have been described in human and macaque retina (Liao et al., 2016), it is not yet known whether there is a corresponding diversity in rod- and cone-driven inputs to different subtypes.

As a population, ipRGCs innervate many different brain areas to regulate various functions. The projection patterns of ipRGCs in rodents have been studied with a number of approaches. The presence of RGC projections to regions now known to be targeted by ipRGCs had been demonstrated well before the discovery of melanopsin (Hendrickson et al., 1972; Moore and Lenn, 1972). Multiple groups have used retrograde-labeling techniques to identify RGCs that project to these regions, such as the SCN and olivary pretectal nucleus (OPN), and found that proportions of the retrograde-labeled RGCs expressed melanopsin (Berson et al., 2002; Gooley et al., 2001; Gooley et al., 2003; Morin et al., 2003). Furthermore, expression of pituitary-adenylate-cyclase activating polypeptide (PACAP) was found in a subset of ganglion cells that all co-express melanopsin. Thus, the projections of rat ipRGCs were identified by co-staining brains for retinal projections and for PACAP (Hannibal and Fahrenkrug, 2004).

With the genetic control of the melanopsin locus, the projections of these cells could be examined with even higher precision. The creation of a transgenic mouse in which the tau-LacZ gene replaced a copy of melanopsin in its locus (Hattar et al., 2002) allowed examination of ipRGC projections

to the brain based on the expression and enzymatic activity of β galactosidase, the enzyme encoded by the LacZ gene. The densest label was seen in the SCN, OPN, and intergeniculate leaflet (IGL; Hattar et al., 2002), but these neurons send axons to approximately a dozen additional regions (Hattar et al., 2006). These projections likely arise from the M1 subtype because the expression level of tau-LacZ is too low in other subtypes to drive detectable expression of β galactosidase (Ecker et al., 2010; Hattar et al., 2006).

The use of the more sensitive Cre line allowed identification of targets of non-M1 ipRGCs (Ecker et al., 2010). In addition to the M1 targets, this mouse shows denser ipRGC projections to the dorsal lateral geniculate nucleus (dLGN), the core region of the OPN, the superior colliculus, ventral LGN, and posterior pretectal nucleus (Ecker et al., 2010). The widespread projection patterns of ipRGCs suggest that they influence many functions (Ecker et al., 2010; Morin and Studholme, 2014). Some of these functions and the projections that regulate them are well-established, such as the photic entrainment of the circadian clock and the pupillary light reflex, which are mediated by projections to the SCN and OPN, respectively. Others are not as well-delineated, such as the role of ipRGCs in light-induced pain (Matynia et al., 2012), modulation of sleep (Lupi et al., 2008), and modulation of locomotor activity (Mrosovsky and Hattar, 2003). While a role for melanopsin phototransduction and ipRGCs has been demonstrated for these functions, the specific responsible brain projection has not been definitively identified. There are also regions that receive ipRGC projections, such as the lateral hypothalamus, that do not have well-defined visual functions.

There is evidence that individual ipRGCs have bifurcated axons that project to multiple brain regions (Gooley et al., 2003; Morin et al., 2003). This observation suggests that similar information would be available to different brain regions. Some proportion of rat ipRGCs innervate both the SCN and OPN (Gooley et al., 2003), even though the visual functions controlled by these regions use light in very different manners. The circadian clock (SCN) integrates light over time (Nelson and Takahashi, 1991), while the pupil (OPN) responds to light transiently. In mice, the lineage expression of a transcription factor, Brn3b, largely separates a population of ipRGCs that project to the OPN and control the pupil from ipRGCs that project to the SCN and are sufficient for controlling the clock (Chen et al., 2011). Given these

different views, the extent to which the population of ipRGCs that project to the SCN and are responsible for controlling the clock is separable from the population of ipRGCs that project to the OPN and control the pupil is currently unclear.

Regardless, the physiological properties of ipRGCs that project to each area have not been examined, and it has not yet been determined whether the signals generated within ipRGCs are tailored to the functions that they regulate. In addition, we do not yet have a full understanding of the diversity within and between morphological subtypes. Chapter 4 of this dissertation addresses these issues by systematically examining signal generation in ipRGCs and comparing ipRGC signaling in cells that regulate hypothalamic-driven functions to that in cells that regulate pretectal-driven functions. The results of these experiments demonstrate that there is a remarkable degree of physiological diversity within and between morphologically-defined melanopsin subtypes and that the functions driven by these brain areas are regulated by ipRGCs with highly overlapping physiological properties.

References

Altimus, C.M., Guler, A.D., Alam, N.M., Arman, A.C., Prusky, G.T., Sampath, A.P., and Hattar, S. (2010). Rod photoreceptors drive circadian photoentrainment across a wide range of light intensities. Nat. Neuro. 13, 1107-1112.

Baden, T., Berens, P., Franke, K., Roman Roson, M., Bethge, M., and Euler, T. (2016). The functional diversity of retinal ganglion cells in the mouse. Nature 529, 345-350.

Bailes, H.J., and Lucas, R.J. (2013). Human melanopsin forms a pigment maximally sensitive to blue light (λmax ≈ 479 nm) supporting activation of G(q/11) and G(i/o) signalling cascades. Proc. Biol. Sci. 280, 20122987.

Baver, S.B., Pickard, G.E., and Sollars, P.J. (2008). Two types of melanopsin retinal ganglion cell differentially innervate the hypothalamic suprachiasmatic nucleus and the olivary pretectal nucleus. Eur. J. Neurosci. 27, 1763-1770.

Bernard, G.D. (1983). Bleaching of rhabdoms in eyes of intact butterflies. Science 219, 69-71.

Berson, D.M., Castrucci, A.M., and Provencio, I. (2010). Morphology and mosaics of melanopsin-expressing retinal ganglion cell types in mice. J. Comp. Neurol. 518, 2405-2422.

Berson, D.M., Dunn, F.A., and Takao, M. (2002). Phototransduction by retinal ganglion cells that set the circadian clock. Science 295, 1070-1073.

Chen, C.K., Burns, M.E., Spencer, M., Niemi, G.A., Chen, J., Hurley, J.B., Baylor, D.A., and Simon, M.I. (1999). Abnormal photoresponses and light-induced apoptosis in rods lacking rhodopsin kinase. Proc. Natl. Acad. Sci. USA 96, 3718-3722.

Chen, S.K., Badea, T.C., and Hattar, S. (2011). Photoentrainment and pupillary light reflex are mediated by distinct populations of ipRGCs. Nature 476, 92-95.

Chew, K.S., Schmidt, T.M., Rupp, A.C., Kofuji, P., and Trimarchi, J.M. (2014). Loss of *Gq/11* genes does not abolish melanopsin phototransduction. PloS ONE 9, e98356.

Dacey, D.M., Liao, H.W., Peterson, B.B., Robinson, F.R., Smith, V.C., Pokorny, J., Yau, K.-W., and Gamlin, P.D. (2005). Melanopsin-expressing ganglion cells in primate retina signal colour and irradiance and project to the LGN. Nature 433, 749-754.

Dkhissi-Benyahya, O., Gronfier, C., De Vanssay, W., Flamant, F., and Cooper, H.M. (2007). Modeling the role of mid-wavelength cones in circadian responses to light. Neuron 53, 677-687.

Do, M.T.H., and Yau, K.-W. (2013). Adaptation to steady light by intrinsically photosensitive retinal ganglion cells. Proc. Natl. Acad. Sci. USA 110, 7470-7475.

Do, M.T.H., Kang, S.H., Xue, T., Zhong, H., Liao, H.W., Bergles, D.E., and Yau, K.-W. (2009). Photon capture and signalling by melanopsin retinal ganglion cells. Nature 457, 281-287.

Dumitrescu, O.N., Pucci, F.G., Wong, K.Y., and Berson, D.M. (2009). Ectopic retinal ON bipolar cell synapses in the OFF inner plexiform layer: contacts with dopaminergic amacrine cells and melanopsin ganglion cells. J. Comp. Neurol. 517, 226-244.

Ecker, J.L., Dumitrescu, O.N., Wong, K.Y., Alam, N.M., Chen, S.K., LeGates, T., Renna, J.M., Prusky, G.T., Berson, D.M., and Hattar, S. (2010). Melanopsin-expressing retinal ganglion-cell photoreceptors: cellular diversity and role in pattern vision. Neuron 67, 49-60.

Emanuel, A.J., and Do, M.T.H. (2015). Melanopsin tristability for sustained and broadband phototransduction. Neuron 85, 1043-1055.

Estevez, M.E., Fogerson, P.M., Ilardi, M.C., Borghuis, B.G., Chan, E., Weng, S., Auferkorte, O.N., Demb, J.B., and Berson, D.M. (2012). Form and function of the M4 cell, an intrinsically photosensitive retinal ganglion cell type contributing to geniculocortical vision. J. Neurosci. 32, 13608-13620.

Freedman, M.S., Lucas, R.J., Soni, B., von Schantz, M., Munoz, M., David-Gray, Z., and Foster, R. (1999). Regulation of mammalian circadian behavior by non-rod, non-cone, ocular photoreceptors. Science 284, 502-504.

Fu, Y., Zhong, H., Wang, M.H., Luo D.G., Liao, H.W., Maeda, H., Hattar, S., Frishman, L.J., Yau, K.-W. (2005). Intrinsically photosensitive retinal ganglion cells detect light with a vitamin A-based photopigment. Proc. Natl. Acad. Sci. USA 15, 415-422.

Gooley, J.J., Lu, J., Chou, T.C., Scammell, T.E., and Saper, C.B. (2001). Melanopsin in cells of origin of the retinohypothalamic tract. Nat. Neurosci. 4, 1165.

Gooley, J.J., Lu, J., Fischer, D., and Saper, C.B. (2003). A broad role for melanopsin in nonvisual photoreception. J. Neurosci. 23, 7093-7106.

Goz, D., Studholme, K., Lappi, D.A., Rollag, M.D., Provencio, I., and Morin, L.P. (2008). Targeted destruction of photosensitive retinal ganglion cells with a saporin conjugate alters the effects of light on mouse circadian rhythms. PloS ONE 3, e3153.

Graham, D.M., Wong, K.Y., Shapiro, P., Frederick, C., Pattabiraman, K., and Berson, D.M. (2008). Melanopsin ganglion cells use a membrane-associated rhabdomeric phototransduction cascade. J. Neurophysiol. 99, 2522-2532.

Güler, A.D., Ecker, J.L., Lall, G.S., Haq, S., Altimus, C.M., Liao, H.W., Barnard, A.R., Cahill, H., Badea, T.C., Zhao, H.*, et al.* (2008). Melanopsin cells are the principal conduits for rod-cone input to non-image-forming vision. Nature 453, 102-105.

Hannibal, J., and Fahrenkrug, J. (2004). Target areas innervated by PACAP-immunoreactive retinal ganglion cells. Cell Tissue Res. 316, 99-113.

Hannibal, J., Hindersson, P., Knudsen, S.M., Georg, B., and Fahrenkrug, J. (2002). The photopigment melanopsin is exclusively present in pituitary adenylate cyclase-activating polypeptide-containing retinal ganglion cells of the retinohypothalamic tract. J. Neurosci. 22, RC191.

Hatori, M., Le, H., Vollmers, C., Keding, S.R., Tanaka, N., Buch, T., Waisman, A., Schmedt, C., Jegla, T., and Panda, S. (2008). Inducible ablation of melanopsin-expressing retinal ganglion cells reveals their central role in non-image forming visual responses. PloS ONE 3, e2451.

Hattar, S., Kumar, M., Park, A., Tong, P., Tung, J., Yau, K.-W., and Berson, D.M. (2006). Central projections of melanopsin-expressing retinal ganglion cells in the mouse. J. Comp. Neurol. 497, 326-349.

Hattar, S., Liao, H.W., Takao, M., Berson, D.M., and Yau, K.-W. (2002). Melanopsin-containing retinal ganglion cells: architecture, projections, and intrinsic photosensitivity. Science 295, 1065-1070.

Hattar, S., Lucas, R.J., Mrosovsky, N., Thompson, S., Douglas, R.H., Hankins, M.W., Lem, J., Biel, M., Hofmann, F., Foster, R.G., and Yau, K.-W. (2003). Melanopsin and rod-cone photoreceptive systems account for all major accessory visual functions in mice. Nature 424, 76-81.

Helmstaedter, M., Briggman, K.L., Turaga, S.C., Jain, V., Seung, H.S., and Denk, W. (2013). Connectomic reconstruction of the inner plexiform layer in the mouse retina. Nature 500, 168-174.

Hendrickson A.E., Wagoner N., and Cowan, W.M. (1972). An autoradiographic and electron microscopic study of retino-hypothalamic connections. Z. Zellforsch. Mikrosk. Anat. 135, 1-26

Hillman, P., Hochstein, S., and Minke, B. (1983). Transduction in invertebrate photoreceptors: role of pigment bistability. Physiol. Rev. 63, 668-772.

Hoshi, H., Liu, W.L., Massey, S.C., and Mills, S.L. (2009). ON inputs to the OFF layer: bipolar cells that break the stratification rules of the retina. J. Neurosci. 29, 8875-8883.

Lall, G.S., Revell, V.L., Momiji, H., Al Enezi, J., Altimus, C.M., Guler, A.D., Aguilar, C., Cameron, M.A., Allender, S., Hankins, M.W., and Lucas, R.J. (2010). Distinct contributions of rod, cone, and melanopsin photoreceptors to encoding irradiance. Neuron 66, 417-428.

Liao, H.W., Ren, X., Peterson, B.B., Marshak, D.W., Yau, K.-W., Gamlin, P.D., and Dacey, D.M. (2016). Melanopsin-expressing ganglion cells in macaque and human retinas form two morphologically distinct populations. J. Comp. Neurol. Accepted Article. Doi: 10.1002/cne.23995.

Lucas, R.J., Hattar, S., Takao, M., Berson, D.M., Foster, R.G., and Yau, K.-W. (2003). Diminished pupillary light reflex at high irradiances in melanopsin-knockout mice. Science 299, 245-247.

Luo, D.-G., Kefalov, V., and Yau, K.-W. (2008). Phototransduction in retinal rods and cones. In The Senses: A Comprehensive Reference, A.I. Basbaum, ed. (Elsevier/Academic Press).

Lupi, D., Oster, H., Thompson, S., and Foster, R.G. (2008). The acute light-induction of sleep is mediated by OPN4-based photoreception. Nat. Neurosci. 11, 1068-1073.

Masland, R.H. (2012). The neuronal organization of the retina. Neuron 76, 266-280.

Matsuyama, T., Yamashita, T., Imamoto, Y., and Shichida, Y. (2012). Photochemical properties of mammalian melanopsin. Biochemistry 51, 5454-5462.

Matynia, A., Parikh, S., Chen, B., Kim, P., McNeill, D.S., Nusinowitz, S., Evans, C., and Gorin, M.B. (2012). Intrinsically photosensitive retinal ganglion cells are the primary but not exclusive circuit for light aversion. Exp. Eye Res. 105, 60-69.

Mawad, K., and Van Gelder, R.N. (2008). Absence of long-wavelength photic potentiation of murine intrinsically photosensitive retinal ganglion cell firing *in vitro*. J. Biol. Rhythms 23, 387-391.

McDougal, D.H., and Gamlin, P.D. (2010). The influence of intrinsically-photosensitive retinal ganglion cells on the spectral sensitivity and response dynamics of the human pupillary light reflex. Vision Res. 50, 72-87.

Melyan, Z., Tarttelin, E.E., Bellingham, J., Lucas, R.J., and Hankins, M.W. (2005). Addition of human melanopsin renders mammalian cells photoresponsive. Nature 433, 741-745.

Moore, R.Y., and Lenn, N.J. (1972). A retinohypothalamic projection in the rat. J. Comp. Neurol. 146, 1-14.

Morin, L.P., Blanchard, J.H., and Provencio, I. (2003). Retinal ganglion cell projections to the hamster suprachiasmatic nucleus, intergeniculate leaflet, and visual midbrain: bifurcation and melanopsin immunoreactivity. J. Comp. Neurol. 465, 401-416.

Morin, L.P., and Studholme, K.M. (2014). Retinofugal projections in the mouse. J. Comp. Neurol. 522, 3733-3753.

Mrosovsky, N., and Hattar, S. (2003). Impaired masking responses to light in melanopsin-knockout mice. Chronobiol. Int. 20, 989-999.

Mure, L.S., Cornut, P.L., Rieux, C., Drouyer, E., Denis, P., Gronfier, C., and Cooper, H.M. (2009). Melanopsin bistability: a fly's eye technology in the human retina. PloS ONE 4, e5991.

Mure, L.S., Rieux, C., Hattar, S., and Cooper, H.M. (2007). Melanopsin-dependent nonvisual responses: evidence for photopigment bistability *in vivo*. J. Biol. Rhythms 22, 411-424.

Nathans, J., Thomas, D., and Hogness, D.S. (1986). Molecular genetics of human color vision: the genes encoding blue, green, and red pigments. Science 232, 193-202.

Nelson, D.E., and Takahashi, J.S. (1991). Sensitivity and integration in a visual pathway for circadian entrainment in the hamster (*Mesocricetus auratus*). J. Physiol. 439, 115-145.

Palczewski, K. (2006). G protein-coupled receptor rhodopsin. Annu. Rev. Biochem. 75, 743-767.

Palczewski, K., Kumasaka, T., Hori, T., Behnke, C.A., Motoshima, H., Fox, B.A., Le Trong, I., Teller, D.C., Okada, T., Stenkamp, R.E.*, et al.* (2000). Crystal structure of rhodopsin: A G protein-coupled receptor. Science 289, 739-745.

Panda, S., Nayak, S.K., Campo, B., Walker, J.R., Hogenesch, J.B., and Jegla, T. (2005). Illumination of the melanopsin signaling pathway. Science 307, 600-604.

Panda, S., Sato, T.K., Castrucci, A.M., Rollag, M.D., DeGrip, W.J., Hogenesch, J.B., Provencio, I., and Kay, S.A. (2002). Melanopsin (Opn4) requirement for normal light-induced circadian phase shifting. Science 298, 2213-2216.

Perez-Leighton, C.E., Schmidt, T.M., Abramowitz, J., Birnbaumer, L., and Kofuji, P. (2011). Intrinsic phototransduction persists in melanopsin-expressing ganglion cells lacking diacylglycerol-sensitive TRPC subunits. Eur. J. Neurosci. 33, 856-867.

Provencio, I., Jiang, G., De Grip, W.J., Hayes, W.P., and Rollag, M.D. (1998). Melanopsin: An opsin in melanophores, brain, and eye. Proc. Natl. Acad. Sci. USA 95, 340-345.

Provencio, I., Rodriguez, I.R., Jiang, G., Hayes, W.P., Moreira, E.F., and Rollag, M.D. (2000). A novel human opsin in the inner retina. J. Neurosci. 20, 600-605.

Qiu, X., Kumbalasiri, T., Carlson, S.M., Wong, K.Y., Krishna, V., Provencio, I., and Berson, D.M. (2005). Induction of photosensitivity by heterologous expression of melanopsin. Nature 433, 745-749.

Saari, J.C. (2000). Biochemistry of visual pigment regeneration: the Friedenwald lecture. Invest. Ophthalmol. Vis. Sci. 41, 337-348.

Sanes, J.R., and Masland, R.H. (2015). The types of retinal ganglion cells: current status and implications for neuronal classification. Annu. Rev. Neurosci. 38, 221-246.

Schmidt, T.M., Alam, N.M., Chen, S., Kofuji, P., Li, W., Prusky, G.T., and Hattar, S. (2014). A role for melanopsin in alpha retinal ganglion cells and contrast detection. Neuron 82, 781-788.

Schmidt, T.M., and Kofuji, P. (2009). Functional and morphological differences among intrinsically photosensitive retinal ganglion cells. J. Neurosci. 29, 476-482.

Schmidt, T.M., and Kofuji, P. (2010). Differential cone pathway influence on intrinsically photosensitive retinal ganglion cell subtypes. J. Neurosci. 30, 16262-16271.

Schmidt, T.M., and Kofuji, P. (2011). Structure and function of bistratified intrinsically photosensitive retinal ganglion cells in the mouse. J. Comp. Neurol. 519, 1492-1504.

Schmidt, T.M., Taniguchi, K., and Kofuji, P. (2008). Intrinsic and extrinsic light responses in melanopsin-expressing ganglion cells during mouse development. J. Neurophysiol. 100, 371-384.

Sekaran, S., Foster, R.G., Lucas, R.J., and Hankins, M.W. (2003). Calcium imaging reveals a network of intrinsically light-sensitive inner-retinal neurons. Curr. Biol. 13, 1290-1298.

Sekaran, S., Lall, G.S., Ralphs, K.L., Wolstenholme, A.J., Lucas, R.J., Foster, R.G., and Hankins, M.W. (2007). 2-Aminoethoxydiphenylborane is an acute inhibitor of directly photosensitive retinal ganglion cell activity *in vitro* and *in vivo*. J. Neurosci. 27, 3981-3986.

Sexton, T.J., Golczak, M., Palczewski, K., and Van Gelder, R.N. (2012). Melanopsin is highly resistant to light and chemical bleaching *in vivo*. J. Biol. Chem. 287, 20888-20897.

Shapley, R., and Enroth-Cugell, C. (1984). Visual adaptation and retinal gain controls. Prog. Retin. Eye Res. 3, 263-346.

Smallwood, P.M., Olveczky, B.P., Williams, G.L., Jacobs, G.H., Reese, B.E., Meister, M., and Nathans, J. (2003). Genetically engineered mice with an additional class of cone photoreceptors: implications for the evolution of color vision. Proc. Natl. Acad. Sci. USA 100, 11706-11711.

Takahashi, J.S., Hong, H.K., Ko, C.H., and McDearmon, E.L. (2008). The genetics of mammalian circadian order and disorder: implications for physiology and disease. Nat. Rev. Genet. 9, 764-775.

Tsukamoto, H., Kubo, Y., Farrens, D.L., Koyanagi, M., Terakita, A., and Furutani, Y. (2015). Retinal attachment instability is diversified among mammalian melanopsins. J. Biol. Chem. 290, 27176-27187.

Tsunematsu, T., Tanaka, K.F., Yamanaka, A., and Koizumi, A. (2013). Ectopic expression of melanopsin in orexin/hypocretin neurons enables control of wakefulness of mice *in vivo* by blue light. Neurosci. Res. 75, 23-28.

Tu, D.C., Zhang, D., Demas, J., Slutsky, E.B., Provencio, I., Holy, T.E., and Van Gelder, R.N. (2005). Physiologic diversity and development of intrinsically photosensitive retinal ganglion cells. Neuron 48, 987-999.

Walker, M.T., Brown, R.L., Cronin, T.W., and Robinson, P.R. (2008). Photochemistry of retinal chromophore in mouse melanopsin. Proc. Natl. Acad. Sci. USA 105, 8861-8865.

Wang, J.S., and Kefalov, V.J. (2011). The cone-specific visual cycle. Prog. Retin. Eye Res. 30, 115-128.

Weng, S., Estevez, M.E., and Berson, D.M. (2013). Mouse ganglion-cell photoreceptors are driven by the most sensitive rod pathway and by both types of cones. PloS ONE 8, e66480.

Wong, K.Y., Dunn, F.A., and Berson, D.M. (2005). Photoreceptor adaptation in intrinsically photosensitive retinal ganglion cells. Neuron 48, 1001-1010.

Xue, T., Do, M.T.H., Riccio, A., Jiang, Z., Hsieh, J., Wang, H.C., Merbs, S.L., Welsbie, D.S., Yoshioka, T., Weissgerber, P.*, et al.* (2011). Melanopsin signaling in mammalian iris and retina. Nature 479, 67-73.

Yau, K.-W., and Hardie, R.C. (2009). Phototransduction motifs and variations. Cell 139, 246-264.

Ye, H., Daoud-El Baba, M., Peng, R.W., and Fussenegger, M. (2011). A synthetic optogenetic transcription device enhances blood-glucose homeostasis in mice. Science 332, 1565-1568.

Zhao, X., Stafford, B.K., Godin, A.L., King, W.M., and Wong, K.Y. (2014). Photoresponse diversity among the five types of intrinsically photosensitive retinal ganglion cells. J. Physiol. 592, 1619-1636.

Chapter 2: Melanopsin Tristability for Sustained and Broadband Phototransduction

Alan Joseph Emanuel and Michael Tri Hoang Do

This chapter of this dissertation is reprinted from Neuron, 85, Emanuel, A.J. and Do, M.T.H., Melanopsin Tristability for Sustained and Broadband Phototransduction, 1043-1055, 2015, with permission from Elsevier. It has been formatted here to match the style of the dissertation. Link to formal publication by DOI: http://dx.doi.org/10.1016/j.neuron.2015.02.011.

Summary

Mammals rely upon three ocular photoreceptors to sense light: rods, cones, and intrinsically photosensitive retinal ganglion cells (ipRGCs). Rods and cones resolve details in the visual scene. Conversely, ipRGCs integrate over time and space, primarily to support "non-image" vision. The integrative mechanisms of ipRGCs are enigmatic, particularly since these cells use a phototransduction motif that allows invertebrates like Drosophila to parse light with exceptional temporal resolution. Here, we provide evidence for a single mechanism that allows ipRGCs to integrate over both time and wavelength. Light distributes the visual pigment, melanopsin, across three states, two silent and one signaling. Photoequilibration among states maintains pigment availability for sustained signaling, stability of the signaling state permits minutes-long temporal summation, and modest spectral separation of the silent states promotes uniform activation across wavelengths. By broadening the tuning of ipRGCs in both temporal and chromatic domains, melanopsin tristability produces signal integration for physiology and behavior.

Introduction

The visual system resolves detail to support familiar tasks like recognizing objects and guiding action, but many processes have quite different requirements for sensing light. These "non-image" visual functions include the regulation of sleep, hormone levels, pupil contraction, and the circadian clock (reviewed by Do and Yau, 2010; Lucas et al., 2014). They tend to integrate rather than resolve, thereby smoothing fluctuations in light level across space and time to produce accurate representations of overall irradiance. The degree of integration can be remarkable. For instance, the circadian clock responds similarly to a given number of photons whether that number is delivered over milliseconds or minutes (Nelson and Takahashi, 1991). The clock uses irradiance to synchronize its endogenous rhythm with the solar day, thereby establishing normal patterns of gene expression in practically every tissue and allowing organisms to anticipate cycles of key parameters such as temperature and predator behaviors (Mohawk et al., 2012). Dysregulation of the clock is linked to psychiatric illness, cardiovascular disease, metabolic disorders, and cancer (Takahashi et al., 2008).

Mammalian non-image vision begins in the retina and is supported by intrinsically photosensitive retinal ganglion cells (ipRGCs; Berson et al., 2002). IpRGCs are like conventional retinal ganglion cells (RGCs) in that they convey visual information to the brain that originates from the rod and cone photoreceptors. IpRGCs also sense light directly through their own mechanism of phototransduction. Selective elimination of ipRGC phototransduction has broad effects on the organism. Some visual functions are unable to reach their natural maxima. For instance, pupil constriction and circadian phase-shifting cannot be driven to completion; instead, they saturate at abnormally low light intensities (Lucas et al., 2003; Panda et al., 2002). Furthermore, some functions are abnormally fleeting. For example, pupil constriction and the acute modulation of locomotor activity are not sustained during steady illumination (Mrosovsky and Hattar, 2003; Zhu et al., 2007). Thus, ipRGC phototransduction appears to be particularly important at high light intensities (i.e., room light and above) and over extended timescales (i.e., seconds to hours).

IpRGCs sense light using a visual pigment called melanopsin (Provencio et al., 1998, 2000). The wavelength sensitivity of melanopsin is precisely mirrored by that of ipRGCs, expression of melanopsin is required for all intrinsic light responses in ipRGCs and heterologous expression of melanopsin in other cell types renders them photosensitive with the known characteristics of melanopsin (Berson et al., 2002; Dacey et al., 2005; Hattar et al., 2003; Lucas et al., 2003; Melyan et al., 2005; Panda et al., 2005; Qiu et al., 2005). Melanopsin is unusual in that it is expressed in vertebrates but is most homologous to the rhabdomeric pigments that are typically found in invertebrates (Provencio et al., 1998, 2000; Shichida and Matsuyama, 2009). Within ipRGCs, melanopsin drives a transduction cascade that is distinguished by its prolonged time course. For example, the unitary (i.e., single-photon) response of ipRGC phototransduction has an integration time of 8 s, which is approximately 300-fold longer than that of *Drosophila* photoreceptors, 100-fold longer than that of mammalian cones, and 20-fold longer than that of mammalian rods (Do et al., 2009; Henderson et al., 2000). Thus, melanopsin function appears tailored to the integrative nature of non-image vision.

We have investigated signal integration by ipRGCs and obtained evidence that it is greater than previously appreciated. Not only does the intrinsic light response integrate over minutes of time, it also

integrates over wavelength. Furthermore, such integration appears to arise from molecular properties of melanopsin that have not been found in any other native visual pigment.

Results

IpRGCs Generate a Persistent Response that Produces Temporal Integration

Using established techniques, we identified ipRGCs within the in vitro mouse retina and monitored the output of individual neurons using the perforated-patch mode of electrophysiological recording, which preserves the melanopsin-driven light responses of these cells (Do et al., 2009; Do and Yau, 2013; Xue et al., 2011). Our principal focus was the M1 subtype of ipRGC, which is strictly required for photoregulation of the circadian clock and influences other non-image visual functions (Güler et al., 2008; Hatori et al., 2008). M1 ipRGCs are strongly driven by a melanopsin-mediated response that is 10-fold greater in sensitivity and saturated amplitude than that of other subtypes (Ecker et al., 2010; Schmidt and Kofuji, 2009, 2011). Such responses allow for precise, quantitative analysis. We recognized M1 ipRGCs by standard criteria (Experimental Procedures; Do et al., 2009; Do and Yau, 2013; Xue et al., 2011) and will refer to them simply as "ipRGCs" unless otherwise noted.

We recorded from single ipRGCs near body temperature (35 °C ± 1 °C) with synaptic transmission intact. We stimulated ipRGCs with xenon light, which has a spectrum that resembles sunlight, at intensities within the physiological range. During illumination, ipRGCs generated a response in which synaptic and intrinsic components were often discernable, as expected from prior studies (Perez-Leon et al., 2006; Schmidt and Kofuji, 2009; Wong et al., 2007). Upon cessation of illumination, we observed that the response could persist for many minutes in darkness.

Figure 2.1. Persistent Responses and Temporal Integration of IpRGCs

(A) Membrane voltage of an ipRGC in response to a series of 10-s pulses of white light (xenon at an intensity of 2.5×10^{-5} μW μm^{-2}, equivalent to 3.3×10^{4} lux). The corresponding spike rate is shown below in 10-s bins. Light monitor at bottom. Activation that continues beyond the period of illumination is referred to as the persistent response.

(B) Excerpts of the trace in (A) illustrating the response to the first and sixth light pulses. Dashed line represents the baseline (-60 mV).

(C) Subthreshold membrane voltages, averaged from 30-40 s after each light pulse, is displayed for individual cells (connected makers, n = 6 cells) and the population mean (bars) for this protocol. The difference from baseline, normalized to the maximum difference, is displayed for each cell. Closed markers represent the cell shown in (A).

(D) Subthreshold membrane voltage after the last pulse for the cell shown in (A) (in 5-s bins). Time point 0 corresponds to the end of illumination. Fit is a single exponential (τ = 107 s). All experiments were performed at 35 °C with synaptic transmission intact. See also Figure S1.

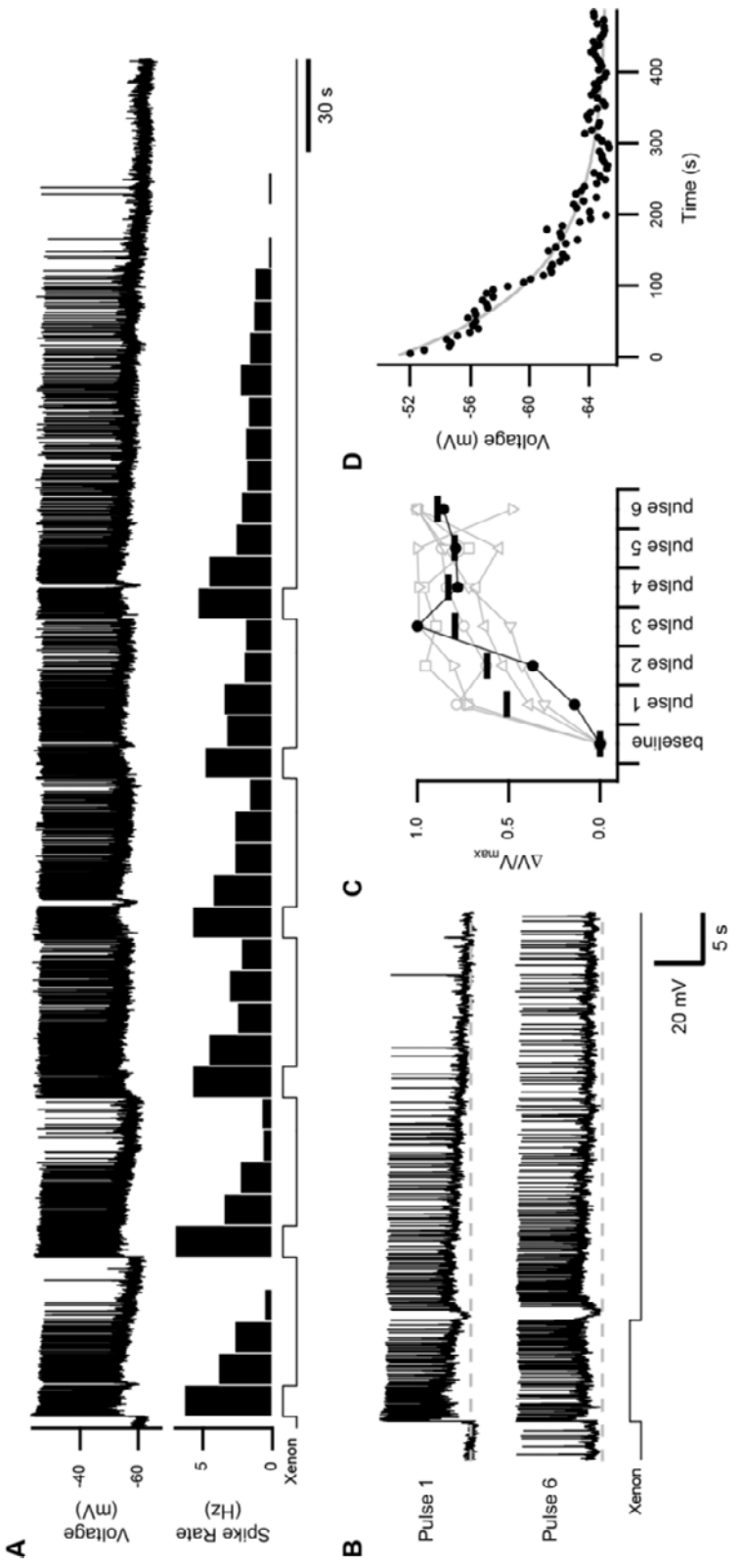

Figure 2.1 (Continued).

To evaluate the ability of these persistent responses to support temporal integration, we stimulated ipRGCs successively with pulses of light (10-s duration; intensity of 2.0×10^{-6} or 2.5×10^{-5} $\mu W\ \mu m^{-2}$, equivalent to 2.6×10^{3} or 3.3×10^{4} lux, respectively) that were separated by extended intervals of darkness (40 s). An example of temporal integration is illustrated in Figures 2.1A and 2.1B: the persistent response increases across stimuli until reaching saturation, both at the level of spiking and the subthreshold membrane voltage (observed in 6 cells; Figure 2.1C). Some ipRGCs did not display temporal integration because their persistent responses were small or were already saturated with the first stimulus (n = 9 cells). Such variation in photosensitivity is expected of ipRGCs, even within the M1 subtypes (Do et al., 2009; Do and Yau, 2013; Xue et al., 2011). Indeed, altering the light intensity to change the magnitude of the persistent response could unmask temporal integration in such cases (n = 2 of 2 cells tested; Figure S1).

We estimated the lifetime of the persistent response by monitoring the subthreshold membrane voltage following illumination. The decay was well described by a single exponential with a time constant of 122 ± 34 s (mean ± SEM, n = 10 cells with saturated persistent responses; example in Figure 2.1D). Thus, the persistent response is expected to promote temporal integration in a window of ~5 min, which is unexpectedly long because the unitary response of ipRGCs decays with a time constant of 8.3 ± 1.0 s (inferred from the dim-flash response of 18 cells measured in voltage clamp; Experimental Procedures).

The Persistent Response Arises from Melanopsin Phototransduction

To investigate the mechanism of the persistent response, we stimulated ipRGCs with monochromatic light (440-480 nm; Figure S2) near the peak wavelength sensitivity (λ_{max}) of melanopsin while isolating the intrinsic response by blocking synaptic transmission. A persistent response was produced in every case, indicating that it is inherent to ipRGCs (n = 85 cells). In current clamp, the persistent response was evident as a depolarization of the analog membrane voltage. With regard to spikes, this depolarization drove tonic firing in the largest fraction of ipRGCs, was too small to do so in others, and was so large in the remainder that spikes were attenuated (n = 18, 5, and 13 cells, respectively, probed with the same saturating pulse of short-wavelength light; Figure S2). When measured at room temperature, the persistent depolarization only decayed slightly in darkness

(observation period as long as 20 min; example in Figure 2.2A). Near body temperature, it lasted for minutes (n = 4 cells), as expected from experiments with synaptic transmission intact (Figure 2.1). Surprisingly, the persistent response was acutely decreased by light—provided that this light was of a longer wavelength than the preceding activating stimulus (Figures 2.2A-2.2D; n = 4 and 81 cells at 35 °C and 23 °C, respectively). Indeed, the persistent response was repeatedly increased and decreased in magnitude with successive pulses of light in a wavelength-dependent manner (Figures 2.2B-2.2D).

Figure 2.2. Persistent Responses Are Inherent to IpRGCs and Bi-Directionally Modulated by Light

(A) A persistent response evoked during pharmacological block of synaptic transmission. A flash of monochromatic, short-wavelength light was followed by darkness (~20 min) and then a pulse of long-wavelength light.

(B) An example of wavelength- and timing-dependent modulations of the persistent response in another ipRGC.

(C) Protocol for quantifying persistent responses in current clamp displayed with a representative recording. Periods of measurement are indicated by bars. Dashed lines indicate the average voltages measured following each stimulus (with lines extended for clarity). Persistent responses following short-wavelength stimuli are sufficiently large, in this cell, to cause depolarization block. Passive electrical properties were tested with hyperpolarizing current injections (5 pA, 1 s; bottom trace).

(D) Population data from the experiment illustrated in (C) with the difference in membrane voltage (from darkness) plotted for individual cells (connected markers). Groups marked with asterisks and daggers differ significantly from each other ($n = 8$ cells, $p < 0.001$). All experiments were performed at 23 °C with synaptic transmission blocked. Light stimuli were 50-ms flashes or 10-s pulses (monitors below traces). See Figure S2 for spectra and intensities of light.

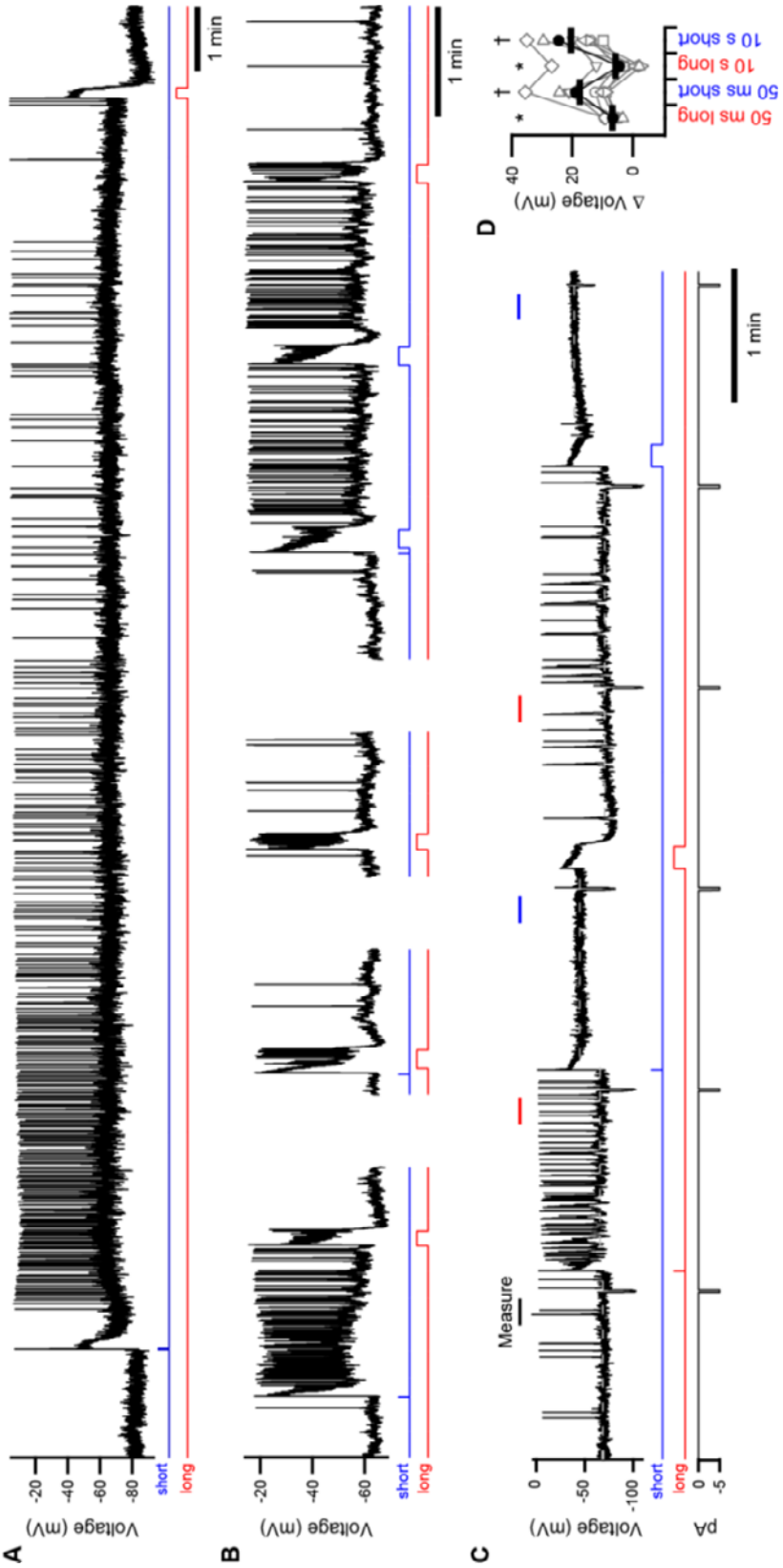

Figure 2.2 (Continued).

Together with melanopsin phototransduction, voltage-gated ion channels produce the intrinsic excitability of ipRGCs. The persistent response does not require these channels because it was neither increased nor decreased following pulses of depolarizing or hyperpolarizing current injection, respectively (all 36 cells tested). Furthermore, even when the membrane voltage was clamped, a robust persistent current was observed (n = 56 cells at -80 mV; example in Figure 2.3A). Comparison of persistent responses measured in current and voltage clamp (Figures 2.2B and 2.3A, respectively) indicates that phototransduction establishes a plateau of depolarization upon which voltage gated channels primarily serve to drive action potentials.

We used voltage-clamp recording to evaluate the dependence of the persistent response on wavelength (Figure 2.3B; Supplemental Experimental Procedures). While all tested wavelengths activated ipRGCs during the period of illumination itself, the persistent response was largest following the shortest wavelength and smaller following longer wavelengths (Figure 2.3C). The noise accompanying the persistent response, which resembles that generated by melanopsin phototransduction during illumination (Do and Yau, 2013), was similarly graded with wavelength (Figure 2.3C). Because light must act through melanopsin to influence ipRGCs (in the absence of synaptic transmission; Lucas et al., 2003), these data indicate that ongoing activity of melanopsin underlies the persistent response.

Melanopsin Activates from Two Silent States in IpRGCs

While the persistent response has no homolog in vertebrate rods and cones, it does resemble a feature displayed by many invertebrate photoreceptors, the "prolonged depolarizing afterpotential" (PDA; Hillman et al., 1983). The PDA is prolonged because the rhabdomeric type of visual pigment used by such photoreceptors has a stable signaling state. The pigment can be repeatedly switched between its signaling state and silent state by light, thereby activating and deactivating the PDA (Hillman et al., 1983). Such bistability has long been speculated to be a property of mammalian melanopsin (Melyan et al., 2005; Mure et al., 2007, 2009; Panda et al., 2005), though the topic is controversial (reviewed by Schmidt et al., 2011).

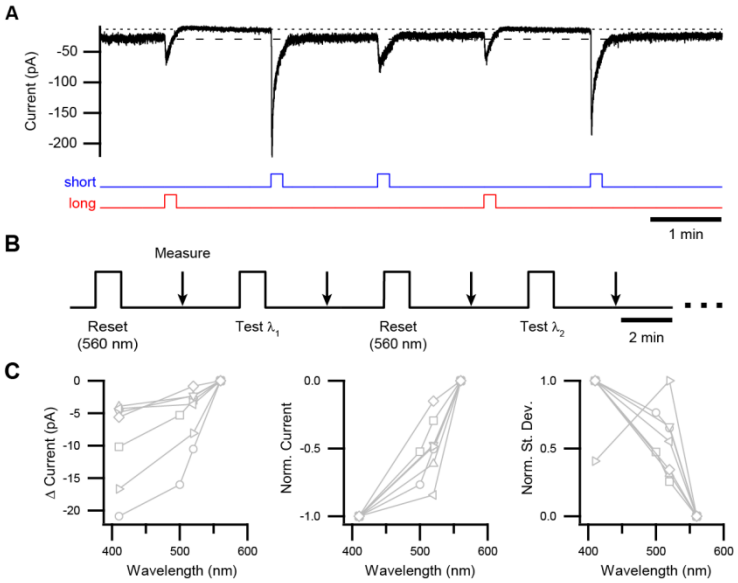

Figure 2.3. Wavelength Dependence of Persistent Responses Measured in Voltage Clamp

(A) Example of a persistent response (i.e., the light-evoked current that continues to flow beyond the period of illumination) modulated by successive pulses of short- and long-wavelength light. This response does not show temporal integration because it is saturated with each short-wavelength pulse at the intensity used here, and there is negligible dark regeneration between pulses. Light monitors are shown below trace. See Figure S2 for spectra and intensities of light.

(B) Protocol for quantifying the magnitude of the persistent response as a function of wavelength. Test wavelengths were alternated with a "reset" wavelength of 560 nm to establish a baseline. The intensities of all stimuli ($1 \times 10^9 - 2 \times 10^9$ photons μm^{-2} s^{-1}) were sufficient to produce a saturated persistent response at each wavelength tested.

(C) Population data from protocol in (B) for difference in current from baseline (left), difference in current normalized to minimum and maximum for each cell (middle), and current noise in the same period (standard deviation normalized to minimum and maximum; right). Connected markers are individual cells. All experiments were in voltage clamp (-80 mV) at 23 °C with synaptic transmission blocked.

A defining feature of a bistable pigment is its activation from a single conformational state, and we tested whether this is true of melanopsin in ipRGCs. A pigment state can be defined by its spectral sensitivity, which is described by a mathematical nomogram whose only free parameter is the λ_{max} (Govardovskii et al., 2000). The spectral sensitivity of a pigment state is conferred upon the photoreceptor to give the cellular action spectrum (e.g., Govardovskii et al., 2000; Hillman et al., 1983; Makino et al., 1999). Electrophysiological measurement of the action spectrum is generally more sensitive, by orders of magnitude, than biochemical measurements of the absorption spectrum (Govardovskii et al., 2000). The sensitivity afforded by electrophysiology is particularly important for delineating the properties of native melanopsin because this pigment is expressed sparsely in ipRGCs (Do et al., 2009) and these cells are few in number (Berson et al., 2010; Ecker et al., 2010).

We measured the ipRGC action spectrum under two conditions: dark adaptation (no activation) and atop a background light of 600 nm (a wavelength that minimizes the persistent response). We found that the action spectrum of dark-adapted ipRGCs was described by a single-state nomogram with a λ_{max} of 471 ± 2 nm (n = 6 cells; Figure 2.4), comparable to most prior reports (Lucas et al., 2014). With the 600-nm background light, the action spectrum was again described by a single-state nomogram (Figure 2.4). Unexpectedly, this nomogram was blue shifted to have a λ_{max} of 453 ± 1 nm (n = 6 cells; same cells as above), which indicates the presence of a pigment state that is distinct from that observed in darkness. We observed this spectral shift in each cell tested (n = 4 cells at 35 °C and 2 cells at 23 °C with no detectable variation with temperature; λ_{max} differs between darkness and 600-nm background light with $p < 0.001$). A pulse of long-wavelength conditioning light was also effective in producing the blue-shifted pigment state (Figure S3). These experiments indicate that melanopsin activates from more than one state and is therefore not bistable.

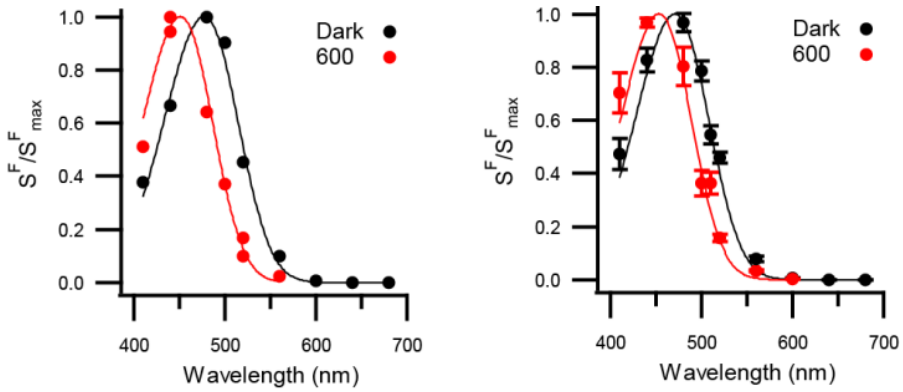

Figure 2.4. Two Silent States of Melanopsin Detected in IpRGCs

Left: the spectral sensitivity (i.e., action spectrum) of a single ipRGC measured in darkness as well as during a 600-nm background light (black and red markers, respectively). Plotted is the sensitivity of the cell to dim flashes of each test wavelength (S^F, in pA photons^{-1} μm^2) normalized to the maximum for this cell (S^F_{max}). Continuous curves are single state nomograms fit to the data with λ_{max} = 471 nm (darkness) and 454 nm (600-nm background). Right: population averages for the same conditions (mean ± SEM; n = 6 cells) with λ_{max} = 471 nm (darkness, the "cyan" state) and 453 nm (600-nm background, the "violet" state). 600-nm background was delivered at $4 \times 10^6 - 7 \times 10^8$ photons μm^{-2} s^{-1}. Measurements were made at 35 °C and 23 °C with no detectable variation in λ_{max} with temperature. Synaptic transmission was blocked and the holding voltage was -80 mV. See also Figure S3.

When we delivered a background of 440-nm light (a wavelength that produces a large persistent response), ipRGCs exhibited an action spectrum that is broader than that of a single pigment state. Rather, it is described by the weighted sum of the 471-nm (69% ± 7%) and 453-nm (31% ± 7%) nomograms (n = 4 cells at 23 °C; Figure 2.5A). To test the effect of all visible wavelengths, we used a background of xenon light (1.5×10^{-7} μW μm^{-2}, equivalent to 50 lux, an intensity similar to dim room light). Again, ipRGCs displayed an action spectrum that was described by the weighted sum of the 471-nm (59% ± 8%) and 453-nm (41% ± 8%) nomograms (n = 5 cells at 35 °C and 4 cells at 23 °C with no detectable variation with temperature; Figure 2.5B). Collectively, these data suggest that the ipRGC action spectrum reflects one pigment state, another, or both depending on illumination conditions (Figures 2.4 and 2.5). In other words, melanopsin activates from two states, which we refer to as cyan (λ_{max} = 471 nm) and violet (453 nm).

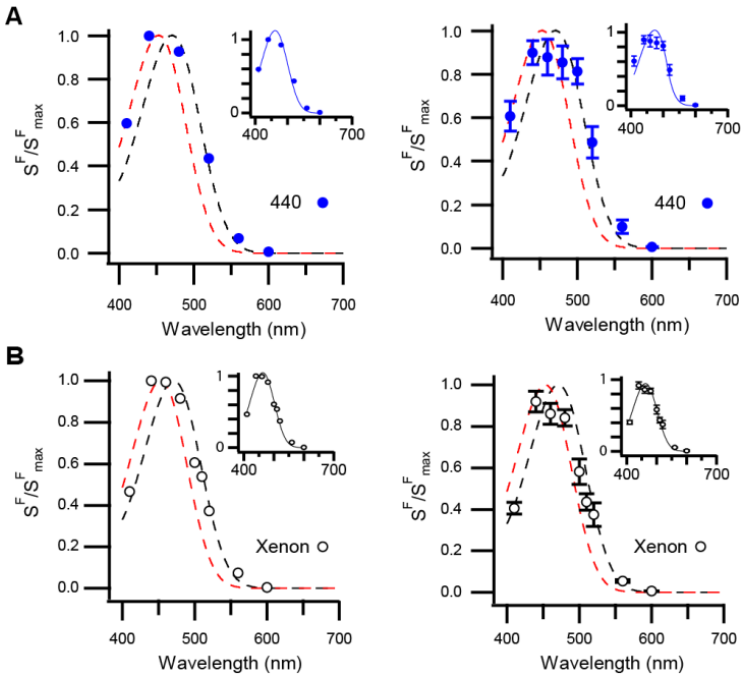

Figure 2.5. Broadened Spectral Sensitivity of IpRGCs due to Activation of Melanopsin from Two Silent States

(A) Action spectrum of a single ipRGC (left) and the population (right) on a background of short-wavelength light (440 nm). Dashed lines are single-state nomograms used to fit the spectra in Figure 2.4 (black, representing the cyan state and red, the violet state). Insets: same data but the curves are weighted sums of the same two nomograms (left: 53% cyan and 47% violet; right: 69% cyan and 31% violet).

(B) Action spectrum measured from a single ipRGC (left) and the population (right) on a background of white (xenon) light. Black and red dashed lines represent the cyan and violet nomograms, respectively. Insets: same data but each curve is the weighted sum of the two nomograms for the cyan and violet states (left: 60% cyan and 40% violet; right: 59% cyan and 41% violet). Background lights were $1 \times 10^5 - 7 \times 10^5$ photons μm^{-2} s^{-1} (440 nm) and 1.5×10^{-7} μW μm^{-2} (equivalent to 50 lux; xenon). Synaptic transmission was blocked. Experiments were performed at 35 °C and 23 °C, with no detectable difference between these conditions detected. Holding voltage was -80 mV. All error bars represent SEM.

Uniformity of Phototransduction Evoked from Two Silent States of Melanopsin

To determine whether ipRGCs respond differently to photon absorption by the cyan and violet states, we generated a dominant fraction of the violet state or a majority fraction of the cyan state using background lights (600 and 440 nm, respectively; Figures 2.4 and 2.5A) and probed transduction with dim flashes (480 nm; Figure 2.6A). We calibrated the intensities of the two backgrounds to produce a comparable level of activation, and thus adaptation, in ipRGCs (Supplemental Experimental Procedures; Do and Yau, 2013; Wong et al., 2005). Without such calibration, differences in the responses could arise from a difference in adaptation rather than the identity of the pigment state. This consideration also precluded us from using darkness for comparison with the long-wavelength background—although darkness yields a pure cyan state, it produces no adaptation. Dim-flash responses evoked on these backgrounds had indistinguishable sensitivities and kinetics (Figures 2.6B and 2.6C). Comparing 440- and 600-nm backgrounds, sensitivities were $1.1 \pm 0.3 \times 10^{-6}$ versus $1.0 \pm 0.3 \times 10^{-6}$ pA photon^{-1} μm^2 ($p = 0.56$), while time constants were 1.4 ± 0.3 versus 1.6 ± 0.2 sec (τ_1 of a fit using the convolution of two exponentials; $p = 0.36$) and 8.7 ± 2.8 versus 7.5 ± 1.3 sec (τ_2; $p = 0.52$; $n = 5$ cells; see also Do et al., 2009). Thus, we did not detect a dependence of downstream signaling on silent states. Equivalent activation from the cyan and violet states, which are separated by ~20 nm, broadens the wavelength tuning of ipRGCs. This spectral separation is comparable to that between the red (λ_{max} = 552 nm) and green (530 nm) cone pigments that serves human color vision (Merbs and Nathans, 1992). Here, this separation exists within a single pigment.

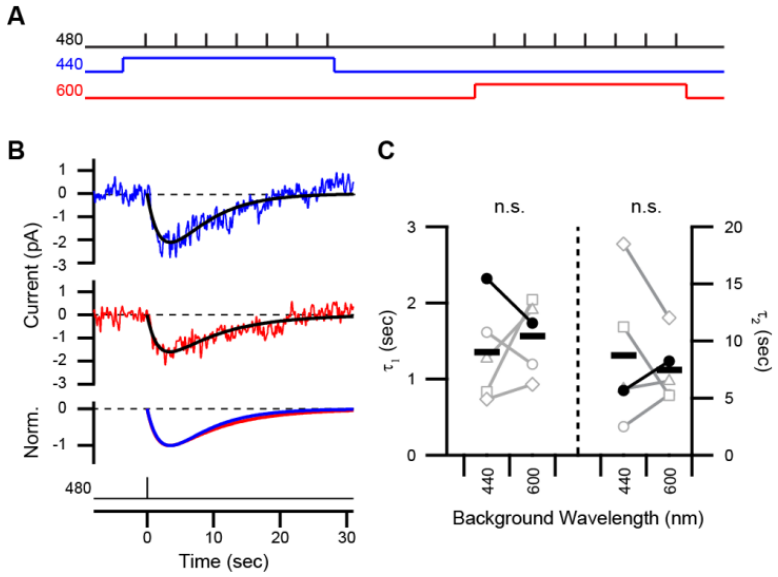

Figure 2.6. Indistinguishable Activation from Two Silent States of Melanopsin

(A) Schematic of the protocol used to compare responses evoked from the cyan and violet states. A 440-nm background generates a majority fraction of the cyan state and a 600-nm background generates a dominant fraction of the violet state. Backgrounds were matched in intensity to produce equivalent activation of ipRGCs and presented in random order (3 and 2 cells with 440 and 600 nm first, respectively).

(B) Dim-flash responses evoked on 440- and 600-nm backgrounds (blue and red traces, respectively). Traces are the average of seven trials. Fits are convolutions of two exponentials $A(e^{-t/\tau_1} - e^{-t/\tau_2})$, shown normalized to their peaks in the bottom panel (time constants for blue and red traces: τ_1, 2.3 and 1.7 s; τ_2, 5.7 and 7.5 s). Light monitors are below.

(C) Time constants from the population of cells (closed markers for the cell in B). "n.s." is lack of statistical significance. Background lights were 9×10^5 photons μm^{-2} s^{-1} (440 nm) and 1×10^8 photons μm^{-2} s^{-1} (600 nm). Synaptic transmission was blocked in all experiments, which were performed at 23 °C. Holding voltage was -80 mV.

Photoequilibrium of Melanopsin States Supports Temporal and Chromatic Integration

Our experiments suggest the following new view of melanopsin function in the mammalian retina. Dark-adapted ipRGCs contain melanopsin in the cyan state (Figure 2.4). Light produces an equilibrium of cyan, violet, and signaling "meta" states. The photoequilibrium fractions of these states are determined by their spectral sensitivities and the wavelength of illumination. Photon absorption by one state causes it to isomerize to another. Therefore, short wavelengths produce a photoequilibrium that favors the meta state (λ_{max} = 476 nm; Matsuyama et al., 2012) because it absorbs these wavelengths less effectively than the cyan (471 nm) and violet (453 nm) states. On the other hand, long wavelengths produce a photoequilibrium with a dominant violet state, because this state absorbs long wavelengths least effectively. The violet state is electrically silent, or largely silent, since it is formed by wavelengths that decrease ipRGC activity (Figures 2.2 and 2.3) and its isomerization activates ipRGCs (Figures 2.4 and 2.6). Thus, our biophysical measurements indicate that native melanopsin is tristable, possessing two silent states and one signaling state.

This view is inconsistent with biochemical experiments on melanopsin (Koyanagi et al., 2005; Newman et al., 2003; Shirzad-Wasei et al., 2013; Walker et al., 2008) with the exception of a study by Shichida and colleagues (Matsuyama et al., 2012). This study demonstrated that melanopsin's ground state ("melanopsin," λ_{max} = 467 nm, containing 11-*cis* retinal) photoequilibrates with the signaling state ("metamelanopsin," 476 nm, all-*trans* retinal). There was also evidence of photoequilibration between metamelanopsin and a third state, called "extramelanopsin" (446 nm) that contained 7-*cis* retinal. In other words, melanopsin ⇌ metamelanopsin ⇌ extramelanopsin, with direct conversion between melanopsin and extramelanopsin neither detected nor expected due to energetic constraints (Matsuyama et al., 2012). A physiological role for extramelanopsin was considered hypothetical because pigments containing 7-*cis* retinal have not been thought to exist in nature (Matsuyama et al., 2012; Sekharan and Morokuma, 2011) and these biochemical experiments were performed under highly reduced conditions (e.g., the pigment was truncated, expressed heterologously, and solubilized in detergent). On the other hand, extramelanopsin does resemble the violet state that we observe in ipRGCs (λ_{max} = 446 nm and 453 nm, respectively; Figure S4).

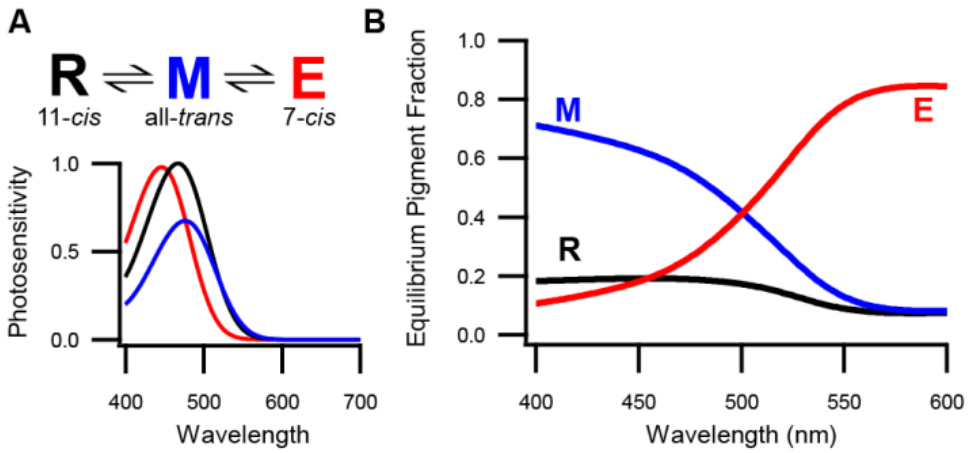

Figure 2.7. A State Model for Tristable Melanopsin

(A) State diagram of melanopsin (top) based on parameters measured biochemically from purified pigment (Matsuyama et al., 2012). Shown are melanopsin (R), metamelanopsin (M), and extramelanopsin (E) with chromophores designated. Below are plotted the relative photosensitivities (i.e., products of the extinction coefficients and quantum efficiencies) of these states as a function of wavelength. Only two model parameters are experimentally undefined: the quantum efficiency of the E state and the fraction of M isomerizations that yields the R versus E state (set at 0.4 and 0.5, respectively; Experimental Procedures). Only the latter parameter is not depicted here. Direct photoconversion between the R and E states is unlikely given energetic constraints of chromophore isomerization.

(B) Predicted equilibrium fraction of each pigment state as a function of wavelength. Lines show the R state (black), M state (blue), and E state (red). See also Figure S4.

To make this comparison between melanopsin biochemistry and ipRGC physiology quantitative, we developed a numerical model that uses parameters measured from purified melanopsin to predict the photoequilibrium of pigment states arising from any excitation spectrum (Experimental Procedures; Figures 2.7A and S4; Matsuyama et al., 2012). The model predicts that short wavelengths drive most pigment into the metamelanopsin ("M") state, which parallels our experimental finding that these wavelengths generate the largest persistent responses (which reflect the M-like meta state; Figure 2.3). The remaining pigment is predicted to be divided between the melanopsin ("R") and extramelanopsin ("E") states (Figure 2.7B). For example, at 440 nm, the E state should compose 46% of the silent states. Our experiments on ipRGCs are in general agreement: Illumination at this wavelength produces a photoequilibrium in which ~31% of the pigment occupies the E-like violet state (Figure 2.5A). For long wavelengths, the model predicts that there is a small fraction of the M and R states as well as a large fraction of the E state (Figure 2.7B), which accords with our observation that these wavelengths produce the smallest persistent responses in ipRGCs (Figures 2.2 and 2.3). At 600 nm, the E state is predicted to account for 92% of the silent states. When delivered to ipRGCs, light of this wavelength produces a photoequilibrium in which the only detectable silent state is the E-like violet state (Figure 2.4 and Experimental Procedures). Thus, mammalian melanopsin appears to be tristable in its native environment as well as when purified, and tristability can account for the integrative properties of ipRGCs that we observe.

Tristability Confers Unique Properties to Melanopsin under Diverse Illumination Conditions

To investigate how tristability operates under diverse illumination conditions, we assessed model outputs for common light sources (Figure 2.8A; Johnsen et al., 2006). Remarkably, despite having diverse spectra, these sources are predicted to have practically identical effects on the photoequilibrium of melanopsin states, resembling monochromatic short-wavelength light in producing a majority fraction of the M state and roughly even fractions of the R and E states (Figure 2.8B).

We generated two additional models to compare the properties of tristable and bistable visual pigments. The first is a hypothetical, "bistable melanopsin" that lacks the E state (Figure 2.8C) and the second is Drosophila rhodopsin (Figure 2.8D). All relevant biochemical parameters are known for both

models (Matsuyama et al., 2012; Ostroy, 1978; Stavenga, 2010). The principal difference between these bistable models is that the spectral sensitivities of the ground and signaling states are similar for melanopsin (λ_{max} = 467 and 476 nm, respectively) but different for rhodopsin (480 and 570 nm). We find that the photoequilibrium of bistable melanopsin, but not of rhodopsin, displays a high degree of invariance across diverse lighting spectra. By contrast, the photoequilibrium of rhodopsin, but not of bistable melanopsin, can have a nearly pure fraction of either the silent state or the signaling state. Tristable melanopsin is distinct from bistable pigments in that it displays both spectral invariance and state purity (Figure 2.8B). Furthermore, the approach of tristable melanopsin to photoequilibrium is slower than that of bistable melanopsin or Drosophila rhodopsin (by 1.6- and 6.1-fold, respectively), consistent with the integrating nature of non-image vision.

Figure 2.8. Melanopsin Tristability under Diverse Lighting Conditions

(A) Measures spectra of various, common light sources (in photons μm^{-2} s^{-1} nm^{-1} prior to normalization).

(B) Left: state diagram and relative photosensitivities as displayed in Figure 2.7A. Middle: predicted equilibrium fractions of melanopsin states for monochromatic illumination at two wavelengths (440 and 560 nm). Right: predicted equilibrium fractions of melanopsin states for broadband illumination by the sources shown in (A).

(C) Same as (B) but for a hypothetical bistable melanopsin with only the ground state (R) and metamelanopsin (M).

(D) Same as (B) but for *Drosophila* rhodopsin (R) and metarhodopsin (M). Midday and sunset in (A) are courtesy of Sönke Johnsen (Johnsen et al., 2006).

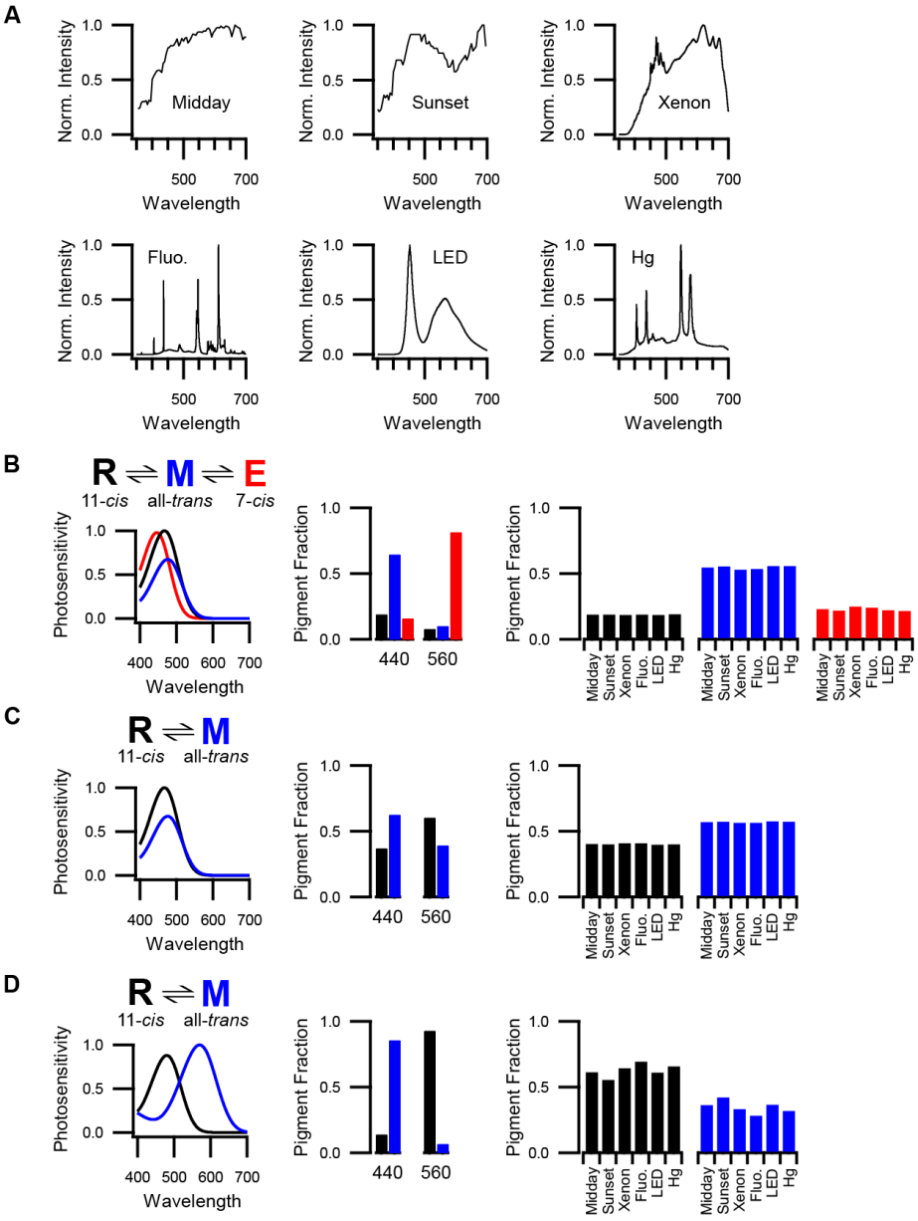

Figure 2.8 (Continued).

Discussion

We have found that melanopsin signaling in ipRGCs exhibits a high degree of signal integration that is consistent with the characteristics of non-image vision. Melanopsin activity generates persistent responses that support temporal integration over many minutes. We know of no other sensory cell that exhibits such a high degree of temporal integration. Notably, ipRGCs accomplish this integration with signaling components that are employed in other systems to resolve signals on a millisecond time scale (Angueyra et al., 2012; Dorlöchter and Stieve, 1997; Henderson et al., 2000). Furthermore, the persistent responses of ipRGCs are activated by a wider range of wavelengths than expected from a single visual pigment (Govardovskii et al., 2000) even though phototransduction relies exclusively on melanopsin (Hattar et al., 2003; Lucas et al., 2003; Melyan et al., 2005; Panda et al., 2005; Qiu et al., 2005). We have provided evidence that this chromatic integration reflects the activation of melanopsin from two spectrally distinct silent states, which we have called cyan and violet.

The violet state of melanopsin resembles the E state that Shichida and colleagues defined biochemically for purified melanopsin (Matsuyama et al., 2012). The E state is unusual in using 7-*cis* retinal, a chromophore that has not yet been found in a native visual pigment. Molecular dynamics simulations have predicted that 7-*cis* retinal would produce an inactive pigment (Sekharan and Morokuma, 2011). Therefore, like the violet state, the E state is expected to be silent. Moreover, rhodopsins that are experimentally reconstituted with 11-*cis* or 7-*cis* retinal differ in the initial stages of photoactivation but converge before G-protein engagement (Shichida et al., 1991). This is consistent with our observation of indistinguishable activation from the cyan and violet states in ipRGCs (Figure 2.6). Thus, extramelanopsin and the violet state are likely to be one and the same. Purification of 7-*cis* retinal from ipRGCs would provide a test of this idea, though such experiments are challenging due to the miniscule amount of melanopsin in the retina (Berson et al., 2010; Do et al., 2009; Ecker et al., 2010).

Some studies have suggested that mammalian melanopsin has only one silent state and is bistable (Melyan et al., 2005; Mure et al., 2009; Mure et al., 2007; Panda et al., 2005; Qiu et al., 2005; Shirzad-Wasei et al., 2013). Other studies, including our own, have not detected any photoequilibration of melanopsin among stable states (Do et al., 2009; Do and Yau, 2013; Fu et al., 2005; Mawad and Van

Gelder, 2008; Qiu et al., 2005; Sexton et al., 2012). Much of this disagreement may stem from properties of tristability that we have described here. First, because all three melanopsin states are tuned to short wavelengths, long-wavelength illumination must be intense or prolonged to produce an obvious fraction of the violet state and thus cellular deactivation (Figure S4). Second, the largest persistent responses we observed were approximately 30 pA and most were <10 pA, which can be difficult to detect. These responses are also associated with decreases in input resistance and photosensitivity (Figures 2.2C and 2.3A), which are typical criteria for terminating a recording session (Do et al., 2009; Do and Yau, 2013). Finally, even though persistent currents are small, they are often able to drive ipRGCs into depolarization block due to the overall high input resistance of these cells (Figure 2.2C; Do et al., 2009; Do and Yau, 2013; Schmidt and Kofuji, 2009); these activated but weakly- or non-spiking cells would not be apparent in extracellular recordings (Mawad and Van Gelder, 2008; Sexton et al., 2012).

Melanopsin tristability appears to have advantages for non-image vision. First, photoequilibration of melanopsin among signaling and silent states supports the sustained activity of ipRGCs by maintaining a fraction of pigment molecules that are available for activation. By contrast, the monostable rod and cone pigments spontaneously dissociate into opsin and chromophore after a single activation, thereby losing photosensitivity. Because pigment regeneration requires a slow series of reactions that take place in accessory cells, rods and cones have a limited intrinsic capacity for sustained signaling (Wang and Kefalov, 2011). Our observations of the violet state and its activation provide evidence for the light-driven regeneration of melanopsin in ipRGCs. Previously, we reported that ipRGCs have a surplus of melanopsin for generating acute responses to light, in that each cell expresses approximately ten-fold more molecules than are needed to produce the saturated photocurrent (Do et al., 2009; Do and Yau, 2013). Therefore, we expect tristability to be especially important for pigment regeneration over the long time scales that are characteristic of non-image visual responses (Mrosovsky and Hattar, 2003; Wong, 2012).

With regard to maintaining pigment availability, tristability is not expected to differ from bistability, which raises the question of whether tristability provides unique advantages. Our work indicates that tristable melanopsin displays an activation level that is similar across a variety of broadband spectra ("spectral invariance") and can range from a small minimum to a large maximum ("state purity").

By contrast, a bistable pigment can display either spectral invariance or state purity—depending on the relative wavelength sensitivity of its two states—but not both. State purity facilitates the fine-tuning of pigment function to behavioral needs. For example, the balance between activation and deactivation can be flexibly altered through the expression of screening pigments that are upstream of the photoreceptors, a strategy that is used by many species for adaptation to diverse habitats (Cronin et al., 2001; Hardie and Postma, 2008). Tristable melanopsin has two additional features that distinguish it from bistable pigments. First, its spectral sensitivity is broadened by activation from two silent states, which confers a degree of wavelength integration. Second, tristable melanopsin approaches photoequilibrium with an extended time course, which imposes a low-pass filter on visual signals. Thus, tristability endows melanopsin signaling with a unique set of properties that is consistent with the integrative nature of non-image vision.

A notable implication of our study is that no type of illumination can produce a pure population of melanopsin's ground state. Nevertheless, this is the only state that is detected in dark-adapted ipRGCs biochemically (Sexton et al., 2012; Walker et al., 2008) and in our own biophysical experiments (Figure 2.4). Therefore, melanopsin is likely to return to the ground state through a light-independent mechanism. We expect such dark regeneration to be slow because the persistent response (reflecting the meta state) can be observed for many minutes following its induction by light, and the action spectra of ipRGCs (reflecting the fractional occupancy of cyan and violet states) agree with predictions from our state model, which only includes light-driven transitions. Melanopsin can be regenerated by the administration of exogenous chromophore (Do et al., 2009; Fu et al., 2005; but see Sexton et al., 2012), raising the possibility that formation of the ground state involves bleaching and regeneration.

In summary, ipRGCs respond to common lighting conditions by producing signals that sum over minutes, regenerating melanopsin molecules from the signaling state, and expanding their spectral sensitivity. We have presented evidence that these phototransduction properties share a common origin in melanopsin tristability; namely, the photoequilibration of melanopsin among silent cyan, silent violet, and signaling meta states. It is presently unknown if tristability is unique to mammalian melanopsin or is also a property of other visual pigments. Regardless, melanopsin tristability imparts broadband and

sustained signals to the many processes that have been ascribed to ipRGCs, from neural and vascular development (Rao et al., 2013; Renna et al., 2011) to the regulation of mood and the circadian clock (reviewed by Do and Yau, 2010; Lucas et al., 2014). Tristability is also expected to increase the integrative capacity of cells that are rendered photosensitive through the optogenetic use of melanopsin, and permit these cells to be acutely deactivated with long-wavelength illumination (Lin et al., 2008; Ye et al., 2011).

Experimental Procedures

Detailed procedures for individual experiments are included in Supplemental Experimental Procedures.

Tissue

All procedures were approved by the Institutional Animal Care and Use Committee of Boston Children's Hospital. BAC-transgenic mice (either sex, postnatal days 20-140, housed in a 12-hr light/12-hr dark cycle) with ipRGCs labeled by expression of tdTomato from the melanopsin gene locus were used (Do et al., 2009). Mice were dark adapted for > 1.5 hr and experiments were performed between zeitgeber times 3 and 10 (where 0 is lights on). Under dim red light, animals were anesthetized with Avertin, enucleated, and euthanized. The retina was mechanically freed from the retinal pigment epithelium and vitreous humor in carbogenated Ames' medium (i.e., equilibrated with 95% O_2/5% CO_2). The retina was flattened with peripheral cuts and held in the recording chamber, photoreceptors down, by a platinum-iridium frame strung with lycra fibers or a coverslip coated with poly-L-lysine.

Electrophysiology

The flat-mount retina was superfused with carbogenated Ames' medium at ~5 ml/min on the stage of an upright microscope. Cells were viewed with differential interference contrast optics using infrared transillumination (850-nm center wavelength and 30-nm width at half maximum). IpRGCs were visualized with ~1 s of light (25-nm bandpass centered on 545 nm, 1×10^{10} photons μm^{-2} s^{-1}; Figure S2) and the overlying inner limiting membrane was mechanically removed. Cells were dark adapted for > 15 min before data were collected. Pipettes (2-6 MΩ) were wrapped with parafilm to reduce capacitance. Series resistance (generally ≤ 50 MΩ) was monitored. Integrity of the perforated-patch configuration was tested with periodic test flashes and, in some cases, brief visualization of lucifer yellow (which does not

permeate amphotericin B) at the end of the experiment. Recordings were performed near physiological temperature (35 °C ± 1 °C) or, for additional stability, at room temperature (~23 °C). Temperature was monitored with a thermistor in the recording chamber. Recordings were low-pass filtered at 4-10 kHz (current clamp) or 2 kHz (voltage clamp) and sampling exceeded the Nyquist minimum. Analysis was performed using Clampfit and Igor Pro. Nearly all ipRGCs we recorded are likely to be of the M1 subtype based on their bright tdTomato labeling; large intrinsic light responses (typically > 100 pA); wide, highly accommodating action potentials; and, often dendrites that could be seen extending into the inner plexiform layer (Do et al., 2009; Do and Yau, 2013; Ecker et al., 2010; Schmidt and Kofuji, 2009; Xue et al., 2011). The few apparently non-M1 ipRGCs encountered were not overtly different with regard to melanopsin tristability, exhibiting persistent responses to short-wavelength light and shifted action spectra during or after long-wavelength light. Solutions are detailed in Supplemental Experimental Procedures.

Optical Stimulation

Light from 75-W xenon arc lamps or a 100-W mercury halide lamp was filtered to deplete heat while selecting intensity and wavelength. Delivery through a 40× objective produced a uniform field (480-μm diameter) centered on the soma. Electromechanical shutters controlled stimulus timing. Light stimuli were measured at the site of the preparation using a calibrated radiometer and spectrometer. Light delivered through 10-nm bandpass filters were assumed to be of the center wavelength; for broader filters, photon flux was calculated from measured spectra (Figures 2.8 and S2). Photometric units were calculated using the CIE standard photopic luminosity function (Sharpe et al., 2005). "Flashes" are impulse stimuli (i.e., duration and intensity can be interchanged to give the same response).

Numerical Model of Melanopsin Tristability

The distribution of biochemically defined melanopsin states (Matsuyama et al., 2012) as a function of wavelength was estimated with a numerical simulation in which occupancy of each state is calculated with each time step. The states are melanopsin (R), metamelanopsin (M), and extramelanopsin (E). A state depopulates if a molecule in that state absorbs a photon and isomerizes (thus converting to another state). A state populates if a molecule in an adjoining state absorbs a photon

and isomerizes. R and E both interconvert directly with M but not each other, in accordance with biochemical data on purified melanopsin (Matsuyama et al., 2012) and the likelihood, given energetic constraints, that the transition from one *cis* isoform to another occurs via the all-*trans* conformation. For each state, photon absorption is governed by the extinction coefficient (ε, in units of cm^2 $mol^{-}1$), which has a spectral dependence, A(λ). Following photon absorption, the probability of isomerization is given by the quantum efficiency (ϕ). The equations are

$$f_{n+1}^{R} = f_n^R + f^{M\to R}[\ln(10) \times I(\lambda) \times f_n^M \times \varepsilon_{\mathrm{M}} \times \mathrm{A_M}(\lambda) \times \phi_{\mathrm{M}}] - [\ln(10) \times I(\lambda) \times f_n^R \times \varepsilon_{\mathrm{R}} \times \mathrm{A_R}(\lambda) \times \phi_{\mathrm{R}}]$$

$$f_{n+1}^{M} = f_n^M + [\ln(10) \times I(\lambda) \times f_n^R \times \varepsilon_{\mathrm{R}} \times \mathrm{A_R}(\lambda) \times \phi_{\mathrm{R}}] + [\ln(10) \times I(\lambda) \times f_n^E \times \varepsilon_{\mathrm{E}} \times \mathrm{A_E}(\lambda) \times \phi_{\mathrm{E}}] - [\ln(10) \times I(\lambda) \times f_n^M \times \varepsilon_{\mathrm{M}} \times \mathrm{A_M}(\lambda) \times \phi_{\mathrm{M}}]$$

$$f_{n+1}^{E} = f_n^E + f^{M\to E}[\ln(10) \times I(\lambda) \times f_n^M \times \varepsilon_{\mathrm{M}} \times \mathrm{A_M}(\lambda) \times \phi_{\mathrm{M}}] - [\ln(10) \times I(\lambda) \times f_n^E \times \varepsilon_{\mathrm{E}} \times \mathrm{A_E}(\lambda) \times \phi_{\mathrm{E}}]$$

where f^R, f^M, and f^E are the fractional occupancies of each state and sum to 1. We typically begin our simulation with $f_0^R = 1$, reflecting dark adaptation but the equilibrium state is insensitive to the initial conditions. $f^{M\to R}$ is the fraction of M isomerizations that yields R and $f^{M\to E}$ is the fraction that yields E; $f^{M\to R} + f^{M\to E} = 1$. $I(\lambda)$ is the light intensity in mol photons cm^{-2} s^{-1} nm^{-1} (higher intensities simply give faster approaches to equilibrium; Figure S4). The *ln(10)* term originates with the Beer-Lambert law governing absorbance of light. Equilibrium was defined at the point when the fraction of each state changes by $< 1.0 \times 10^{-20}$ between time steps (of at least 1 ms). For A(λ), we use the standard spectral template for A1-based pigments, including both α and β absorption bands (Govardovskii et al., 2000), with the λ_{max} values reported for purified, mammalian melanopsin (R = 467 nm, M = 476 nm, and E = 446 nm; Matsuyama et al., 2012).

All model parameters except for ϕ_{E} and $f^{M\to R}$ (thus also $f^{M\to E}$) have been defined by Shichida and colleagues (Matsuyama et al., 2012). Most natural pigments have a quantum efficiency of activation near 0.7 (Dartnall, 1972); where it has been studied, the quantum efficiency of deactivation for bistable pigments is as low as 0.2 (Cronin and Goldsmith, 1982; Matsuyama et al., 2012). There is little

information available on the quantum efficiency of pigments containing 7-*cis* retinal (Shichida et al., 1991), like the E state. For our model, we selected a ϕ_E of 0.4, which is intermediate between the values for melanopsin and metamelanopsin (Matsuyama et al., 2012), and an $f^{M\to R}$ (and thus $f^{M\to E}$) of 0.5.

We do not consider light-independent transitions between states because the thermal decay of the M and E states appears to be negligible over the time scales of our experiments, especially at 23 °C. For instance, the persistent response (reflecting the signaling, or M state) is stable for minutes at 35 °C and 23 °C (Figures 2.1D and 2.2A) and the spectral sensitivity of the violet state (the physiological homolog of the biochemical E state) can be measured from ipRGCs in a >10 min window following a conditioning light that produces it (at 23 °C, Figure S3). Furthermore, many of our experiments are performed with continuous illumination, which maintains the photoequilibrium distribution of melanopsin states.

Numerical Models of Bistable Pigments

The equations that compose the models of bistable pigments are

$$f_{n+1}^{R} = f_n^{R} + [\ln(10) \times I(\lambda) \times f_n^{M} \times \varepsilon_{\mathrm{M}} \times \mathrm{A_M}(\lambda) \times \phi_{\mathrm{M}}] - [\ln(10) \times I(\lambda) \times f_n^{R} \times \varepsilon_{\mathrm{R}} \times \mathrm{A_R}(\lambda) \times \phi_{\mathrm{R}}]$$

$$f_{n+1}^{M} = f_n^{M} + [\ln(10) \times I(\lambda) \times f_n^{R} \times \varepsilon_{\mathrm{R}} \times \mathrm{A_R}(\lambda) \times \phi_{\mathrm{R}}] - [\ln(10) \times I(\lambda) \times f_n^{M} \times \varepsilon_{\mathrm{M}} \times \mathrm{A_M}(\lambda) \times \phi_{\mathrm{M}}]$$

Variables are identical to those given for the tristable melanopsin model. For the hypothetical "bistable melanopsin," all values are the same as for the tristable melanopsin model. For *Drosophila* rhodopsin, ε_R = 35,000 $cm^2\,mol^{-1}$ and ε_M = 56,000 $cm^2\,mol^{-1}$ (Ostroy, 1978). ϕ_M has been measured to be 0.71 of ϕ_R (Stavenga, 2010). ϕ_R itself has not been directly measured but its proportionality with ϕ_M is sufficient for accurate prediction of photoequilibrium pigment fractions. $A_R(\lambda)$ and $A_M(\lambda)$ are Govardovskii nomograms (Govardovskii et al., 2000) with λ_{max} values of 480 and 570 nm, respectively, which fit *Drosophila* pigment states (Stavenga, 2010).

Statistical Methods

We used non-parametric statistics, employing the Mann-Whitney U test for unpaired data and the Wilcoxon signed-rank test for paired data. To compare more than two groups with repeated measures, we used the Friedman test and a post-hoc Wilcoxon signed-rank test with Bonferroni correction.

Supplemental Information

Supplemental Information includes Supplemental Experimental Procedures and five figures and can be found with this article online at http://dx.doi.org/10.1016/j.neuron.2015.02.011. The Supplemental Information has also been included in Appendix 1 of this dissertation.

Author Contributions

A.J.E. and M.T.H.D. designed experiments, which were conducted by A.J.E., and wrote the paper.

Acknowledgments

We thank T. Matsuyama, Y. Shichida, D.D. Oprian, R.I. Wilson, C.J. Woolf, and laboratory members (M.C. Brown, G.S. Bryman, A. Liu, and E.S. Milner) for discussions; and R. Adams, E. Egan, and M. Kwiatkowski for technical assistance. This work was supported by grants from the National Science Foundation (Graduate Research Fellowship, A.J.E.), National Institutes of Health (R01 EY023648, M.T.H.D.; P30 HD18655, Boston Children's Hospital IDDRC; P30 EY012196, Harvard Medical School; and T32 HL007901, HMS Division of Sleep Medicine), the Whitehall Foundation (2011-05-15, M.T.H.D.), and The Karl Kirchgessner Foundation (M.T.H.D.).

Received: November 11, 2014

Revised: January 20, 2015

Accepted: January 29, 2015

Published: March 4, 2015

References

Azuma, K., and Azuma, M. (1985). Absorbance and circular dichroism spectra of 7-*cis* photoproduct formed by irradiating frog rhodopsin. Photochem. Photobiol. 41, 165–169.

Berson, D.M., Dunn, F.A., and Takao, M. (2002). Phototransduction by retinal ganglion cells that set the circadian clock. Science 295, 1070–1073.

Berson, D.M., Castrucci, A.M., and Provencio, I. (2010). Morphology and mosaics of melanopsin-expressing retinal ganglion cell types in mice. J. Comp. Neurol. 518, 2405–2422.

Brainard, G.C., Hanifin, J.P., Greeson, J.M., Byrne, B., Glickman, G., Gerner, E., and Rollag, M.D. (2001). Action spectrum for melatonin regulation in humans: evidence for a novel circadian photoreceptor. J. Neurosci. 21, 6405–6412.

Cronin, T.W., and Goldsmith, T.H. (1982). Quantum efficiency and photosensitivity of the rhodopsin equilibrium metarhodopsin conversion in crayfish photoreceptors. Photochem. Photobiol. 36, 447–454.

Cronin, T.W., Caldwell, R.L., and Marshall, J. (2001). Sensory adaptation. Tunable colour vision in a mantis shrimp. Nature 411, 547–548.

Dacey, D.M., Liao, H.W., Peterson, B.B., Robinson, F.R., Smith, V.C., Pokorny, J., Yau, K.-W., and Gamlin, P.D. (2005). Melanopsin-expressing ganglion cells in primate retina signal colour and irradiance and project to the LGN. Nature 433, 749–754.

Dartnall, H.J.A. (1972). Photosensitivity. In Photochemistry of Vision, H.J.A. Dartnall, ed. (New York: Springer-Verlag), pp. 122–145.

Do, M.T.H., and Yau, K.-W. (2010). Intrinsically photosensitive retinal ganglion cells. Physiol. Rev. 90, 1547–1581.

Do, M.T.H., and Yau, K.-W. (2013). Adaptation to steady light by intrinsically photosensitive retinal ganglion cells. Proc. Natl. Acad. Sci. USA 110, 7470–7475.

Do, M.T.H., Kang, S.H., Xue, T., Zhong, H., Liao, H.W., Bergles, D.E., and Yau, K.-W. (2009). Photon capture and signalling by melanopsin retinal ganglion cells. Nature 457, 281–287.

Ecker, J.L., Dumitrescu, O.N., Wong, K.Y., Alam, N.M., Chen, S.K., LeGates, T., Renna, J.M., Prusky, G.T., Berson, D.M., and Hattar, S. (2010). Melanopsin-expressing retinal ganglion-cell photoreceptors: cellular diversity and role in pattern vision. Neuron 67, 49–60.

Fu, Y., Zhong, H., Wang, M.H., Luo, D.G., Liao, H.W., Maeda, H., Hattar, S., Frishman, L.J., and Yau, K.-W. (2005). Intrinsically photosensitive retinal ganglion cells detect light with a vitamin A-based photopigment, melanopsin. Proc. Natl. Acad. Sci. USA 102, 10339–10344.

Govardovskii, V.I., Fyhrquist, N., Reuter, T., Kuzmin, D.G., and Donner, K. (2000). In search of the visual pigment template. Vis. Neurosci. 17, 509–528.

Güler, A.D., Ecker, J.L., Lall, G.S., Haq, S., Altimus, C.M., Liao, H.W., Barnard, A.R., Cahill, H., Badea, T.C., Zhao, H., et al. (2008). Melanopsin cells are the principal conduits for rod-cone input to non-image-forming vision. Nature 453, 102–105.

Hardie, R.C., and Postma, M. (2008). 1.05 – Phototransduction in microvillar photoreceptors of Drosophila and other invertebrates. In The Senses: A Comprehensive Reference, A.I. Basbaum, ed. (Elsevier Science/Academic Press), pp. 77–130.

Hatori, M., Le, H., Vollmers, C., Keding, S.R., Tanaka, N., Buch, T., Waisman, A., Schmedt, C., Jegla, T., and Panda, S. (2008). Inducible ablation of melanopsin-expressing retinal ganglion cells reveals their central role in non-image forming visual responses. PLoS ONE 3, e2451.

Hattar, S., Lucas, R.J., Mrosovsky, N., Thompson, S., Douglas, R.H., Hankins, M.W., Lem, J., Biel, M., Hofmann, F., Foster, R.G., and Yau, K.-W. (2003). Melanopsin and rod-cone photoreceptive systems account for all major accessory visual functions in mice. Nature 424, 76–81.

Henderson, S.R., Reuss, H., and Hardie, R.C. (2000). Single photon responses in *Drosophila* photoreceptors and their regulation by Ca^{2+}. J. Physiol. 524, 179–194.

Hillman, P., Hochstein, S., and Minke, B. (1983). Transduction in invertebrate photoreceptors: role of pigment bistability. Physiol. Rev. 63, 668–772.

Johnsen, S., Kelber, A., Warrant, E., Sweeney, A.M., Widder, E.A., Lee, R.L., Jr., and Hernández-Andrés, J. (2006). Crepuscular and nocturnal illumination and its effects on color perception by the nocturnal hawkmoth *Deilephila elpenor*. J. Exp. Biol. 209, 789–800.

Koyanagi, M., Kubokawa, K., Tsukamoto, H., Shichida, Y., and Terakita, A. (2005). Cephalochordate melanopsin: evolutionary linkage between invertebrate visual cells and vertebrate photosensitive retinal ganglion cells. Curr. Biol. 15, 1065–1069.

Lin, B., Koizumi, A., Tanaka, N., Panda, S., and Masland, R.H. (2008). Restoration of visual function in retinal degeneration mice by ectopic expression of melanopsin. Proc. Natl. Acad. Sci. USA 105, 16009–16014.

Lucas, R.J., Douglas, R.H., and Foster, R.G. (2001). Characterization of an ocular photopigment capable of driving pupillary constriction in mice. Nat. Neurosci. 4, 621–626.

Lucas, R.J., Hattar, S., Takao, M., Berson, D.M., Foster, R.G., and Yau, K.-W. (2003). Diminished pupillary light reflex at high irradiances in melanopsin knockout mice. Science 299, 245–247.

Lucas, R.J., Peirson, S.N., Berson, D.M., Brown, T.M., Cooper, H.M., Czeisler, C.A., Figueiro, M.G., Gamlin, P.D., Lockley, S.W., O'Hagan, J.B., et al. (2014). Measuring and using light in the melanopsin age. Trends Neurosci. 37, 1–9.

Maeda, A., Ogurusu, T., Shichida, Y., Tokunaga, F., and Yoshizawa, T. (1978). Formation of a 7-*cis* retinal pigment by irradiating cattle rhodopsin at low temperatures. FEBS Lett. 92, 77–80.

Maeda, A., Shichida, Y., and Yoshizawa, T. (1979). Formation of 7-*cis*- and 13-*cis*-retinal pigments by irradiating squid rhodopsin. Biochemistry 18, 1449–1453.

Makino, C.L., Groesbeek, M., Lugtenburg, J., and Baylor, D.A. (1999). Spectral tuning in salamander visual pigments studied with dihydroretinal chromophores. Biophys. J. 77, 1024–1035.

Matsuyama, T., Yamashita, T., Imamoto, Y., and Shichida, Y. (2012). Photochemical properties of mammalian melanopsin. Biochemistry 51, 5454–5462.

Mawad, K., and Van Gelder, R.N. (2008). Absence of long-wavelength photic potentiation of murine intrinsically photosensitive retinal ganglion cell firing *in vitro*. J. Biol. Rhythms 23, 387–391.

Melyan, Z., Tarttelin, E.E., Bellingham, J., Lucas, R.J., and Hankins, M.W. (2005). Addition of human melanopsin renders mammalian cells photoresponsive. Nature 433, 741–745.

Merbs, S.L., and Nathans, J. (1992). Absorption spectra of human cone pigments. Nature 356, 433–435.

Mohawk, J.A., Green, C.B., and Takahashi, J.S. (2012). Central and peripheral circadian clocks in mammals. Annu. Rev. Neurosci. 35, 445–462.

Mrosovsky, N., and Hattar, S. (2003). Impaired masking responses to light in melanopsin-knockout mice. Chronobiol. Int. 20, 989–999.

Mure, L.S., Rieux, C., Hattar, S., and Cooper, H.M. (2007). Melanopsin-dependent nonvisual responses: evidence for photopigment bistability *in vivo*. J. Biol. Rhythms 22, 411–424.

Mure, L.S., Cornut, P.L., Rieux, C., Drouyer, E., Denis, P., Gronfier, C., and Cooper, H.M. (2009). Melanopsin bistability: a fly's eye technology in the human retina. PLoS ONE 4, e5991.

Nelson, D.E., and Takahashi, J.S. (1991). Sensitivity and integration in a visual pathway for circadian entrainment in the hamster (*Mesocricetus auratus*). J. Physiol. 439, 115–145.

Newman, L.A., Walker, M.T., Brown, R.L., Cronin, T.W., and Robinson, P.R. (2003). Melanopsin forms a functional short-wavelength photopigment. Biochemistry 42, 12734–12738.

Ostroy, S.E. (1978). Characteristics of *Drosophila* rhodopsin in wild-type and *norpA* vision transduction mutants. J. Gen. Physiol. 72, 717–732.

Panda, S., Sato, T.K., Castrucci, A.M., Rollag, M.D., DeGrip, W.J., Hogenesch, J.B., Provencio, I., and Kay, S.A. (2002). Melanopsin (*Opn4*) requirement for normal light-induced circadian phase shifting. Science 298, 2213–2216.

Panda, S., Nayak, S.K., Campo, B., Walker, J.R., Hogenesch, J.B., and Jegla, T. (2005). Illumination of the melanopsin signaling pathway. Science 307, 600–604.

Perez-Leon, J.A., Warren, E.J., Allen, C.N., Robinson, D.W., and Brown, R.L. (2006). Synaptic inputs to retinal ganglion cells that set the circadian clock. Eur. J. Neurosci. 24, 1117–1123.

Provencio, I., Jiang, G., De Grip, W.J., Hayes, W.P., and Rollag, M.D. (1998). Melanopsin: An opsin in melanophores, brain, and eye. Proc. Natl. Acad. Sci. USA 95, 340–345.

Provencio, I., Rodriguez, I.R., Jiang, G., Hayes, W.P., Moreira, E.F., and Rollag, M.D. (2000). A novel human opsin in the inner retina. J. Neurosci. 20, 600–605.

Qiu, X., Kumbalasiri, T., Carlson, S.M., Wong, K.Y., Krishna, V., Provencio, I., and Berson, D.M. (2005). Induction of photosensitivity by heterologous expression of melanopsin. Nature 433, 745–749.

Rao, S., Chun, C., Fan, J., Kofron, J.M., Yang, M.B., Hegde, R.S., Ferrara, N., Copenhagen, D.R., and Lang, R.A. (2013). A direct and melanopsin-dependent fetal light response regulates mouse eye development. Nature 494, 243–246.

Renna, J.M., Weng, S., and Berson, D.M. (2011). Light acts through melanopsin to alter retinal waves and segregation of retinogeniculate afferents. Nat. Neurosci. 14, 827–829.

Schmidt, T.M., and Kofuji, P. (2009). Functional and morphological differences among intrinsically photosensitive retinal ganglion cells. J. Neurosci. 29, 476–482.

Schmidt, T.M., and Kofuji, P. (2011). Structure and function of bistratified intrinsically photosensitive retinal ganglion cells in the mouse. J. Comp. Neurol. 519, 1492–1504.

Schmidt, T.M., Chen, S.K., and Hattar, S. (2011). Intrinsically photosensitive retinal ganglion cells: many subtypes, diverse functions. Trends Neurosci. 34, 572–580.

Sekharan, S., and Morokuma, K. (2011). Why 11-*cis*-retinal? Why not 7-*cis*-, 9-*cis*-, or 13-*cis*-retinal in the eye? J. Am. Chem. Soc. 133, 19052–19055.

Sekharan, S., Wei, J.N., and Batista, V.S. (2012). The active site of melanopsin: the biological clock photoreceptor. J. Am. Chem. Soc. 134, 19536–19539.

Sexton, T.J., Golczak, M., Palczewski, K., and Van Gelder, R.N. (2012). Melanopsin is highly resistant to light and chemical bleaching *in vivo*. J. Biol. Chem. 287, 20888–20897.

Sharpe, L.T., Stockman, A., Jagla, W., and Jägle, H. (2005). A luminous efficiency function, V*(λ), for daylight adaptation. J. Vis. 5, 948–968.

Shichida, Y., and Matsuyama, T. (2009). Evolution of opsins and phototransduction. Philos. Trans. R. Soc. Lond. B Biol. Sci. 364, 2881–2895.

Shichida, Y., Kandori, H., Okada, T., Yoshizawa, T., Nakashima, N., and Yoshihara, K. (1991). Differences in the photobleaching process between 7-*cis*- and 11-*cis*-rhodopsins: a unique interaction change between the chromophore and the protein during the lumi-meta I transition. Biochemistry 30, 5918–5926.

Shirzad-Wasei, N., van Oostrum, J., Bovee-Geurts, P.H., Wasserman, M., Bosman, G.J., and Degrip, W.J. (2013). Large scale expression and purification of mouse melanopsin-L in the baculovirus expression system. Protein Expr. Purif. 91, 134–146.

Stavenga, D.G. (2010). On visual pigment templates and the spectral shape of invertebrate rhodopsins and metarhodopsins. J. Comp. Physiol. A Neuroethol. Sens. Neural Behav. Physiol. 196, 869–878.

Takahashi, J.S., Hong, H.K., Ko, C.H., and McDearmon, E.L. (2008). The genetics of mammalian circadian order and disorder: implications for physiology and disease. Nat. Rev. Genet. 9, 764–775.

Walker, M.T., Brown, R.L., Cronin, T.W., and Robinson, P.R. (2008). Photochemistry of retinal chromophore in mouse melanopsin. Proc. Natl. Acad. Sci. USA 105, 8861–8865.

Wang, J.S., and Kefalov, V.J. (2011). The cone-specific visual cycle. Prog. Retin. Eye Res. 30, 115–128.

Wong, K.Y. (2012). A retinal ganglion cell that can signal irradiance continuously for 10 hours. J. Neurosci. 32, 11478–11485.

Wong, K.Y., Dunn, F.A., and Berson, D.M. (2005). Photoreceptor adaptation in intrinsically photosensitive retinal ganglion cells. Neuron 48, 1001–1010.

Wong, K.Y., Dunn, F.A., Graham, D.M., and Berson, D.M. (2007). Synaptic influences on rat ganglion-cell photoreceptors. J. Physiol. 582, 279–296.

Xue, T., Do, M.T.H., Riccio, A., Jiang, Z., Hsieh, J., Wang, H.C., Merbs, S.L., Welsbie, D.S., Yoshioka, T., Weissgerber, P., et al. (2011). Melanopsin signalling in mammalian iris and retina. Nature 479, 67–73.

Ye, H., Daoud-El Baba, M., Peng, R.W., and Fussenegger, M. (2011). A synthetic optogenetic transcription device enhances blood-glucose homeostasis in mice. Science 332, 1565–1568.

Zhu, Y., Tu, D.C., Denner, D., Shane, T., Fitzgerald, C.M., and Van Gelder, R.N. (2007). Melanopsin-dependent persistence and photopotentiation of murine pupillary light responses. Invest. Ophthalmol. Vis. Sci. 48, 1268–1275.

Chapter 3: Consequences of Melanopsin Tristability for the Activation and Adaptation of Intrinsically Photosensitive Retinal Ganglion Cells

Alan Joseph Emanuel and Michael Tri Hoang Do

This chapter describes experiments performed to understand how the persistent response generated by ipRGCs as a result of the tristable nature of melanopsin interacts with activation and adaptation of the phototransduction cascade. The work was conceptualized and initiated by Alan Emanuel and Michael Do. All experiments were completed by Alan Emanuel.

Summary

Intrinsically photosensitive retinal ganglion cells (ipRGCs) respond directly to light due to expression of the pigment, melanopsin. We have previously shown that this pigment, in mice, can be interconverted between three stable states, two of which are silent, and one of which is signaling. The long-lived signaling state (the meta state), which is generated by most light stimuli, produces a response in ipRGCs that outlasts the end of illumination by minutes and allows the cell to temporally integrate. Here, we examine further consequences of melanopsin tristability for ipRGCs by using patch-clamp electrophysiology. Specifically, we investigate how the meta state and its associated persistent response influences subsequent activation and adaptation of ipRGC phototransduction. We found that the persistent response narrowed the intensity range over which ipRGCs encode irradiance. It also caused desensitization. Sensitivity could be recovered by acute reduction of the signaling state by long-wavelength illumination. However, the extent of this recovery was variable from cell to cell. In some cases, long-wavelength illumination further desensitized the cell, likely due to its production of long-lasting adaptation. These experiments suggest that the sensitivity and activation of ipRGCs depend on a balance of pigment fractions and adaptation state.

Introduction

In mammals, a subset of retinal ganglion cells respond directly to light due to their expression of the protein, melanopsin (Berson et al., 2002; Do and Yau, 2010; Lucas et al., 2014). The intrinsic, melanopsin-driven photosensitivity of these intrinsically photosensitive retinal ganglion cells (ipRGCs) is important for non-image-forming visual functions such as entrainment of the circadian clock to the solar cycle and constriction of the pupil in the pupillary light reflex (Lucas et al., 2003; Panda et al., 2002).

We previously demonstrated that light interconverts melanopsin between three stable states in mouse ipRGCs (Emanuel and Do, 2015). Two of these states are silent (the cyan and violet states) and one is signaling (the meta state). Each of these states has a different spectral sensitivity, and therefore the equilibrium pigment fractions generated by exposure to light depends on the spectral content of the light source. White light, as well as short-wavelength light, generates a large fraction of the meta state, whereas long-wavelength light generates a small fraction of the meta state (Emanuel and Do, 2015). One

consequence of the stability of the meta state is that ipRGCs are capable of generating a persistent response that long outlasts the offset of the stimulus, allowing them to integrate light over many minutes (Emanuel and Do, 2015).

It is currently unclear, however, how tristability of the melanopsin molecule affects the activation and adaptation of ipRGCs. The activation of the melanopsin-driven response in ipRGCs depends on two broadly-defined factors. First, it depends on the availability of melanopsin molecules that are able to capture photons and initiate the G protein signaling cascade (Do et al., 2009). Therefore, the number of available melanopsin molecules sets the likelihood of capturing a photon. Furthermore, it sets the absolute possible maximal response, which is the sum of the response produced by each isomerized melanopsin molecule. However, the light response need not reach this maximal response due to the second factor that sets the intensity of the cell: the gain of the response, which is the size of the response to each absorbed photon (Do et al., 2009). In the dark, a single photon produces a response of ~1 pA at body temperature and a response that is 2-3 fold smaller at room temperature (Do et al., 2009). In the presence of light, this gain is reduced (i.e., the cell adapts to produce a smaller response and extend the range over which it can activate; Do and Yau, 2013; Wong et al., 2005).

Production of the meta state, which is already active, reduces the number of melanopsin molecules available for activation. Thus, one may predict that in the presence of a substantial fraction of melanopsin in the meta state that the cell would desensitize due to a decrease in pigment availability. In addition, the active molecules continue to signal and produce a response that resembles that during ongoing phototransduction. This signaling may drive adaptation processes that reduce the gain of the response, further decreasing the sensitivity of the cell (Do and Yau, 2013; Wong et al., 2005). Thus, the persistent activation of melanopsin has the potential both to produce integration of light through summing of the persistent response and to drive adaptation in ipRGCs via reduced pigment availability and adaptation. The balance of integration and adaptation in ipRGCs driven by this response is unknown, but shapes the physiology of these cells during and after illumination. Several studies have sought to address how the melanopsin pigment affects signaling by ipRGCs and their downstream functions but have reached contradictory conclusions (Do et al., 2009; Mawad and Van Gelder, 2008; Mure et al.,

2009; Mure et al., 2007), likely because melanopsin was conceptualized as either a bistable or bleachable pigment. In this chapter, we use quantitative electrophysiological measurements from individual ipRGCs to examine the balance between integration and adaptation, with consideration of our current understanding of melanopsin as a tristable pigment.

Results

To record from ipRGCs, we used a mouse line that expresses the fluorescent protein, tdTomato, under the melanopsin promoter (Do et al., 2009). The cells were identified in the flat mount retina by using brief steps of imaging light (see experimental procedures) and recordings were performed in the perforated-patch configuration to preserve the intrinsic light response, which runs down in whole-cell configuration. All recordings were performed in the presence of antagonists of synaptic transmission to isolate the intrinsic, melanopsin-driven light response from the synaptic light responses that arise from phototransduction in rods and cones. All experiments used full-field (350 μm diameter) illumination.

In order to examine how the generation of the meta state and its associated persistent response change the activation of ipRGCs, we measured the intensity-response relation of their intrinsic responses using flashes of short- and long-wavelength light at near-physiological temperature (35 °C) in voltage clamp (holding at -80 mV). Previously, intensity-response relations for ipRGCs have been measured so that the baseline recovers to that in the dark-adapted state (Berson et al., 2002; Dacey et al., 2005; Do et al., 2009). In this experiment, we used a fixed interstimulus interval of 70 s, which is shorter than the time constant of the decay of the persistent response (Emanuel and Do, 2015), and we measured the intensity-response relation to two different wavelengths of light: 440-nm light, which produces a large persistent response, and 560-nm light, which produces a smaller persistent response (Figure 3.1A; Emanuel and Do, 2015). We expect ~65% of melanopsin pigment photoequilibrated with 440-nm light to be in the meta state and ~15% of the pigment photoequilibrated with 560-nm light to be in the meta state (Emanuel and Do, 2015). The order of presentation of the intensity-response relations was from dimmest to brightest and the intensity-response relation to 560-nm light was measured first, so that the large persistent response generated by 440-nm light would not impede measurements to 560-nm light. To minimize any effect of the brightest 560-nm flashes on the responses to the subsequent 440-nm

flashes, the cell was allowed to partially dark adapt for 210 s between the two intensity-response measurements. A longer period was impractical because perforated-patch recordings at high temperature are stable for a relatively short period of time.

We found that the activation of ipRGCs diverged with these wavelengths. First, at dim intensities the holding current between flashes did not differ. At brighter intensities, the holding current after 440-nm flashes was larger than that after 560-nm flashes (example in Figure 3.1B), consistent with the prediction that 440-nm flashes would produce a larger persistent response (Emanuel and Do, 2015). Second, the sensitivity to dim flashes was 7.9 ± 0.5-fold (mean ± sem) higher for 440-nm light than for 560-nm light. This is relatively close to the difference in the absorbance of the two wavelengths by the ground state of melanopsin (19.7-fold). The difference likely arises from incomplete dark adaptation between the two intensity-response relation measurements and from the actual shape of the absorbance spectrum in our conditions (see Appendix 2). Third, the kinetics of the transient flash response did not differ between wavelengths (Figure 3.1C) when matched by peak amplitude, even with large-amplitude responses to flashes that evoke different magnitudes of the ensuing persistent response (Figure 3.1D). Thus, the transient activation is quite similar between wavelengths despite the difference in the magnitude of the persistent response. Fourth, the 440-nm intensity-response relation saturates with a lower response amplitude than the 560-nm relation (Figure 3.1E). Although the low absorbance of melanopsin at 560 nm prevented us from saturating the response, the responses to the brightest 560-nm light were larger than the saturated responses to 440-nm light (Figure 3.1E). Together, these observations suggest that the persistent response narrows the dynamic range over which ipRGCs activate, but does not affect the kinetics of the transient activation.

Figure 3.1. Activation of IpRGCs Differs with Short- and Long-Wavelength Light

(A) A schematic representing the protocol used to measure intensity-response relations. IpRGCs were stimulated with increasing intensities of 440-nm (blue) and 560-nm (red) flashes with an interstimulus interval of 70 s.

(B) An excerpt of the protocol with the current responses to flashes of 440-nm and 560-nm light overlaid. The area of the plot with the dashed box is expanded on the right to illustrate the larger increase in the persistent response with bright 440-nm stimulation compared to that with 560-nm stimulation.

(C) Baseline-subtracted transient responses of the same cell to 50-ms flashes of 560-nm (left; red traces) and 440-nm (right; blue traces) at time 0.

(D) Large responses evoked with 50-ms flashes of 560-nm (red; 1.1×10^8 photons μm^{-2}) and 440-nm (blue; 5.4×10^7 photons μm^{-2}) light. The responses have similar peak amplitudes and time courses. The flash occurs at time 0.

(E) Peak-amplitude intensity response relations of three different ipRGCs to flashes of 560-nm and 440-nm light. The graph on the left is the intensity-response relation of the cell depicted in (B)-(D).

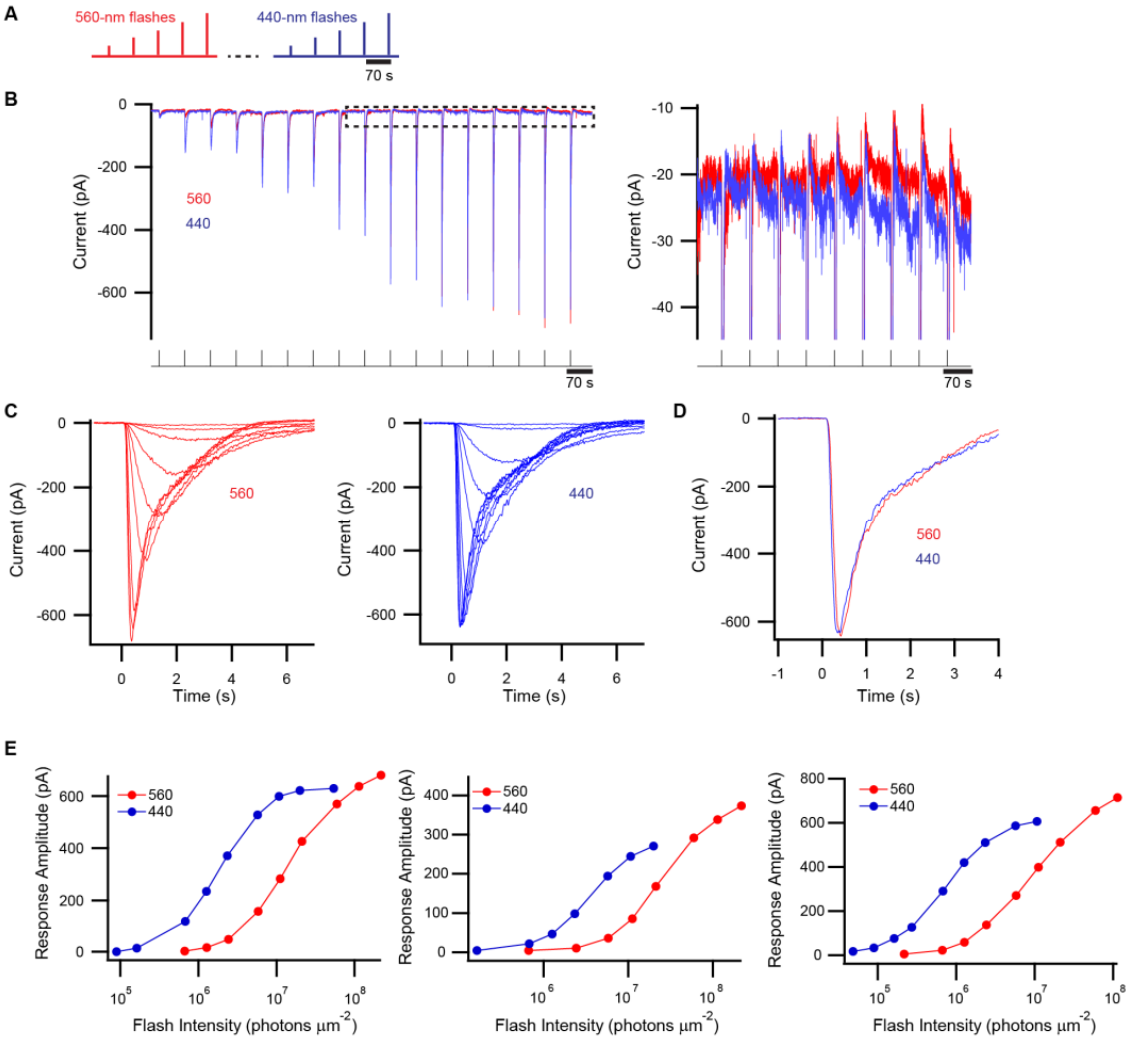

Figure 3.1 (Continued).

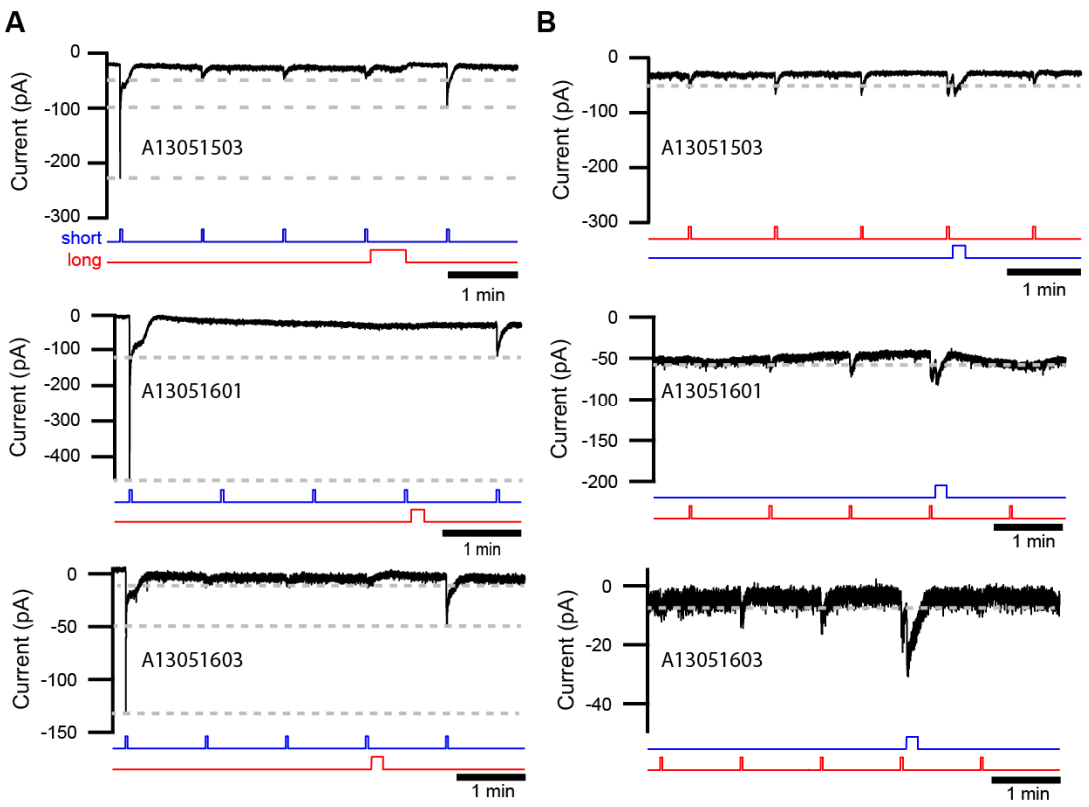

Figure 3.2. IpRGC Light Response Modulation by Short- and Long-Wavelength Light

(A) The responses of three cells (rows) to bright, equally-spaced 2-s steps of short-wavelength light (440-nm; 1.7×10^9 photons μm^{-2} s^{-1}) decreased after the first step. A long-wavelength step (10 or 30 s; 577-nm; 4×10^{10} photons μm^{-2} s^{-1}) in between two short-wavelength stimuli results in increased response amplitude to the short-wavelength step that follows. Dashed gray lines indicate the amplitudes of the first response to the short-wavelength step, the adapted short-wavelength response, and the last short-wavelength step that takes place after the long-wavelength step.

(B) Response amplitudes to equally-spaced, 2-s steps of long-wavelength (577-nm; 4×10^{10} photons μm^{-2} s^{-1}) light presented to the cell (after the protocol in A) increase with each subsequent stimulus. An intervening step of short-wavelength step (10 s; 440-nm; 1.7×10^9 photons μm^{-2} s^{-1}) results in a decrease of the response amplitude to the next long-wavelength step. The dashed, gray lines are drawn at the peak of the first response to long-wavelength light.

We further explored the possibility that the persistent response produces adaptation by delivering a sequence of steps that are expected to saturate the intrinsic photoresponse as well as the persistent response of ipRGCs (2 s of short-wavelength light, separated by 70 s of darkness). We performed this experiment at room temperature (23 °C) because the high stability of the persistent response aids our measurements of its effects over time (Emanuel and Do, 2015). These stimuli produced a persistent response and a decrease in the size of the response to subsequent steps (Figure 3.2A). The degree of this decrease was variable; one cell had no detectable response to the subsequent steps and the other two produced small responses (Figure 3.2A). Decreasing the persistent response by interleaving a long-wavelength conditioning step (10 or 30 s of long-wavelength light, replacing a period of darkness) between two activating steps in this sequence resulted in partial resensitization (n = 3 of 3 cells at 23 °C; Figure 3.2A). Following this sequence, we reversed the wavelengths and found that the response amplitude grew with each long-wavelength step and was decreased by the short-wavelength step (same three cells; Figure 3.2B). The observation of a gradual increase in the response amplitude to each long-wavelength stimulus is consistent with the prediction that the long-wavelength exposures used here are not long or intense enough to produce a photoequilibrium of melanopsin states (Emanuel and Do, 2015). This experiment demonstrates that ipRGCs can be desensitized and resensitized by exposure to short- and long-wavelength light, respectively, and provides further support for the hypothesis that the production of melanopsin molecules in the stably active meta state alters the sensitivity of the cell.

We broadened our sample by applying another stimulation protocol that allows for quantification of the relationship between the persistent response and adaptation. We measured the responses to dim flashes and saturating (or near-saturating) flashes evoked after two illumination sequences: a short-wavelength activation step that was followed by either darkness (the unconditioned protocol) or a long-wavelength conditioning step (the conditioned protocol; Figure 3.3A). Dim flashes are highly informative because they drive the cell in the linear range of the intensity-response relation, thereby producing responses that reflect the waveform of the single-photon response and provide an absolute measure of the sensitivity of the cell (Baylor and Hodgkin, 1973; Do et al., 2009). Saturating flashes are also informative because they elicit the maximum available response, which is a function of pigment

availability and phototransduction gain. The order of presentation of these sequences was randomized; 5 of 9 cells were presented with the unconditioned protocol first. Dim-flash responses must be averaged to give an accurate measure of sensitivity because they are evoked with only a few photon absorptions and the number of absorptions varies across trials. In addition, ipRGC responses to dim flashes are long; at room temperature, they have an integration time of ~20 s (Do et al., 2009). Therefore, we probed sensitivity with 5 dim flashes spaced 70 s apart, beginning 140 s after the activation step (40 s after the end of the conditioning step, if present).

The activation step (0.2 to 2 s of 440-nm light at an intensity of 1.7×10^9 photons μm^{-2} s^{-1}), was designed to establish a photoequilibrium with a maximal fraction of the meta state (65% of the total pigment) and thereby saturate the persistent response (Emanuel and Do, 2015). The persistent response lasted throughout the measurement period (Figure 3.3B). These experiments were conducted over long timescales, which can make it hard to distinguish magnitude of the persistent response (which tends to be on the order of a few pA) from drift over the course of the recording. Drift is the development of a nonselective conductance that changes the mean current with little effect on the noise. On the other hand, activation and deactivation of the persistent response is associated with a large decrease and increase in noise (Emanuel and Do, 2015). Accordingly, we measured the noise rather than current to provide a robust view of the persistent response (Figure 3.3B). We found that the persistent-response activating step also drove desensitization of ipRGCs (Figure 3.3C-D) and the degree of this desensitization varied among cells, as expected from prior work (Do and Yau, 2013). The long-wavelength conditioning step decreased the persistent response (Figure 3.3B) and resensitized a subset of cells (Figure 3.3C-D). The extent of resensitization depended on the degree of desensitization in that the cells that were most desensitized were also resensitized the most (Figure 3.3D). This experiment demonstrates that conditioning light can recover dim-flash sensitivity and the maximum response, but only in roughly half of the ipRGCs sampled.

Figure 3.3. Sensitivity is Affected by the Persistent Response.

(A) Protocol used for quantification of sensitivity and manipulation of the persistent response. The dim-flash sensitivity was measured in the dark with an interstimulus interval of 70 s. In the unconditioned protocol, a step of 440-nm light (0.2-2 s; 2×10^9 photons μm^{-2} s^{-1}) was used to evoke a persistent response. The sensitivity was measured by averaging the last four dim-flash responses and the near-saturating response was measured with stimulation with a step of 440-nm light (0.2-2s; 2×10^9 photons μm^{-2} s^{-1}). The conditioned protocol is the same as the unconditioned except a 30-s step of long-wavelength light (560 nm; 2×10^9 photons μm^{-2} s^{-1}) replaces a period of darkness.

(B) Measurements of the persistent response in 5-s windows in the middle of the sensitivity measurement (left) and just before the saturating flash (right). Unlike the amplitude of the holding current, the standard deviation of the current exhibits little drift over the long time scales of this experiment but is proportional to the magnitude of the persistent response. Connected markers represent individual cells (n = 9). The filled marker represents the cell displayed in C. Kruskal-Wallis p values are depicted and the asterisks signify significant differences determined by pairwise comparisons with a post-hoc sign-rank test. Example dim-flash (left) and saturating (right) responses from measurements of one cell made during the unconditioned (blue) and conditioned (red) portions of the protocol. The responses are baseline-subtracted. The dashed lines indicate the baseline and amplitudes of the responses.

(C) Example dim-flash (left) and saturating (right) responses from measurements of one cell made during the unconditioned (blue) and conditioned (red) portions of the protocol. The responses are baseline-subtracted. The dashed lines indicate the baseline and the amplitudes of the responses.

Figure 3.3 (Continued).

(D) Sensitivity (left) and saturating amplitude (right) measured for the sample (n = 9 cells). Connected markers represent individual cells. The filled marker represents the cell displayed in (C). Labeled p values are from the Kruskal-Wallis ANOVA and asterisks indicate significant differences observed in pairwise comparisons with a post-hoc sign-rank test.

(E) Scatter plot showing the extent of resensitization of the dim-flash response on the ordinate and the magnitude of persistent response recovery on the abscissa. Cells, represented as points, above the dashed line were resensitized after exposure to the conditioning step and those below the line were desensitized.

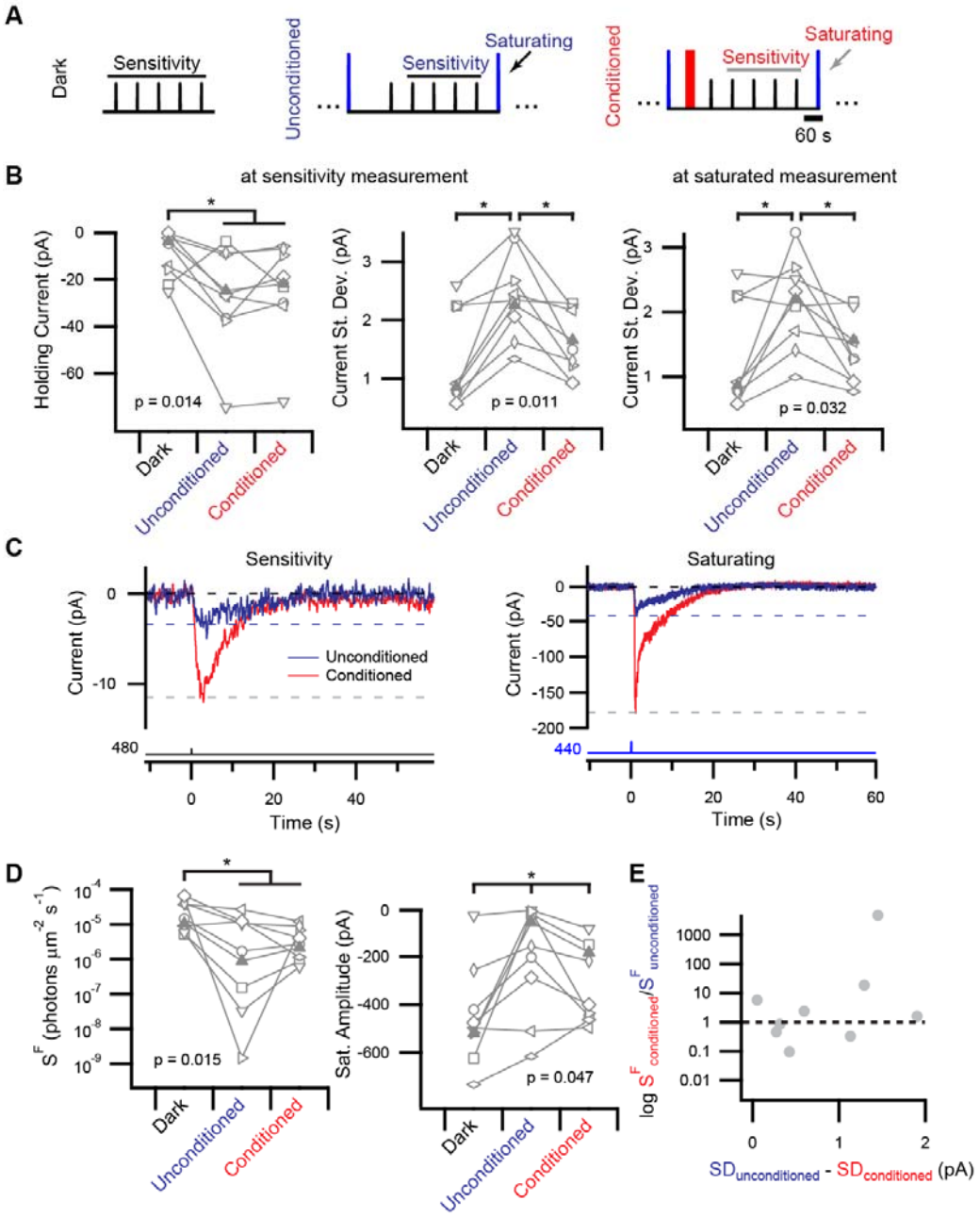

Figure 3.3 (Continued).

The degree to which the sensitivity of the cell changes due to the light exposures of the protocol varied from one cell to another; the sensitivity of some cells was much lower in the unconditioned protocol than the conditioned protocol, but the sensitivity of other cells was higher in the unconditioned protocol than the conditioned protocol. The extent of persistent response modulation also varied from cell to cell, although it was consistently larger in the unconditioned protocol than in the conditioned protocol. The variation in the magnitude of the persistent response modulation does not correlate with the variation in dim-flash sensitivity (Figure 3.3E), which suggests that adaptation driven by the steps of light may be the principal determinant of the sensitivity change. This variability suggests that the adaptation produced by the conditioning step can interfere with measurement of adaptation due to the meta state and the persistent response.

The previous experiment was performed at room temperature (23 °C), and we sought to determine whether a similar phenomenon can be observed near physiological temperature (35 °C). The sensitivity and the kinetics of the ipRGC light response change with temperature, with dim-flash responses accelerating by about three-fold (Do et al., 2009) and persistent responses decaying faster (Emanuel and Do, 2015). Accordingly, we accounted for the faster kinetics of the dim-flash response by using a briefer protocol in which dim flashes were separated by 35 s (the minimum period for the responses to decay completely between flashes) rather than the 70 s used previously (Figure 3.4A). Despite this shorter interval, the persistent response decayed completely during the measurement period for dim-flash responses; the holding current and standard deviation measured in the conditioned and unconditioned portions of the protocol were not significantly different from darkness or from each other (Figure 3.4B).

Consistent with a lack of persistent response at the time of measurement, the dim-flash sensitivity in the unconditioned protocol did not differ from that at baseline (Figure 3.4C-D). All cells did have a lower dim-flash sensitivity in the conditioned protocol (Figure 3.4D), revealing that adaptation driven by the conditioning light can outlast the persistent response.

There was no difference in the magnitude of the saturated response between the conditioned and unconditioned protocols. This may be due to the later time point at which the saturated response is

measured, which gives additional opportunity for resensitization following the conditioning pulse. Alternatively, the magnitudes of the dim-flash and saturated responses reflect different aspects of ipRGC phototransduction that are differentially affected by adaptation driven by the persistent response or the conditioning light.

Taken together, these observations suggest that the extent to which the deactivation of the persistent response causes a sensitization of ipRGCs depends on the balance of two factors: the amount of adaptation produced by the conditioning light that deactivates the persistent response, and the amount of adaptation that is driven by the persistent response itself. The balance between "conditioning-driven" and "persistence-driven" adaptation appears to vary across ipRGCs, giving rise to variation in the extent of resensitization by conditioning light observed in Figure 3.3.

Figure 3.4 Persistent Response is Relatively Short-Lived at Physiological Temperature

(A) Protocol used to measure sensitivity and manipulate the persistent response at physiological temperature. The dim-flash sensitivity was measured in the dark with an interstimulus interval of 35 s. In the unconditioned protocol, a step of 440-nm light (2 s; 2×10^9 photons μm^{-2} s^{-1}) was used to evoke a persistent response. The sensitivity was measured by averaging the last four dim-flash responses and the near-saturating response was measured with stimulation with a step of 440-nm light (2 s; 2×10^9 photons μm^{-2} s^{-1}). The conditioned protocol is the same as the unconditioned except a 30-s step of 560-nm light (2×10^9 photons μm^{-2} s^{-1}) replaces a period of darkness.

(B) Measurements of the persistent response at the time of sensitivity measurement (left) and just before the saturating flash (right). The standard deviation of the current is used for this measurement because it is not subject to drift like the amplitude of the current is over the long time scales of this experiment. Connected markers represent individual cells (n = 7). The filled marker represents the cell displayed in (C). No significant differences were observed using the Kruskal-Wallis test.

(C) Example dim-flash (left) and saturating (right) responses from measurements of one cell made during the unconditioned (blue) and conditioned (red) portions of the protocol. The responses are baseline-subtracted. The dashed lines indicate the baseline and the amplitudes of the responses.

(D) Sensitivity (left) and saturating amplitude (right) measured for the sample (n = 7 cells). Connected markers represent individual cells. The filled marker represents the cell displayed in (C). Labeled p values are from Kruskal-Wallis test. Asterisks indicate significant differences observed in pairwise comparisons with a post-hoc sign-rank test.

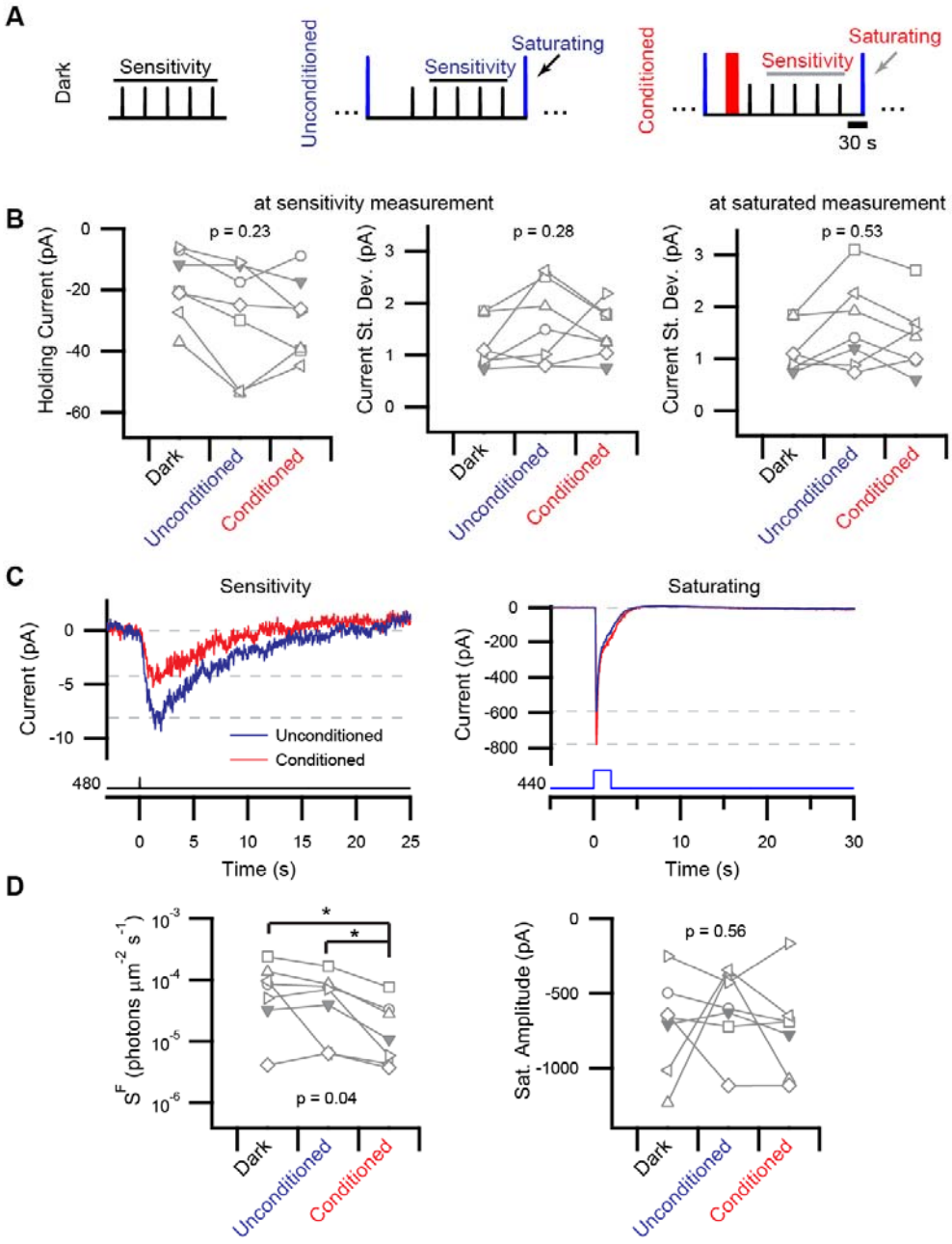

Figure 3.4 (Continued).

To survey this balance in a large sample of cells, we developed a simplified and shortened protocol that we applied to ipRGCs at room temperature (Figure 3.5A-C). Each cell was dark adapted, had its dim-flash sensitivity measured, and then was exposed to a near-saturating flash of white light (200 ms; produced by a xenon arc lamp), that is predicted to produce (and did produce) a persistent response that is stable over time (Figure 3.5D-E). This was followed by two probe flashes of 560-nm light (Figure 3.5C; 1×10^8 photons μm^{-2}; an intensity on the steep portion of the intensity-response relation for most cells when dark adapted), between which a 70-s conditioning step of 560-nm light was included (2×10^9 photons μm^{-2} s^{-1}). The persistent response measured after the conditioning step was smaller in most cells (Figure 3.5D). The persistent response has a long lifetime at room temperature (>20 min; Emanuel and Do, 2015), suggesting that its smaller magnitude at the time of the probe flash is due to the conditioning step and not to elapsed time.

We observed that 17 of 70 cells had an increased response to the second 560-nm flash than the first, suggesting that exposure to the conditioning light increased sensitivity (Figure 3.5E). The holding current was overtly reduced after the conditioning light in 14 of these 17 cells (top right quadrant of Figure 3.5F). A similar proportion (44/53) of cells that had a smaller response to the second flash than the first had smaller holding currents after the conditioning step (top left quadrant of Figure 3.5F). The similarity of these proportions and the lack of correlation suggest that we cannot predict whether a cell will be sensitized based on changes in the size of the persistent response. In addition, the conditioning step in this experiment resulted in desensitization more often than resensitization. Conditioning-driven adaptation appears to be greater than persistence-driven adaptation in the majority of ipRGCs.

Figure 3.5. Cell-to-Cell Variability in Light- and Persistent Response-Induced Adaptation

(A) Schematic of the protocol used to assay variability in ipRGC adaptation driven by light exposure and the persistent response. The cells (n = 70) were exposed to a 200-ms, saturating flash of white light (xenon; 2.0×10^{-2} μW μm^{-2}, equivalent to 3.8×10^{6} lux) to induce a persistent response. Two 560-nm flashes (1×10^{8} photons μm^{-2}) were used to probe the sensitivity of the cell and a 560-nm conditioning step (2×10^{9} photons μm^{-2} s^{-1}) was applied to decrease the persistent response. To evaluate the size of the persistent response, the holding current and standard deviation was measured in 5-s windows designated by each arrow.

(B) Exemplar cell probed with this protocol. The dashed lines represent the baseline current and the current at the time of measurement of Pers. Response 1. The amplitude of the response to xenon light is greater than 100 pA. The response is cut off for visualization of the persistent response and responses to 560-nm flashes.

(C) Overlaid baseline-subtracted response to the two 560-nm flashes (50-ms starting at time 0). The dashed lines indicate the baseline and amplitudes of the two flash responses.

(D) Scatter plots showing the baseline-subtracted persistent current and how it changes over the course of the protocol. The scatter plot on the left compares the second measurement of the persistent response to the first. There is little decay over this period of 70 s. The scatter plot on the right compares the third measurement of the persistent response to the second. Points below the line have decreased persistent response amplitudes.

(E) Same as (D), but illustrating the absolute standard deviation of the current at the measurement times of the persistent current. Points below the line have decreased noise over time.

Figure 3.5 (Continued).

(F) Scatter plot (left) and histogram (right) showing the response amplitudes to the 560-nm flashes. The majority of cells were desensitized at the time of the second 560-nm flash as represented by the response amplitudes lying below the dotted line on the scatter plot.

(G) Scatter plot illustrating the extent of recovery of the persistent response (ordinate) and extent of change in 560-nm flash response amplitude (abscissa). Points above the horizontal line had a decreased persistent response and points to the right of the vertical line had an increased sensitivity after the conditioning step.

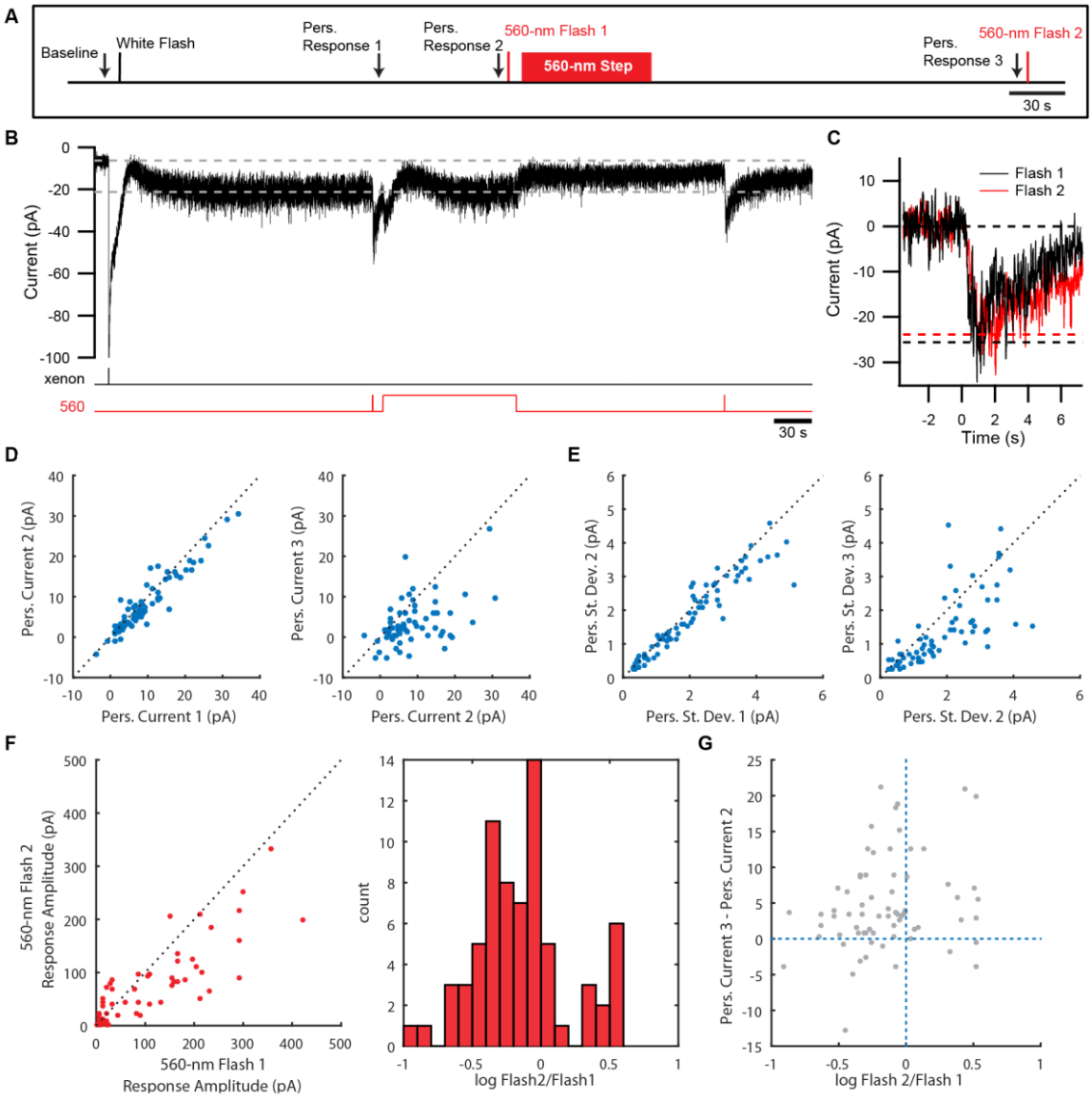

Figure 3.5 (Continued).

Discussion

In this study, we examined ipRGC properties that are affected by the tristable nature of melanopsin (Emanuel and Do, 2015; Matsuyama et al., 2012). We specifically tested the hypothesis that formation of stably active melanopsin molecules in the meta state would affect the activation and adaptation of the intrinsic light response of ipRGCs. The activation of ipRGCs by short-wavelength light, which shifts a large proportion of melanopsin into the active state, appears to have a narrower dynamic range and drive smaller saturated responses than activation of ipRGCs by long-wavelength light, which shifts a much smaller proportion of melanopsin into the active state. We also observed that the generation of stably active melanopsin and the associated persistent response can result in a decrease in ipRGC sensitivity that can be subsequently recovered with long-wavelength, conditioning light. However, this phenomenon was not observed consistently in all ipRGCs because the long-wavelength conditioning light also drove desensitization of the cell.

The only way to acutely manipulate the fractions of melanopsin in each state is to expose the cell to light. This exposure, itself, produces adaptation in addition to adaptation driven by the persistent response. Although such light-driven adaptation of the ipRGC light response has been well documented (Do and Yau, 2013; Wong et al., 2005), the underlying molecular mechanism remains a mystery. There are likely multiple mechanisms involved, as the adaptation of the intrinsic light response is reduced but not abolished in a calcium-free external solution, indicating that there are both calcium-dependent and calcium-independent adaptation mechanisms (Do and Yau, 2013). Adaptation also likely takes place at the level of individual melanopsin molecules via their phosphorylation and their binding to arrestin (Blasic et al., 2014; Cameron and Robinson, 2014; Fahrenkrug et al., 2014). Without a means to manipulate light-driven adaptation selectively, the consequences of meta state stability and the persistent response on ipRGC signaling are difficult to distinguish from the consequences of adaptation to acute light exposures.

We previously observed that the duration of the persistent response is temperature dependent; it decays with a time constant of ~140 s at physiological temperature but decays very little over tens of minutes at room temperature (Emanuel and Do, 2015). This observation has been corroborated here.

The protocol we developed to measure the effect of the persistent response on sensitivity requires a long period of time because the intrinsic light response of ipRGCs is very slow (Berson et al., 2002; Do et al., 2009) and averaging of dim-flash responses is necessary due to Poisson fluctuations in photon absorption. At room temperature, the persistent response is observed at the time of sensitivity measurement but, at high temperature, it was not, even though the protocol was condensed to accommodate the faster kinetics of the dim-flash light response. This observation directly demonstrates that the temperature dependence of the persistent response, which may reflect the rate of decay of melanopsin from the active state, is much greater than the temperature dependence of acute ipRGC photoactivation. Furthermore, the conditioning light consistently reduced the sensitivity at high temperature whereas it was capable of increasing the sensitivity at room temperature. This suggests that the temperature dependence for light-driven adaptation is different from that for the lifetime of the persistent response. In this study, the consequence of this discrepancy in temperature dependence is that there is a limited time period in which long-wavelength light exposure could potentiate ipRGC sensitivity at physiological temperature.

We observe a large degree of variability among cells in our experiments that examined the resensitization of the cell with long-wavelength light. A subset of cells are dominated by adaptation driven by conditioning light (e.g., cells that have lower sensitivity after long-wavelength light) and others are dominated by adaptation driven by the meta state and its associated persistent response (e.g., cells that have higher sensitivity after long-wavelength light). We also observed that the proportion of cells sensitized after long-wavelength light depends on the particular experimental protocol (compare Figure 3.2, Figure 3.3, and Figure 3.5). This variability provides a possible explanation for the discrepancies in previous studies that examined similar consequences of stably-active melanopsin with different approaches (Mawad and Van Gelder, 2008; Mure et al., 2007).

Another possible explanation for the discrepancy is that different ipRGC populations might have been sampled. There are at least five types of morphologically-defined ipRGCs and the behaviors and brain areas that exhibited potentiation by long-wavelength light are downstream of the so-called M1 ipRGC population, which are the most sensitive melanopsin-expressing cells and, thus, likely have the

largest persistent responses (Güler et al., 2008; Mure et al., 2007; Schmidt and Kofuji, 2009). By contrast, the direct examination of ipRGCs used a multielectrode array. When targeting ipRGCs directly with loose-patch electrodes for experiments not described in this chapter, we have observed that the current density for M1 ipRGCs is much lower than that for non-M1 ipRGCs, consistent with the differences in the published spiking capabilities of M1 and non-M1 ipRGCs (Schmidt and Kofuji, 2009; Zhao et al., 2014). Therefore, a multielectrode array is more likely to sample from non-M1 ipRGCs, which are less sensitive and likely have smaller persistent responses than M1 ipRGCs. We expect that the largest persistent responses are likely to drive the most adaptation and, thus, cells that produce large persistent responses could be resensitized the most. Therefore, sampling of different ipRGC populations could account for the difference in long-wavelength potentiation between these studies. An experiment that could be done to determine whether sampling is an issue is to record the spike outputs of M1 ipRGCs to the same stimuli used in both studies. Based on the experiments described in this chapter, we hypothesize that the long-wavelength potentiation observed in the brain areas and behaviors regulated by ipRGCs (Mure et al., 2007) can be recapitulated in the spike output of at least some M1 ipRGCs.

In summary, these experiments demonstrate that the stability of the meta state of melanopsin has consequences for the activation of ipRGCs. However, a full understanding of how melanopsin tristability interacts with the activation and adaptation of ipRGCs has not yet been established. The experiments described here provide a number of key insights that provide a basis for designing experiments that more thoroughly address this question. Primarily, it is necessary to distinguish further between conditioning-driven adaptation and persistence-driven adaptation. This might be accomplished by using longer steps of conditioning light of lower intensities, because lower intensities may produce less adaptation while still generating a large photoequilibrium fraction of the meta state. Furthermore, because the fraction of melanopsin in the meta state and the associated persistent response are wavelength dependent, it may be possible to control for the adaptation produced by the conditioning light by comparing the sensitivity atop persistent responses generated by two different wavelengths that are calibrated to activate the cell equivalently when it is dark adapted. Another useful future experiment could be to measure the extent of adaptation driven during ongoing light and compare it to adaptation

driven by the persistent response. The results of such a comparison could lead to insights about the mechanisms underlying adaptation. For example, if the persistent response current and ongoing light response current are matched but the sensitivity of the cell is not, the conclusion could be made that current is not sufficient for adaptation.

Experimental Procedures

Tissue

All studies were performed on retinas isolated from BAC-transgenic mice that express tdTomato in ipRGCs (Do et al., 2009). Mice were postnatal days 21-100, either male or female, and were housed in a 12-hr light/12-hr dark cycle. Mice were dark adapted for at least 1.5 hours prior to anesthetization with Avertin and all experiments took place between zeitgeber times 3 and 10; time 0 is defined as lights on. After anesthetization, the mice were enucleated and euthanized. The retina was flat-mounted onto a poly-l-lysine-coated coverslip and placed into a recording chamber. The Institutional Animal Care and Use Committee of Boston Children's Hospital approved all animal procedures.

Solutions

The retinas were bathed in a solution of ionic Ames composed of (in mM) 120 NaCl, 22.6 $NaHCO_3$, 3.1 KCl, 0.5 KH_2PO_4, 6 glucose, 1.2 $CaCl_2$, and 1.2 $MgSO_4$ that was equilibrated with carbogen (95% O_2/5% CO_2). Perforated-patch clamp recordings were performed using an internal solution composed of (in mM) 110 K-Methanesulfonate, 13 NaCl, 2 $MgCl_2$, 10 EGTA, 1 $CaCl_2$, 10 HEPES, and 0.125-0.25 amphotericin B. The pH was adjusted to 7.2 with KOH and the final $[K^+]$ was 139 mM.

Electrophysiology

Cells were visualized using infrared transillumination (850-nm center wavelength and 30-nm width at half maximum). IpRGCs were identified by exposure to <1 s of tdTomato excitation light (25-nm bandpass centered on 545 nm, 6×10^9 photons μm^{-2} s^{-1}). The overlying inner limiting membrane was removed with an empty patch pipette. Recording pipettes (3-7 MΩ) were wrapped with parafilm to reduce their capacitance and the series resistance was monitored, but not compensated. Recordings were performed at room temperature (23 °C) as well as near-physiological temperature (35 °C). The temperature was controlled using an in-line heater and was monitored with a thermistor in the bath.

Voltage-clamp recordings were low-pass filtered at 4 kHz and sampled at 10 kHz. For analysis, the traces were digitally low-pass filtered at 10 Hz. Analysis was performed using Igor Pro and Matlab. We targeted M1 ipRGCs by recording from cells with bright tdTomato fluorescence and we expect the majority of the cells were M1 ipRGCs because of their high sensitivity and relatively large saturating amplitudes. However, cells were not excluded from the dataset if they did not have these characteristics.

Optical Stimulation

In most cases, optical stimuli originated from a pair of light sources: a 75-W xenon arc lamp and a 100-W mercury halide lamp. Light from these sources was filtered to deplete heat and select intensity and wavelength. Light was delivered to the cell through a 40× objective, producing a uniform, circular field with a 350-μm diameter that was centered on the soma. The timing of the stimulus was controlled with electromechanical shutters (Uniblitz). Light was assumed to be the center wavelength of 10-nm bandpass filters and its intensity was calibrated using a radiometer. For white light generated by the xenon lamp, photon flux was calculated from spectra measured with a calibrated spectrometer. "Flashes" are impulse stimuli (i.e., duration and intensity can be interchanged to give the same response), and non-impulse stimuli are referred to as "steps."

References

Berson, D.M., Dunn, F.A., and Takao, M. (2002). Phototransduction by retinal ganglion cells that set the circadian clock. Science 295, 1070-1073.

Baylor, D.A., and Hodgkin, A.L. (1973). Detection and resolution of visual stimuli by turtle photoreceptors. J. Physiol. 234, 163-198.

Blasic, J.R., Jr., Matos-Cruz, V., Ujla, D., Cameron, E.G., Hattar, S., Halpern, M.E., and Robinson, P.R. (2014). Identification of critical phosphorylation sites on the carboxy tail of melanopsin. Biochemistry 53, 2644-2649.

Cameron, E.G., and Robinson, P.R. (2014). β-Arrestin-dependent deactivation of mouse melanopsin. PloS ONE 9, e113138.

Dacey, D.M., Liao, H.W., Peterson, B.B., Robinson, F.R., Smith, V.C., Pokorny, J., Yau, K.-W., and Gamlin, P.D. (2005). Melanopsin-expressing ganglion cells in primate retina signal colour and irradiance and project to the LGN. Nature 433, 749-754.

Do, M.T.H., and Yau, K.-W. (2010). Intrinsically photosensitive retinal ganglion cells. Physiol. Rev. 90, 1547-1581.

Do, M.T.H., and Yau, K.-W. (2013). Adaptation to steady light by intrinsically photosensitive retinal ganglion cells. Proc. Natl. Acad. Sci. USA 110, 7470-7475.

Do, M.T.H., Kang, S.H., Xue, T., Zhong, H., Liao, H.W., Bergles, D.E., and Yau, K.-W. (2009). Photon capture and signalling by melanopsin retinal ganglion cells. Nature 457, 281-287.

Emanuel, A.J., and Do, M.T.H. (2015). Melanopsin tristability for sustained and broadband phototransduction. Neuron 85, 1043-1055.

Fahrenkrug, J., Falktoft, B., Georg, B., Hannibal, J., Kristiansen, S.B., and Klausen, T.K. (2014). Phosphorylation of rat melanopsin at Ser-381 and Ser-398 by light/dark and its importance for intrinsically photosensitive ganglion cells (ipRGCs) cellular Ca^{2+} signaling. J. Biol. Chem. 289, 35482-93.

Güler, A.D., Ecker, J.L., Lall, G.S., Haq, S., Altimus, C.M., Liao, H.W., Barnard, A.R., Cahill, H., Badea, T.C., Zhao, H.*, et al.* (2008). Melanopsin cells are the principal conduits for rod-cone input to non-image-forming vision. Nature 453, 102-105.

Lucas, R.J., Hattar, S., Takao, M., Berson, D.M., Foster, R.G., and Yau, K.-W. (2003). Diminished pupillary light reflex at high irradiances in melanopsin-knockout mice. Science 299, 245-247.

Lucas, R.J., Peirson, S.N., Berson, D.M., Brown, T.M., Cooper, H.M., Czeisler, C.A., Figueiro, M.G., Gamlin, P.D., Lockley, S.W., O'Hagan, J.B.*, et al.* (2014). Measuring and using light in the melanopsin age. Trends Neurosci. 37, 1-9.

Matsuyama, T., Yamashita, T., Imamoto, Y., and Shichida, Y. (2012). Photochemical properties of mammalian melanopsin. Biochemistry 51, 5454-5462.

Mawad, K., and Van Gelder, R.N. (2008). Absence of long-wavelength photic potentiation of murine intrinsically photosensitive retinal ganglion cell firing *in vitro*. J. Biol. Rhythms 23, 387-391.

Mure, L.S., Cornut, P.L., Rieux, C., Drouyer, E., Denis, P., Gronfier, C., and Cooper, H.M. (2009). Melanopsin bistability: a fly's eye technology in the human retina. PloS ONE 4, e5991.

Mure, L.S., Rieux, C., Hattar, S., and Cooper, H.M. (2007). Melanopsin-dependent nonvisual responses: evidence for photopigment bistability *in vivo*. J. Biol. Rhythms 22, 411-424.

Panda, S., Sato, T.K., Castrucci, A.M., Rollag, M.D., DeGrip, W.J., Hogenesch, J.B., Provencio, I., and Kay, S.A. (2002). Melanopsin (*Opn4*) requirement for normal light-induced circadian phase shifting. Science 298, 2213-2216.

Schmidt, T.M., and Kofuji, P. (2009). Functional and morphological differences among intrinsically photosensitive retinal ganglion cells. J. Neurosci. 29, 476-482.

Wong, K.Y., Dunn, F.A., and Berson, D.M. (2005). Photoreceptor adaptation in intrinsically photosensitive retinal ganglion cells. Neuron 48, 1001-1010.

Zhao, X., Stafford, B.K., Godin, A.L., King, W.M., and Wong, K.Y. (2014). Photoresponse diversity among the five types of intrinsically photosensitive retinal ganglion cells. J. Physiol. 592, 1619-1636.

Chapter 4: Diverse Physiology of Intrinsically Photosensitive Retinal Ganglion Cells Within and Between Subtypes

Alan Joseph Emanuel and Michael Tri Hoang Do

This chapter describes experiments performed to examine the diversity of the biophysical parameters underpinning ipRGC signal generation. The work was conceptualized and initiated by Alan Emanuel and Michael Do. The stereotaxic injections, electrophysiological measurements, and some histological procedures were performed by Alan Emanuel. We would like to acknowledge Ryan Adams and Verda Bursal for their assistance with additional histological procedures, including tissue sectioning, immunostaining, and imaging.

Summary

Intrinsically photosensitive retinal ganglion cells (ipRGCs) are a class of photoreceptors responsible for the regulation of many different visual behaviors. These cells are diverse in that there are multiple subtypes with distinct morphologies and these subtypes have previously been reported to have different physiological properties. In this study, we examined physiological diversity at the level of biophysical mechanisms governing the light responses of ipRGCs using a systematic, electrophysiological approach. We found a high degree of variability in the spike output as well as basic biophysical properties of ipRGCs. Previous work has suggested that distinct functions, the entrainment of the circadian clock and the pupillary light reflex, are regulated by two subgroups of ipRGCs. However, the physiological properties of those ipRGCs have not previously been examined. To determine whether the diversity we observe can be accounted for by the functions ipRGCs regulated, we recorded from ipRGCs that were retrogradely labeled from the hypothalamus or pretectum. The distributions of hypothalamus-projecting and pretectum-projecting ipRGCs were highly overlapping. By comparing these cells to the general population of ipRGCs (sampled without knowledge of their brain projections), we found that the diversity represented in the hypothalamus- and pretectum-projecting ipRGCs highly overlaps with that found in the entire M1 and M2 ipRGC population. This suggests that each brain region receives the full array of information encoded by ipRGCs. By filling a subset of ipRGCs, we were able to classify M1 and M2 ipRGCs in our sample based on their physiological parameters. Surprisingly, we found that the diversity in physiological parameters within the M1 subtype rivaled the diversity between the M1 and M2 subtypes. Furthermore, many of the individual parameters did not correlate with each other, especially within the M1 ipRGC subtype. This lack of correlation suggests that ipRGCs are particularly flexible in setting their responses to light. Overall, this study demonstrates a previously unappreciated degree of physiological diversity within a molecularly- and morphologically-defined cell type, which may be useful for encoding irradiance in an efficient manner for regulation of many visual functions.

Introduction

A subset of retinal ganglion cells is intrinsically photosensitive due to the expression of melanopsin. These cells send axons to various brain regions to regulate many visual functions. One of

these functions is the entrainment of the circadian clock to ensure that physiological and behavioral events occur at the appropriate time of day. IpRGCs are also responsible for constriction of the pupil in response to light, the so-called pupillary light reflex. A striking aspect of the functions driven by ipRGCs is that they use light in very different manners. The clock and pupil provide an excellent example of such a difference; the circadian clock integrates light over long periods of time (Nelson and Takahashi, 1991), whereas the pupillary light reflex responds to the overall irradiance from one moment to the next. How the population of ipRGCs drives such distinct behaviors is unknown.

There are at least five morphologically-defined subtypes of ipRGCs, designated as M1-M5. These subtypes are defined by their melanopsin expression and dendritic arborization (Baver et al., 2008; Berson et al., 2010; Ecker et al., 2010; Schmidt and Kofuji, 2009, 2011). Physiological properties also differ between subtypes (Ecker et al., 2010; Schmidt et al., 2014; Schmidt and Kofuji, 2009, 2011; Tu et al., 2005; Zhao et al., 2014). On a coarse level, it has been established that these subtypes have different axonal projections to the brain. M1 ipRGCs provide dense innervation to the suprachiasmatic nucleus (SCN), shell of the olivary pretectal nucleus (OPN), and intergeniculate leaflet (IGL; Gooley et al., 2003; Hattar et al., 2006), while non-M1 ipRGCs provide dense innervation to the core of the OPN, the ventral lateral geniculate nucleus (vLGN), and somewhat sparser innervation to the dorsal LGN among other regions (Ecker et al., 2010). These differences in projection patterns suggest that ipRGC subtypes regulate diverse functions.

Indeed, lesion of M1 ipRGCs using genetic expression of attenuated diphtheria toxin demonstrates that they are major regulators of both the circadian clock and the pupillary light reflex (Güler et al., 2008). By contrast, the M4 ipRGCs appears to contribute to image-forming vision through a projection to the dorsal lateral geniculate nucleus, the conventional visual thalamic area (Estevez et al., 2012). Melanopsin knockout mice have decreased contrast sensitivity within M4 ipRGCs and at a behavioral level, which suggests that the intrinsic photosensitivity of M4 ipRGCs plays a role in contrast vision (Schmidt et al., 2014). These examples demonstrate that the different morphological subtypes of ipRGCs regulate distinct functions.

M1 ipRGCs alone appear to regulate many diverse functions, including both the pupillary light reflex and the circadian clock (Güler et al., 2008). There is evidence that M1 ipRGCs can also be divided into molecular subtypes that control different functions. A subset of M1 cells, as well as all other subtypes of ipRGCs, express a transcription factor, Brn3b (Chen et al., 2011; Jain et al., 2012). Using a genetic strategy that ablates the lineage of melanopsin-expressing cells that also express Brn3b, Hattar and colleagues showed that an ipRGC projection to the SCN remains intact and that these mice were still able to entrain their circadian clocks to light. However, they had a strongly attenuated pupillary light reflex (Chen et al., 2011). These results suggest that the mouse ipRGCs that regulate the pupil are distinct from those that regulate the circadian clock, but that both functions are regulated by M1 ipRGCs. On the other hand, a retrograde-labeling study performed in rat demonstrates that a substantial proportion of ipRGCs have axon collaterals and that a proportion of ipRGCs that project to the SCN also project to the OPN (Gooley et al., 2003). The contrasting results of these studies have not been reconciled.

Whether signal generation in M1 ipRGCs is tailored to the functions that they regulate remains an open question. Here, we systematically examined the diversity of signal generation in ipRGCs. In addition to finding a high degree of diversity in the general population, we did not detect differences between ipRGCs that project to the hypothalamus and ipRGCs that project to the pretectum. Furthermore, the extent of physiological diversity within cells of the morphological cell type is surprising; the physiological properties of M1 ipRGCs span a similar range as the difference between the M1 and M2 ipRGCs that we sampled.

Results

IpRGCs Produce Diverse Spike Output in Response to Illumination

Previous research has demonstrated a large degree of variability in the spike output of ipRGCs (Mawad and Van Gelder, 2008; Schmidt and Kofuji, 2009; Tu et al., 2005) as well as in physiological properties that govern the output of the cells, such as the sensitivity of the cell and the extent to which it adapts (Do and Yau, 2013; Do et al., 2009; Emanuel and Do, 2015; Xue et al., 2011). In these studies, the variability in spike output was observed near body temperature whereas the biophysical parameters have largely been measured at room temperature. To determine whether the output of ipRGCs remains

diverse at room temperature, which would facilitate analysis of the underlying biophysical mechanisms, we recorded the signals of ipRGCs using the non-invasive, loose-patch method. To identify ipRGCs, we used a transgenic mouse that labels M1, M2, and likely the sparse M3 ipRGCs with expression of the fluorescent protein, tdTomato (Do et al., 2009; Müller et al., 2010). Cells were targeted pseudorandomly by choosing a field of view and recording from the centermost ipRGC. The output due to intrinsic ipRGC phototransduction was measured by including blockers of synaptic transmission in the external solution that have previously been demonstrated to isolate the intrinsic response (see experimental procedures; Do et al., 2009).

Figure 4.1. Diverse Spiking in a Sample of IpRGCs

(A) An example loose-patch recording of the response of an ipRGC to a 60-s step of white light produced by a xenon arc lamp (5.3×10^{-9} μW μm^{-2}, equivalent to 7 lux).

(B) Expanded timescale of one spike from (A).

(C) Raster plot indicating spike times of 23 different ipRGCs in response to a 60-s step of xenon light (5.3×10^{-9} μW μm^{-2}, equivalent to 7 lux). The cells are sorted so that cells with the highest spontaneous rates (measured for 10 s immediately preceding stimulation) are at the top and the cells with the lowest rates are at the bottom. The baseline for cell 23 was only recorded for 10 s prior to stimulation.

(D) Firing rate during the light step as a function of baseline firing rate. Cells either increased their firing in response to the light (above the dashed line) or did not change their firing (on the dashed line).

(E) Raster plot of the same cells in response to higher intensity step of xenon light (3.8×10^{-6} μW μm^{-2}, equivalent to 720 lux). The cells are displayed in the same order as in (C).

(F) Same as D, but for the response prior to and during the higher intensity stimulation. Some cells increased their firing rate (above dashed line) or decreased their firing rate (below dashed line), measured as the average during light stimulation. All experiments performed in the presence of pharmacological blockers of synaptic transmission at 23 °C.

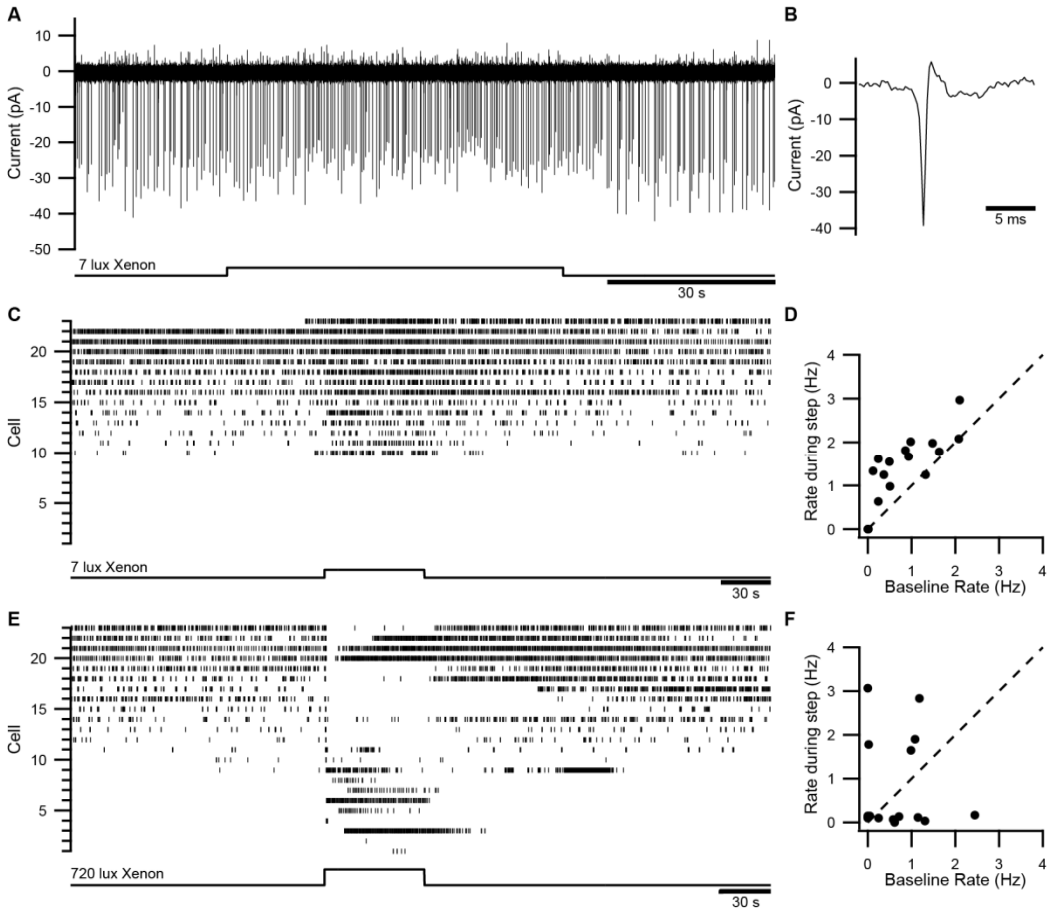

Figure 4.1 (Continued).

After the initial identification with imaging light (see experimental procedures), cells were allowed to dark adapt for at least 20 minutes prior to recording responses to stimulus light. Each cell was exposed to two steps of white light. The first step was at a relatively low intensity (5.3×10^{-9} $\mu W\ \mu m^{-2}$, equivalent to 7 lux), near the threshold step intensity that has been published for the intrinsic response of M1 ipRGCs (Do et al., 2009; Schmidt and Kofuji, 2009; Zhao et al., 2014) and the second light step was 100-fold more intense. An example of a loose patch recording is shown in Figures 4.1A-B. Across the sample (23 cells), there was a high degree of diversity, both in the spontaneous firing and the response to light (Figures 4.1C-F). The lower intensity step increased the firing rate by at least 10% in 12 of 23 cells (Figure 4.1D). These cells are likely M1 ipRGCs due to their high sensitivity; M2 ipRGCs are understood to be at least an order of magnitude less sensitive (Ecker et al., 2010; Schmidt and Kofuji, 2009; Zhao et al., 2014). At the higher intensity, all cells altered their firing by at least 10% (Figure 4.1E-F). However, the polarity of the response was not consistent across cells. 13 of 23 cells increased their firing for most of the step. The remaining cells were silenced following a transient burst of spikes at the step onset (Figure 4.1E-F). Based on previous experiments in which the subthreshold membrane voltage was recorded during light-evoked spike generation (Do and Yau, 2013; Emanuel and Do, 2015; Wong et al., 2005), the decrease in spiking is likely due to activation that overwhelms the spike generator resulting in depolarization block. In addition to the polarity diversity, the extent of the change in firing rate was also quite diverse from cell to cell. Of particular note, the 12 ipRGCs that responded to the dimmer step responded to the brighter step with diverse spike patterns, suggesting that there is a large degree of heterogeneity in the spike output not only between ipRGC subtypes, but also within them.

A Protocol for Systematic Measurement of Signal Generation in IpRGCs

In order to investigate the diversity in the parameters that govern the output of ipRGCs in a systematic way, we developed a standard protocol that elucidates many parameters governing intrinsic membrane properties, synaptic input, and phototransduction (Figure 4.2A). For this purpose, we used perforated-patch electrophysiology (see experimental procedures), which prevents dialysis of the intrinsic light response and tends to be stable for longer periods of time than whole-cell patch clamp. This particular protocol takes ~55 minutes, which is comparable to the lifetime of most recordings.

After exposure to the imaging light used to identify cells (see experimental procedures), the cells were dark adapted for at least 20 minutes before recording responses to light, which allows the physiological properties of each cell to be measured from a similar, dark-adapted state (Emanuel and Do, 2015). After the perforation of the cell stabilized (monitored by tracking access resistance over time), the resting membrane potential was measured in a 10-s period without any injected current in current clamp mode. If the cell was spontaneously active (51 of 90 cells), we measured the average voltage between spikes as the "resting potential" of that cell. The input resistance and spiking properties were measured using 2-s steps of current, each separated by 3 s (example steps and responses shown in Figure 4.2B).

Subsequently, the response of the cell to light was measured. Due to the limited lifetime of the recordings, we confined our measures of the light response to dim and saturated flashes. Dim flashes produce intrinsic responses within the linear range of the intensity-response relation and these responses are highly informative because their waveform reflects the waveform of the single-photon response, which is the basic building block of all light responses (Do et al., 2009). Furthermore, the amplitude of the dim-flash response provides an absolute measure of sensitivity (Do et al., 2009). The saturated response reflects the maximum drive of the response and is subject to adaptation (Do and Yau, 2013), which shapes the intrinsic ipRGC response dramatically (Do and Yau, 2013; Wong et al., 2005). Dim-flash responses were measured prior to saturating responses to minimize light exposure over the course of the protocol.

First, we recorded synaptic light responses by recording the response to dim flashes of full-field, 480-nm light with synaptic transmission intact (Figure 4.2C). The amplitude of the synaptic transient, which was present in a subset of cells (57 of 90 cells), was measured at the intensity required to produce an intrinsic dim flash response of ~5 pA. This transient synaptic response was distinguished from the dim-flash response by the time course (the transient was complete within 500 ms of the flash). The addition of pharmacological blockers of synaptic transmission abolished this response. Furthermore, in a subset of cells (27 of 90 cells), synaptic blockers decreased the holding current and noise. This "synaptic tone" was measured as shown in Figure 4.2D. To examine intrinsic phototransduction, the dim-flash response was then measured in the presence of synaptic blockers (Figure 4.2E). An accurate measure of

the dim-flash sensitivity requires averaging responses together because the amplitude varies depending on the number of melanopsin molecules that are activated (Do et al., 2009). In this study, we averaged 5-10 responses and measured the sensitivity of the intrinsic light response as the amplitude of the averaged dim-flash response divided by the number of photons delivered during the flash (Do et al., 2009). The duration of the response was measured using the integration time, defined as $t_i = \int f(t)dt / f_p$, where $f(t)$ is the response waveform and f_p is the amplitude of the peak (Baylor and Hodgkin, 1973; Do et al., 2009). The intrinsic dim-flash response is fit well with the convolution of two exponentials, $A(e^{\frac{-t}{\tau_1}} - e^{\frac{-t}{\tau_2}})$, (Do et al., 2009) and the time constants of the exponentials were also included in the analysis for each cell.

Figure 4.2. A Protocol for Measurement of the Physiological Parameters that Govern IpRGC Signaling.

(A) Schematic of the protocol used to measure physiological parameters. After seal formation and perforation, current-clamp properties were measured with current injections. The cell was then exposed to 50-ms dim flashes of 480-nm light before and after washing on synaptic blockers that isolate the intrinsic ipRGC response. The saturated response was probed with a 200-ms flash of white light from a xenon source (2.0×10^{-2} μW μm^{-2}, equivalent to 3.8×10^{6} lux) . This light exposure also produced a persistent response, which was measured in a 5-s window, 140 s after the flash.

(B) An example hyperpolarizing current step is shown on the left. The resting voltage was determined prior to any current injections and the input resistance (R_N) was measured from the hyperpolarizing step. A depolarizing current step is shown on the right. The steady spike rate was measured by accounting for the total spikes during the current injection. The interspike intervals (ISIs) were measured and the instantaneous spike rate and coefficient of variations of spiking were calculated.

(C) Example of a baseline-subtracted response to a 480-nm dim flash prior to the addition of synaptic blockers. The amplitude of the synaptic transient was measured as shown. In all cases, these transients were absent after washing on blockers of synaptic transmission. The dashed lines indicate baseline and the amplitude of the synaptic transient. The ensuing current is the beginning of the intrinsic dim-flash response.

(D) In some cells, a decrease in holding current and noise was observed after washing on synaptic blockers (red line). This "synaptic tone" was measured by comparing the current in a 10-s window before addition of synaptic blockers to a 10-s window after addition of synaptic blockers (black bars). The dashed lines indicate the holding current measured in these windows. The cell was periodically probed with step changes in the holding potential to monitor access resistance.

Figure 4.2 (Continued).

(E) An example of an averaged dim-flash response in the presence of blockers of synaptic transmission (black) and its fit by a convolution of two exponentials (blue). The sensitivity was measured by dividing the amplitude by the light intensity. The integration time (t_i) was measured by dividing the area under the curve (AUC) by the amplitude.

(F) An example of a saturated response is shown on the left. The inset is the same response on an expanded time base to illustrate the kinetics of the transient portion of the response. The amplitude, area under the curve (AUC), slope, time to peak, and time to half decay were measured from the saturated response.

(G) An example of the measurement of the persistent response. The baseline and persistent response were measured in 5-s windows, indicated by the arrows and black bars. The gray, dashed lines indicate the baseline current and persistent current. 560-nm light was used to decrease the persistent response. On the right, the 5-s windows are shown to illustrate the difference in noise, which was measured by taking the standard deviation of the current during the 5 s window.

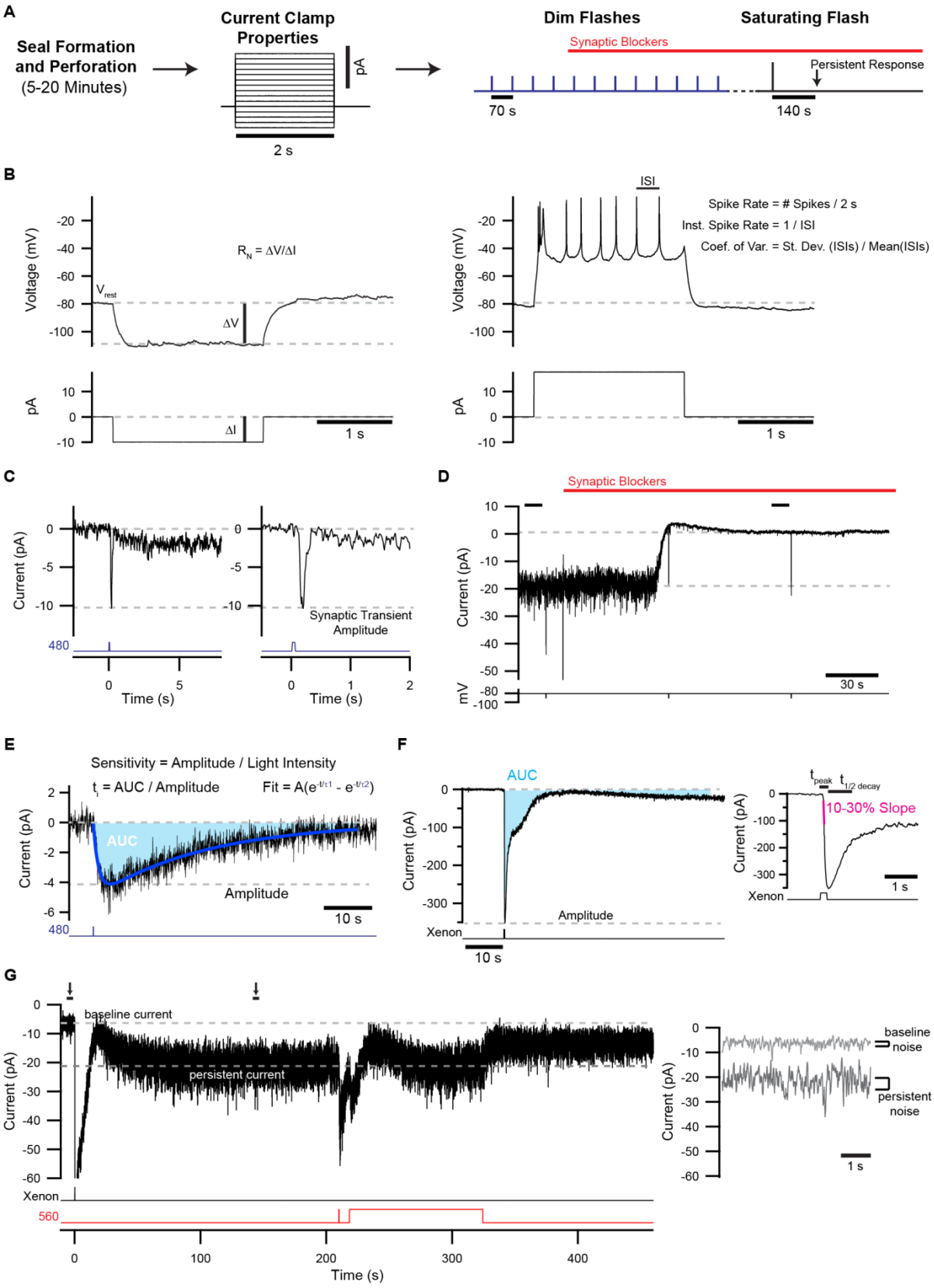

Figure 4.2 (Continued).

The intrinsic saturated response was assayed using an intense flash of white light, which activates ipRGCs similarly to monochromatic, short-wavelength light but allows higher intensities to be achieved (Figure 4.2F). The parameters extracted from analyses of these responses were amplitude, area under the curve (as a measure of duration), slope of activation (10 – 30% of peak), time to peak, and time to half decay (Figure 4.2F). Due to the stability of the active state of melanopsin (Emanuel and Do, 2015), this saturating flash also generated a persistent response (Figure 4.2G), which was measured by comparing the mean and standard deviation of the holding current in a 5-s window beginning 140 s after the flash of white light to a 5-s baseline window immediately preceding the white flash. At this time, the persistent response has stabilized. If the recording was especially long-lived, responses to steps were obtained to observe adaptation. These step responses will be analyzed separately when the sample is sufficiently large.

Diversity in a General Sample of IpRGCs

To examine these physiological properties in a sample of ipRGCs, cells were targeted for perforated-patch recording using the same pseudo-random selection method used for the loose-patch dataset (Figure 4.1). We recorded the properties of 39 ipRGCs identified in this manner and have displayed the distributions of each of the parameters in Figure 4.3. The ranges of these parameters vary widely. For example, the maximum instantaneous spike rate varies over 2 orders of magnitude (Figure 4.3A), the synaptic amplitude varies over 2 orders of magnitude (Figure 4.3B), the dim-flash sensitivity varies over 4 orders of magnitude (Figure 4.3C), and the activation slope of the saturated response varies over 4 orders of magnitude (Figure 4.3D).

Figure 4.3. Distributions of Physiological Parameters of IpRGCs

(A) Probability histograms displaying distributions of intrinsic membrane properties of ipRGCs (n = 39).

(B) Distributions of the amplitudes of the transient synaptic response and the synaptic tone. Only cells with apparent synaptic transients (n = 25) or synaptic tone (n = 12) were included.

(C) Distributions of parameters extracted from dim-flash responses in pharmacological blockade of synaptic transmission.

(D) Distributions of parameters extracted from intrinsic saturated responses and the persistent response.

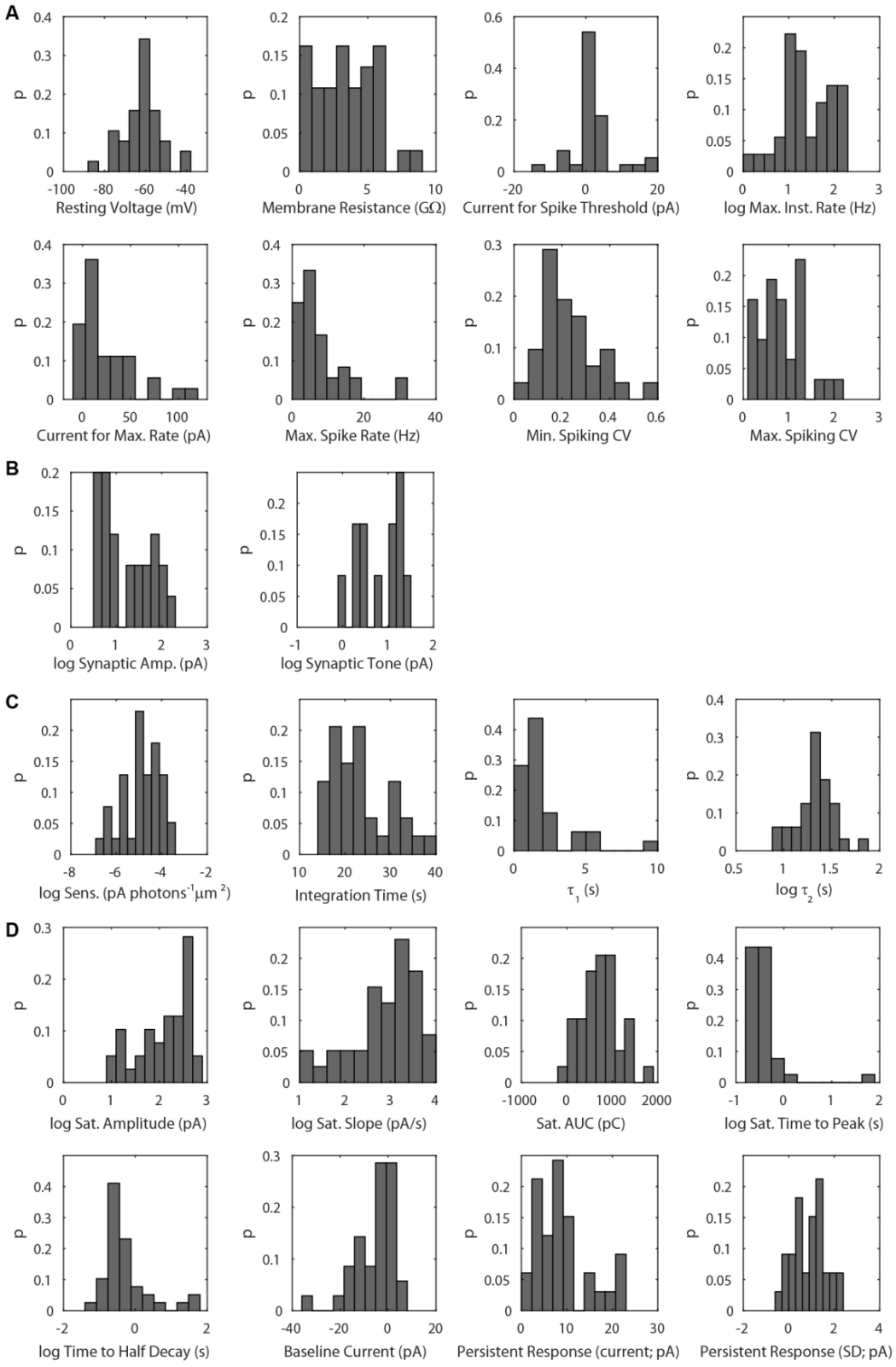

Figure 4.3 (Continued).

Some of this variability is likely due to sampling of ipRGCs from multiple morphologically-defined subtypes. We expect that, due to the nature of our reporter mouse line and our sampling technique, that we are sampling from M1, M2, and possibly M3 cells. Differences in the physiological properties of these subtypes has previously been described (Schmidt and Kofuji, 2009, 2011; Zhao et al., 2014). In a subset of recordings, we gained whole-cell access at the end of the recording and filled the cell with neurobiotin to determine its subtype based on the established criterion of dendritic stratification (Baver et al., 2008; Berson et al., 2010; Schmidt and Kofuji, 2009; Viney et al., 2007). We stained fixed retinas for neurobiotin as well as for nuclei to reveal retinal layers. Filled cells were imaged on a confocal microscope.

We successfully filled 16 of 39 ipRGCs with this technique and found that 9 of these 16 cells had dendritic stratification patterns consistent with M1 ipRGCs; all of their dendrites stratified the outermost portion (OFF sublamina) of the inner plexiform layer (example in Figure 4.4A). The other 7 cells had dendritic stratification patterns consistent with M2 ipRGCs in that all of their dendrites stratified the innermost portion (ON sublamina) of the inner plexiform layer (example in Figure 4.4A). Consistent with previous studies (Berson et al., 2010; Estevez et al., 2012; Schmidt and Kofuji, 2009), the cell bodies of M1 ipRGCs were significantly smaller than those of M2 ipRGCs ($p = 0.0052$, Wilcoxon rank-sum test; Figure 4.4B). Also consistent with previous studies of mouse ipRGCs (Schmidt and Kofuji, 2009; Zhao et al., 2014), there were differences in the physiological properties of M1 and M2 ipRGCs. The saturated amplitude was significantly higher for M1 ipRGCs than M2 ipRGCs ($p = 0.00017$, Wilcoxon rank-sum test) and the maximum spike rate was higher for M2 ipRGCs than M1 ipRGCs ($p = 0.00040$, Wilcoxon rank-sum test; Figure 4.4C). In our sample of filled cells, the proportion of M1 and M2 ipRGCs was similar to that previously reported for the entire population of mouse ipRGCs (Baver et al., 2008; Berson et al., 2010). We did not observe any M3 ipRGCs in our sample, which have bistratified dendritic arbors that branch to both the ON and OFF sublamina of the inner plexiform layer (Berson et al., 2010; Schmidt and Kofuji, 2011). This is expected because we filled a small sample of cells and M3 cells are reported to make up a small proportion of the ipRGC population.

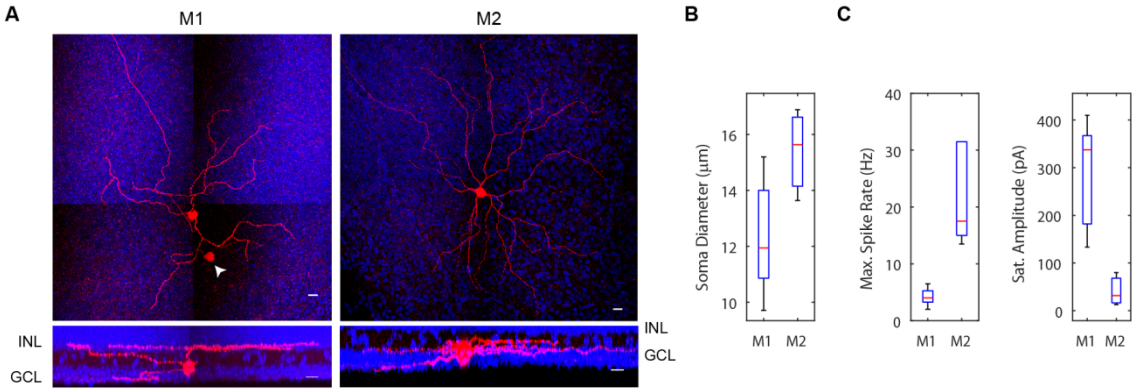

Figure 4.4. Neurobiotin Fills of M1 and M2 IpRGCs

(A) Representative neurobiotin fills of an M1 and an M2 ipRGC. The top row shows Z projections of the neurobiotin fill (red) and nuclear labeling with DAPI (blue). A cell that is likely electrically-coupled to the M1 ipRGC (Müller et al., 2010) is identified with a white arrowhead. The bottom row shows the same cell resliced optically through the Z plane to show the dendritic stratification. At the bottom of the GCL, the axons of both cells can be seen in the resliced images. Scale bars are 15 microns.

(B) Comparison of soma diameters of M1 ipRGCs (n = 9) and M2 ipRGCs (n = 7) with confirmed morphological identity. The red line represents the median, the box represents the interquartile range and the whiskers represent the range. The soma diameter was measured at the beginning of the recording in the live *in vitro* retina.

(C) Comparisons of physiological properties of M1 ipRGCs and M2 ipRGCs. The saturated amplitude is the amplitude of the response of the cell to a 200-ms pulse of intense, white light. The maximum spike rate is the maximum rate observed in a 2-s window with injected current.

We used the physiological properties of filled cells to generate predictions of the morphologies of the unfilled cells. Reduction of the dataset to the first two principal components (see experimental procedures), which explain 42% of the total sample variance, appears to separate the filled M1 and M2 ipRGCs into two, relatively distinct populations (Figure. 4.5A). Linear discriminant analysis was performed by training a classifier on this dimensionality-reduced dataset. The classifier is the line that best discriminates between Gaussian fits of the first two principal components of the filled M1 and M2 ipRGCs (Figure 4.5A). This trained classifier was used to predict the ipRGC subtype of all 39 cells (Figure 4.5B). The resultant prediction indicates that, while ipRGC subtypes can be separated by their physiological properties, there is a large degree of diversity within subtypes. In the first two principal components, the spread within the predicted M1 ipRGCs is similar to the distance between the centers of the predicted M1 and M2 ipRGC samples. Furthermore, the discrimination method misclassified one of seven confirmed M2 ipRGCs as an M1 ipRGC, which suggests that there is overlap in the physiological properties of M1 and M2 ipRGCs.

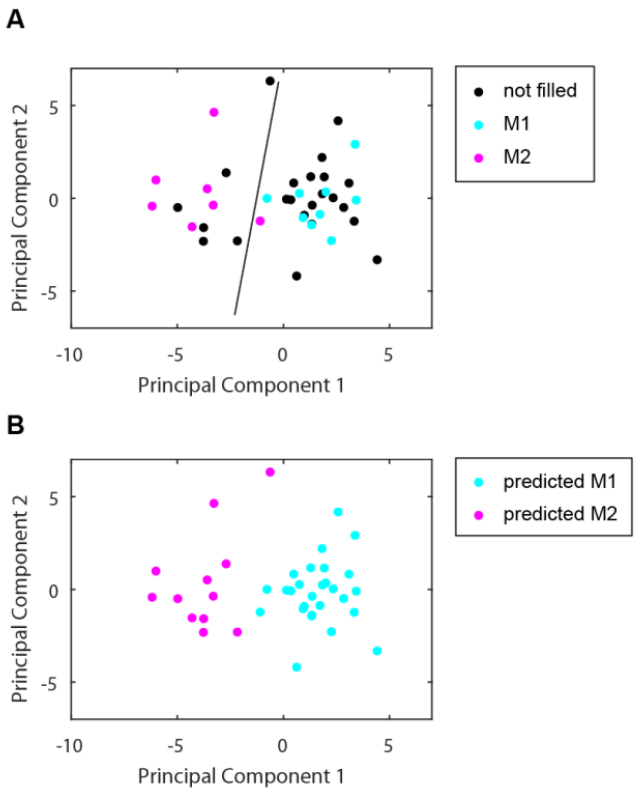

Figure 4.5. Linear Discriminant Analysis for Classification of M1 and M2 IpRGCs.

(A) Principal components one and two of 39 ipRGCs with coloration that represents the morphological identity of 16 filled ipRGCs. The black line is the classifier trained with linear discriminant analysis on the scores of the first two principal components of the filled cells.

(B) Principal components one and two replotted to show the predicted morphology based on the linear discrimination. Note 1 of 7 M2 ipRGCs is misclassified as an M1 ipRGC.

Retrograde-labeled IpRGCs

Because ipRGCs are responsible for various visual functions that use light differently, we tested the hypothesis that the diversity we have observed in the biophysical properties of ipRGCs is tailored to the functions that they drive. We did this by comparing the properties of ipRGCs that project to the hypothalamus to the properties of ipRGCs that project to the pretectum. We injected retrogradely-transported dyes into the hypothalamus of mice to identify hypothalamus-projecting ipRGCs (see experimental procedures; Figure 4.6A). We made relatively large injections that covered multiple retinorecipient nuclei in the hypothalamus in order to produce sufficient numbers of cells for recording. Only a handful of cells in each retina were labeled (example in Figure 4.6B). Every cell retrograde-labeled from hypothalamic injections had an intrinsic light response that was observed in the presence of blockers of synaptic transmission (n = 24 of 24 cells). This observation is consistent with previous studies that indicate that ipRGCs make up ~99% of the input to the SCN of mice, the nucleus within the hypothalamus that is most densely innervated by RGCs (Baver et al., 2008; Morin and Studholme, 2014). Thus, some of our recordings of hypothalamic ipRGCs were made in mice that did not express tdTomato in ipRGCs. No differences were detected in the physiological properties of ipRGCs in wild-type and tdTomato-expressing mice.

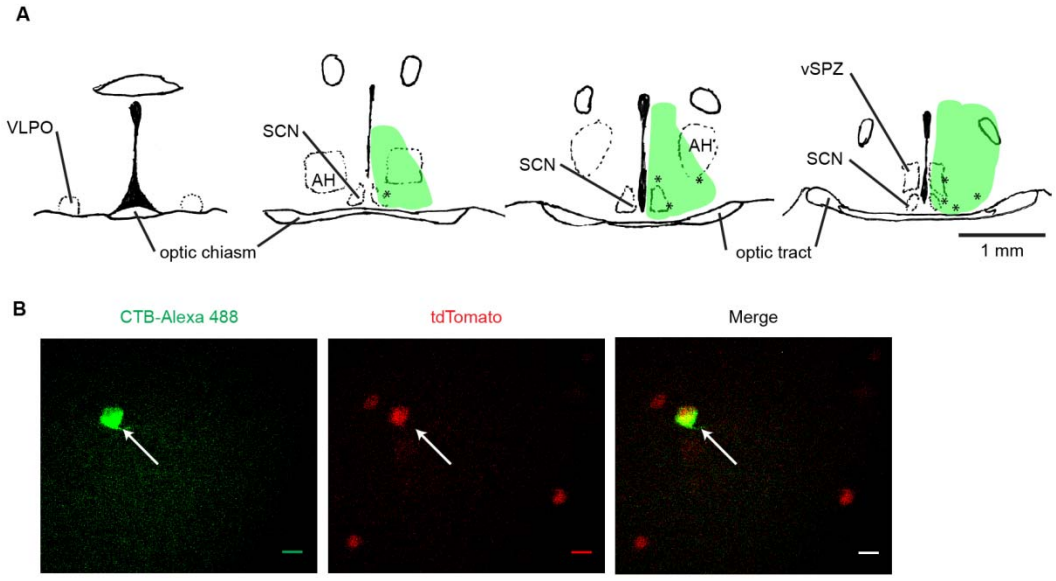

Figure 4.6. Retrograde-labeling of IpRGCs from the Hypothalamus.

(A) Schematics of coronal hypothalamic sections at four rostral-caudal planes. The left-most schematic is most rostral and the right-most schematic is most caudal. The injection locations (asterisks) and the greatest extent of the spread of labels (green), collected for all mice used, are indicated. Retinorecipient areas (Morin and Studholme, 2014) are demarcated with dashed lines. Abbreviations are VLPO for ventral lateral preoptic area, AH for anterior hypothalamus, SCN for suprachiasmatic nucleus, and vSPZ for ventral subparaventricular zone. The schematics are modified from Franklin and Paxinos (2007).

(B) Fluorescent images within a field of view of an *in vitro*, flat-mount retina after injection of cholera toxin b conjugated to Alexa 488 (CTB-Alexa 488) into the hypothalamus of a mouse that expresses tdTomato in ipRGCs. CTB labeling is shown in green and native tdTomato fluorescence is in red. A double-labeled cell is marked by the white arrow. The scale bar is 10 microns.

A similar strategy was used to label ipRGCs that project to the pretectum (Figure 4.7A). To mitigate the concern of labeling fibers passing through the optic tract, which overlies many pretectal nuclei, we targeted the rostral pretectal area. This approach limits the possible uptake of retinal labeling from the optic tract because this area is ventral to a portion of the optic tract that is less dense than more caudal regions of the pretectum. This injection location also decreases the extent to which label spreads to the superior colliculus, another major retinorecipient brain region. Although we cannot rule out labeling that arises from the optic tract, we expect that such labeling is limited because the retrograde labels we used are not thought to label undamaged fibers of passage (Katz et al., 1984; Luppi et al., 1990; Wouterlood and Jorritsma-Byham, 1993) and our injections were medial to the densest portions of the optic tract (Figure 4.7A). Furthermore, the retrograde label was only observed in a small fraction of the total RGCs in the retina. Unlike hypothalamic injections, pretectal injections labeled hundreds of RGCs and most of these labeled cells were not M1-M3 ipRGCs (Figure 4.7B). Therefore, it was necessary to perform these experiments in mice that express tdTomato under the melanopsin promoter (Do et al., 2009) and examine the retinas for cells positive for both the retrogradely-transported label and tdTomato (example in Figure 4.7B).

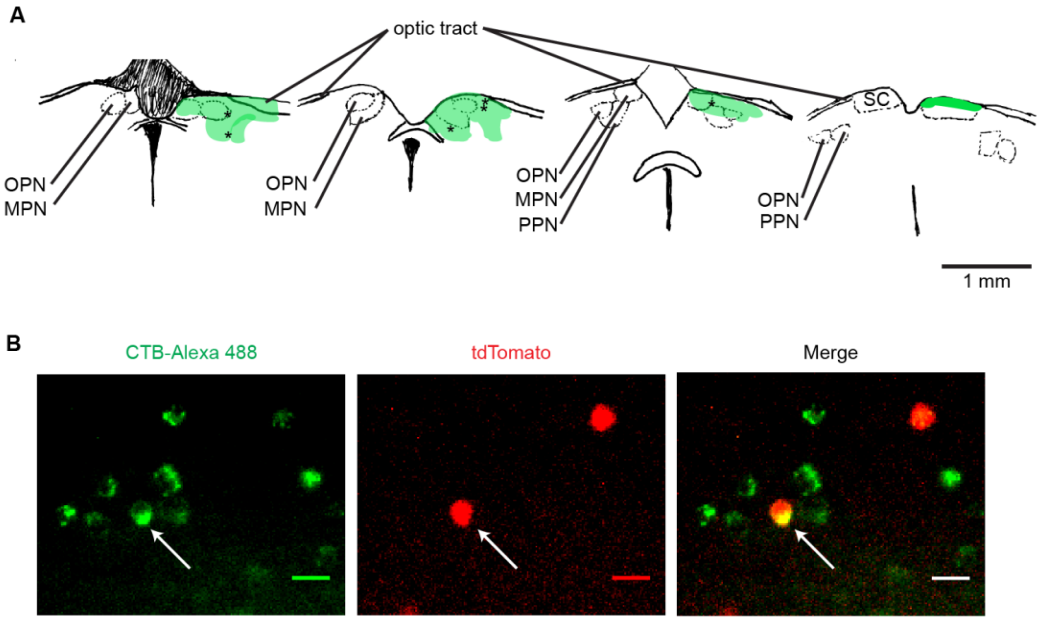

Figure 4.7. Retrograde-labeling of IpRGCs from the Pretectum.

(A) Schematics of coronal pretectal sections at four rostral-caudal planes. The left-most schematic is most rostral and the right-most schematic is most caudal. The injection locations (asterisks) and the greatest extent of the spread of labels (green), collected from all mice used, are indicated. The dye observed in the optic tract could arise from axons of labeled neurons as well as spread of the label into the tract. Retinorecipient areas are demarcated with dashed lines. Abbreviations are OPN for olivary pretectal nucleus, MPN for medial pretectal nucleus, PPN for posterior pretectal nucleus, and SC for superior colliculus. The schematics are modified from Franklin and Paxinos (2007).

(B) Fluorescent images within a field of view of a live, flat-mount retina after injection of CTB conjugated to Alexa 488 into the pretectum. CTB labeling is shown in green and native tdTomato fluorescence is in red. A double-labeled cell is marked by the white arrow. The scale bars are 15 μm.

In total, we applied our recording protocol to 24 ipRGCs that project to the hypothalamus and 27 ipRGCs that project to the pretectum. We found that, similar to the sample of non-retrograde-labeled ipRGCs, many of the parameters we measured varied over wide ranges in both the hypothalamus- and pretectum-projecting cells (Figure 4.8). Some of the parameters that span the broadest ranges are the maximum instantaneous spike rate (distribution shown in Figure 4.8A), the amplitude of the synaptic transient (Figure 4.8B), the dim-flash sensitivity (Figure 4.8C), and the amplitude of the saturated response (Figure 4.8D). We did not observe any statistical differences between the means, medians, or variances of the distributions of any measured parameter from hypothalamus- and pretectum-projecting cells (Figure 4.8). This result suggests both that the physiological properties of these ipRGC populations are highly overlapping and that similar information from ipRGCs is available to both target regions.

Both the retrograde-labeled cells and cells without identified projection targets have physiological properties that span a large range. To ascertain whether all information represented by the general population of M1 and M2 ipRGCs is represented in the retrograde-labeled cells, we compared the biophysical properties of the retrograde-labeled cells to the previously-described sample of non-retrograde-labeled ipRGCs (Figure 4.9). There were no significant differences in the mean, median, or variance of the distributions of any parameter when retrograde-labeled cells were compared to the general population of ipRGCs. This includes parameters extracted from measurement of spiking and intrinsic membrane properties (Figure 4.9A), from synaptic input (Figure 4.9B), from dim-flash responses (Figure 4.9C), and from saturated flash responses (Figure 4.9D). This finding suggests that ipRGCs spanning the entire parameter space project to both the hypothalamus and pretectum and that these brain regions have the entire range of information encoded by M1 and M2 ipRGCs available to them.

Figure 4.8. Comparison of the Physiological Parameters of Hypothalamus-Projecting IpRGCs to Pretectum-Projecting IpRGCs

(A) Probability histograms showing distributions of intrinsic membrane properties for cells identified by retrograde labels injected into the hypothalamus (blue; n = 24) and the pretectum (orange; n = 27).

(B) Distributions of the amplitudes of the transient synaptic response and the synaptic tone. Only cells with apparent synaptic transients (n = 16 and 13 cells labeled from the hypothalamus and pretectum, respectively) or synaptic tone (n = 7 and 8 cells labeled from the hypothalamus and pretectum, respectively) were included.

(C) Distributions of parameters extracted from dim-flash responses with blockade of synaptic transmission.

(D) Distributions of parameters extracted from intrinsic saturated responses and the persistent response.

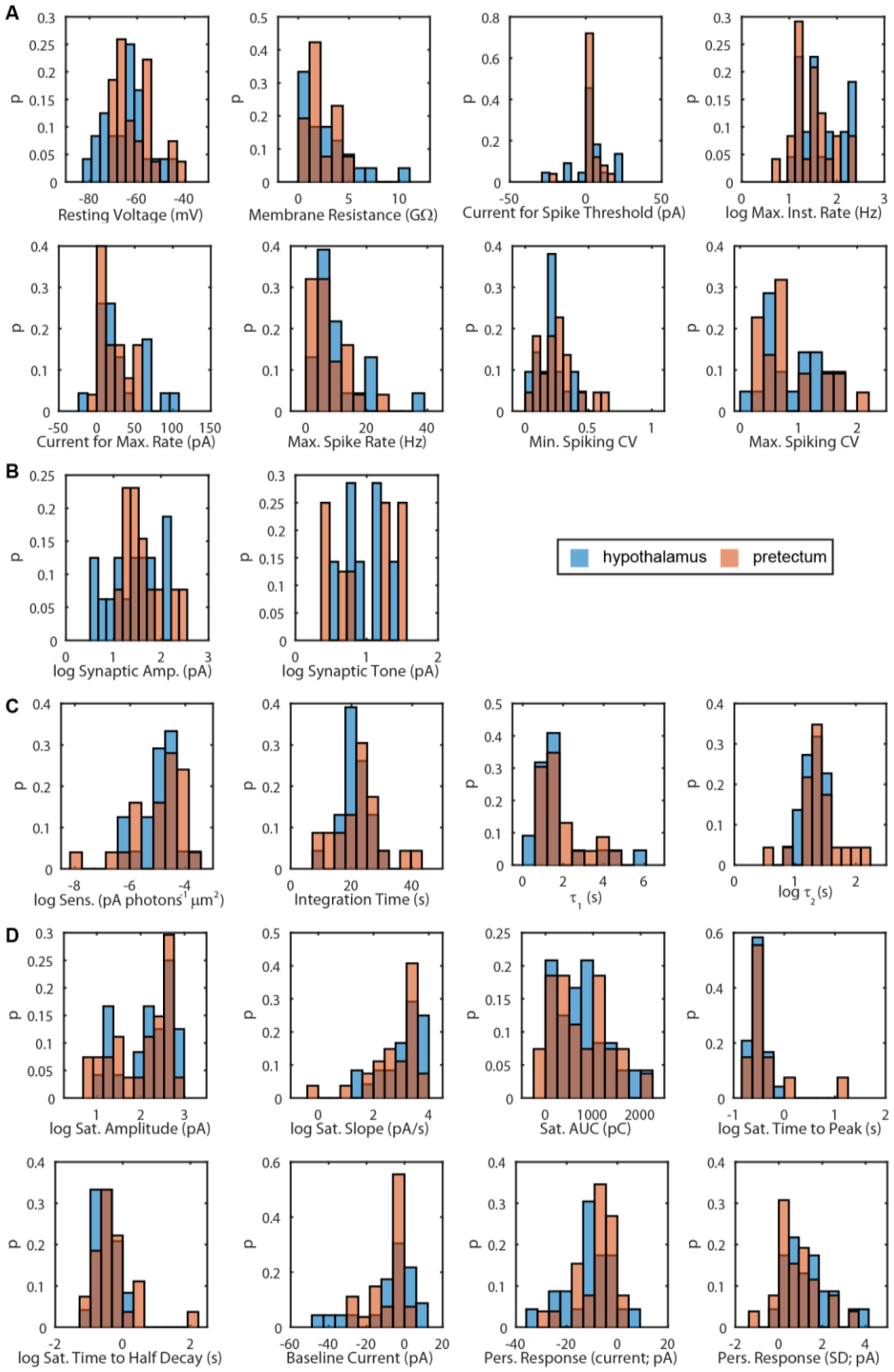

Figure 4.8 (Continued).

Figure 4.9. Comparison of the Physiological Parameters of General, Hypothalamic-Projecting, and Pretectal-Projecting IpRGCs.

(A) Cumulative distributions of intrinsic membrane properties for ipRGCs retrogradely-labeled from the hypothalamus (cyan), ipRGCs retrogradely-labeled from the pretectum (magenta), and non-retrograde-labeled cells (black).

(B) Cumulative distributions of the amplitude of the synaptic transient and the synaptic tone. Note the change in scale due to the large proportions of cells that did not have apparent synaptic transients or an apparent synaptic tone.

(C) Cumulative distributions of parameters extracted from the intrinsic dim-flash response.

(D) Cumulative distributions of parameters extracted from the intrinsic saturated response and the persistent response.

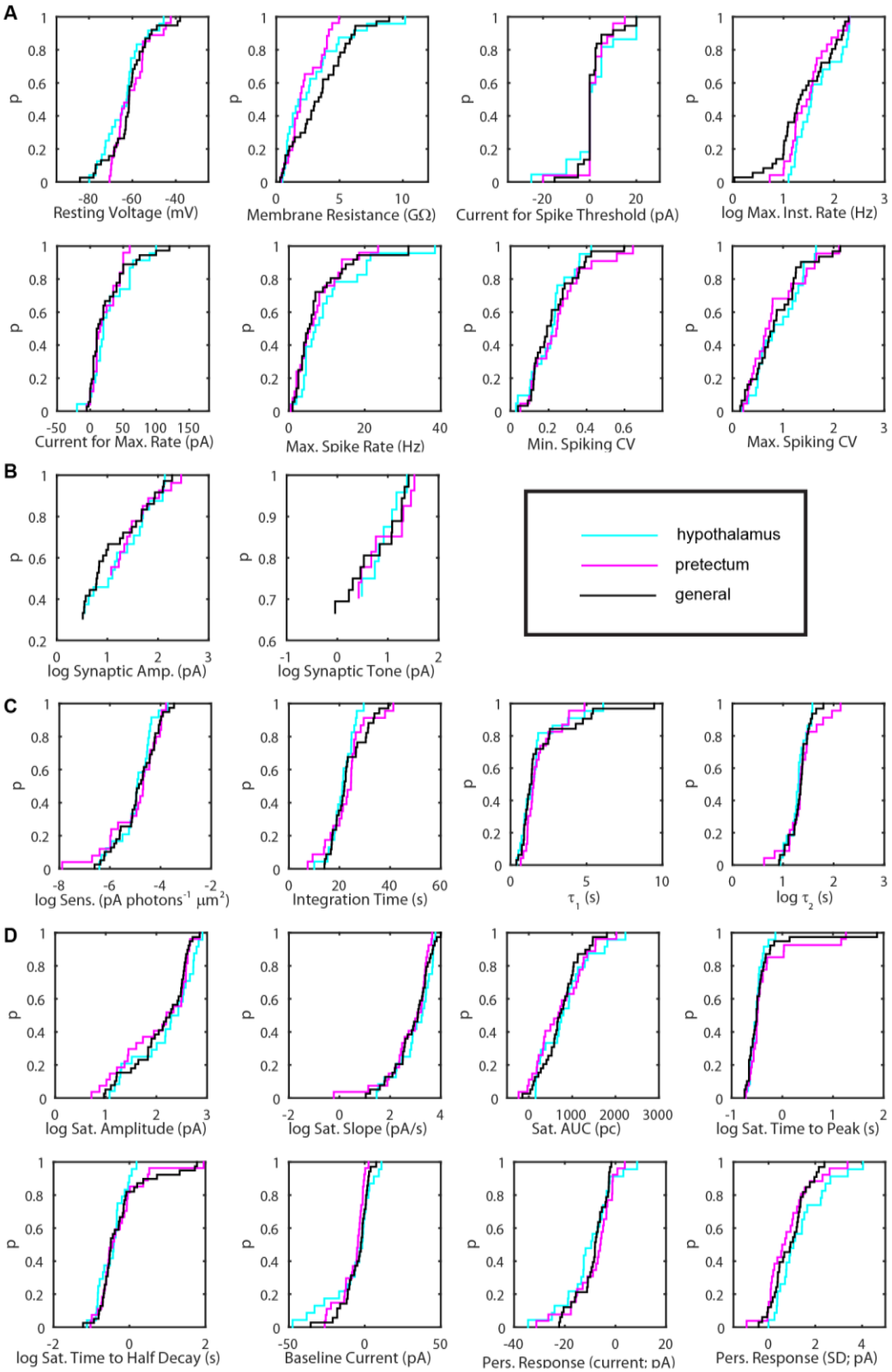

Figure 4.9 (Continued).

Diversity within the Entire Sample

We considered all populations together to examine the extent of diversity within and between ipRGC subtypes. We examined the pairwise correlations among each of the parameters and found that, overall, the correlations are weak (Figure 4.10A-B). The parameters that were most highly correlated (Figure 4.10C) were expected, either because the measurements are closely related (e.g., the activation slope and amplitude of the saturated response) or because of established differences between M1 and M2 ipRGCs, which are both represented within this dataset (e.g., sensitivity and amplitude of the saturated response; Schmidt and Kofuji, 2009).

We reduced the dimensionality of the dataset using principal component analysis on the correlation matrix shown in Figure 4.10A. Consistent with the overlapping distributions we observed for each individual parameter (Figure 4.9), the distributions of the first three principal components of hypothalamus-projecting ipRGCs, pretectum-projecting ipRGCs, and ipRGCs with unidentified targets are highly overlapping (Figure 4.10D). The relatively low proportion of variance explained by these principal components (Figure 4.10D) reflects the low degree of correlation between the parameters (Figure 4.10A)

Figure 4.10. Most Parameters Show Little Correlation in the Entire Sample.

(A) Heatmap showing the Pearson correlation coefficient for comparisons between each measured parameter. The parameters have been sorted to minimize the distance between parameters that are more highly correlated with each other using sparse reverse Cuthill-McKee ordering.

(B) Probability histogram of the distribution of Pearson correlation coefficients for comparisons between each measured parameter, excluding self-correlations.

(C) Scatter plots of the parameter pairs that are most highly correlated. The color of the marker represents the method by which each ipRGC was identified.

(D) Scatter plots that show the relations between the first three principal components, which together explain 53% of the variance in the dataset. The marker colors are the same as in (C).

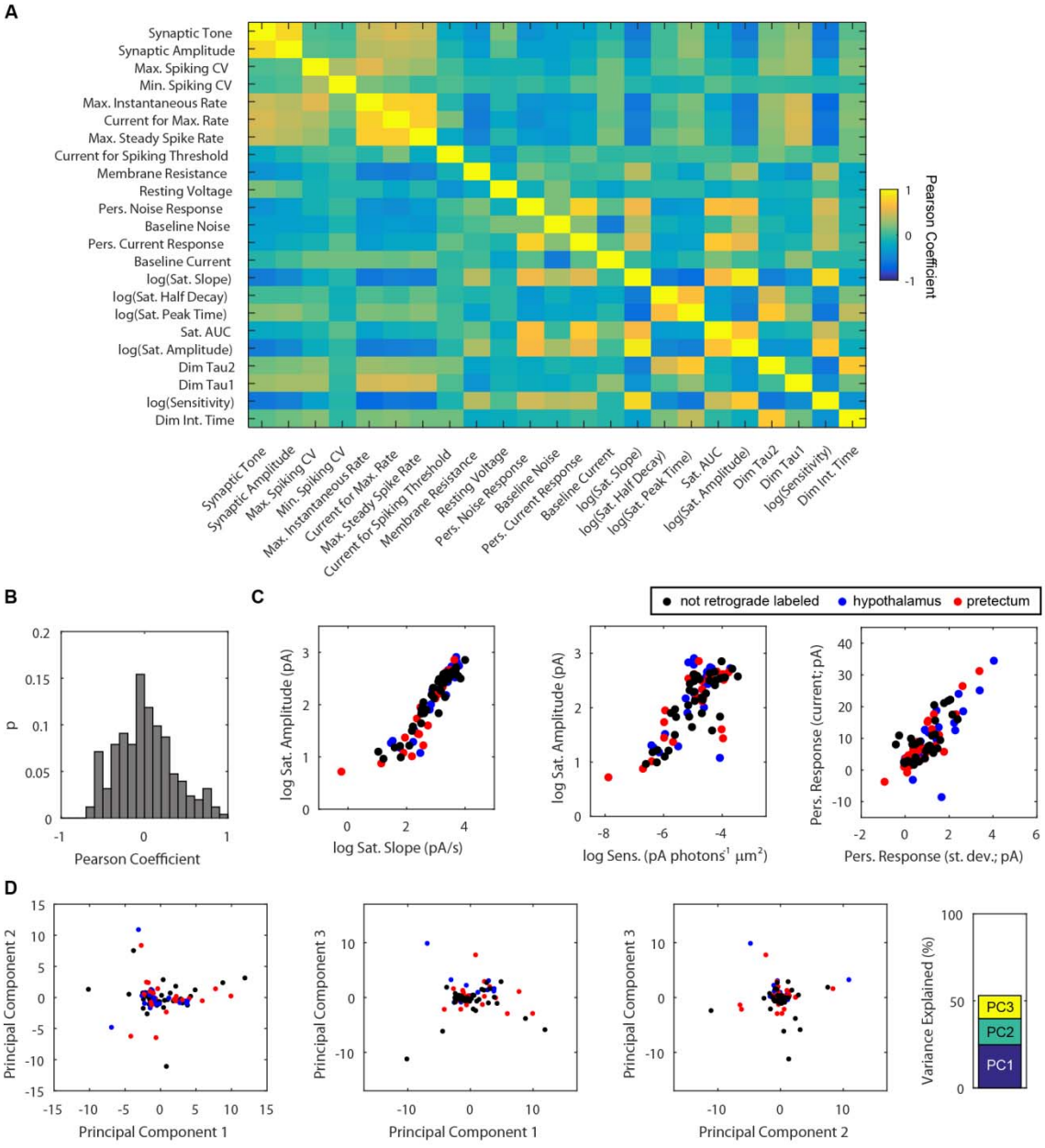

Figure 4.10 (Continued).

In this large sample, there is a high degree of heterogeneity and this is represented in rather continuous distributions across the population. To examine how well M1 and M2 cells can be discriminated and the diversity within these subtypes, we used a linear discrimination approach similar to that described previously (Figure 4.5). Out of 90 total cells, we filled 24 cells. The additional eight filled cells were all from the hypothalamus-projecting sample and were all M1 cells, which is consistent with previous observations that the majority of mouse ipRGCs that project to the SCN are of the M1 subtype (Baver et al., 2008; Chen et al., 2011). The first two principal components and the linear classifier trained on these components are shown in Figure 4.11A. Most filled M1 cells and filled M2 cells are distinguished along the first principal component, which explains 24.8% of the variance of the population. When predictions are made from the classifier, 66 of 90 cells are predicted to be M1 ipRGCs and 24 of 90 cells are predicted to be M2 ipRGCs (Figure 4.11B). The proportion of cells predicted to be M1 ipRGCs in our dataset is larger than the expected proportion of M1 ipRGCs (Baver et al., 2008; Berson et al., 2010). This is likely due to the sampling of retrograde-labeled neurons. The hypothalamus, in particular, appears to receive a large proportion of M1 ipRGCs (Baver et al., 2008; Chen et al., 2011). Furthermore, as suggested before (Figure 4.5), there appears to be a degree of overlap in the physiological properties of M1 and M2 ipRGCs; one of the known M1 ipRGCs was misclassified as an M2 ipRGC and the nature of the representation of physiological properties in the principal component space was continuous.

Because M1 ipRGCs have been specifically implicated in both the entrainment of the circadian clock and the pupillary light reflex (Chen et al., 2011; Güler et al., 2008), we examined the physiological properties of cells predicted to be M1 ipRGCs separately from those predicted to be M2 ipRGCs. Physiological parameters in the predicted M1 ipRGC sample (n = 66 of 90 cells) were even less correlated with each other than those in the full sample (Figure 4.12A-B). The highest correlations are between parameters that are measures of similar aspects of the light response. For example, the slope of activation of the saturated response and the amplitude of the saturated response remain highly correlated in the predicted M1 sample (Figure 4.12C). The two measures of the persistent response also remain highly correlated (Figure 4.12C). On the other hand, the correlation between the dim-flash sensitivity of the cell and the amplitude of the saturated response is much weaker in the M1 sample than

the full sample (Figure 4.12C). This signifies that M2 ipRGCs are consistently both less sensitive and have smaller saturated-response amplitudes than M1 ipRGCs, but that within the M1 population more sensitive cells do not necessarily have larger saturated responses.

Principal component analysis on the sample of predicted M1 ipRGCs reveals that M1 ipRGCs that were labeled from the pretectum (n = 19 of 27 total pretectum-projecting cells) and hypothalamus (n = 19 of 24 total hypothalamus-projecting cells) have highly overlapping physiological properties and that these properties represent the entire spectrum of M1 ipRGC properties (Figure 4.12D). The continuous nature of the representation of the physiological parameters in the first three principal components suggests that the parameters we have analyzed do not distinguish between potential physiological subtypes of the M1 ipRGC population.

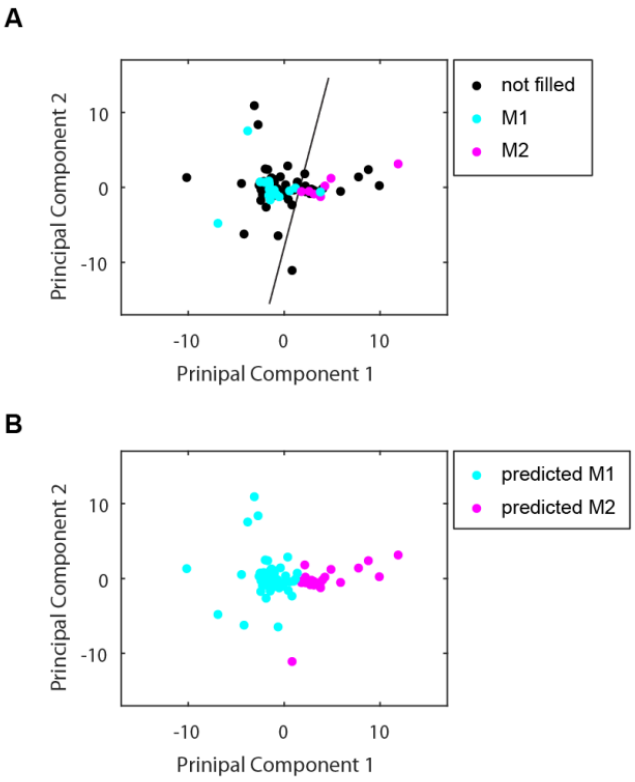

Figure 4.11. Linear Discriminant Analysis for Prediction of M1 and M2 Classifications in the Entire Sample.

(A) Principal components one and two of 90 ipRGCs with coloration that represents the morphological identity of 24 filled ipRGCs. The black line is the classifier trained with linear discriminant analysis on the scores of the first two principal components of the filled cells.

(B) Principal components one and two replotted to show the predicted morphology based on the linear discrimination. Note 1 of 17 M1 ipRGCs is misclassified as an M2 ipRGC.

Figure 4.12. Fewer Correlated Parameters are Apparent in Predicted M1 IpRGCs.

(A) Heatmap showing the Pearson correlation coefficient for comparisons between each measured parameter. The parameters are in the same order as in Figure 4.10A.

(B) Probability histogram of the distribution of Pearson correlation coefficients for comparisons between each measured parameter, excluding self-correlations.

(C) Scatter plots of the same parameter pairs as in Figure 4.10C. The color of the marker represents the method by which each ipRGC was identified.

(D) Scatter plots that show the relations between the first three principal components, which together explain 49% of the variance in the dataset. The marker colors are the same as in (C).

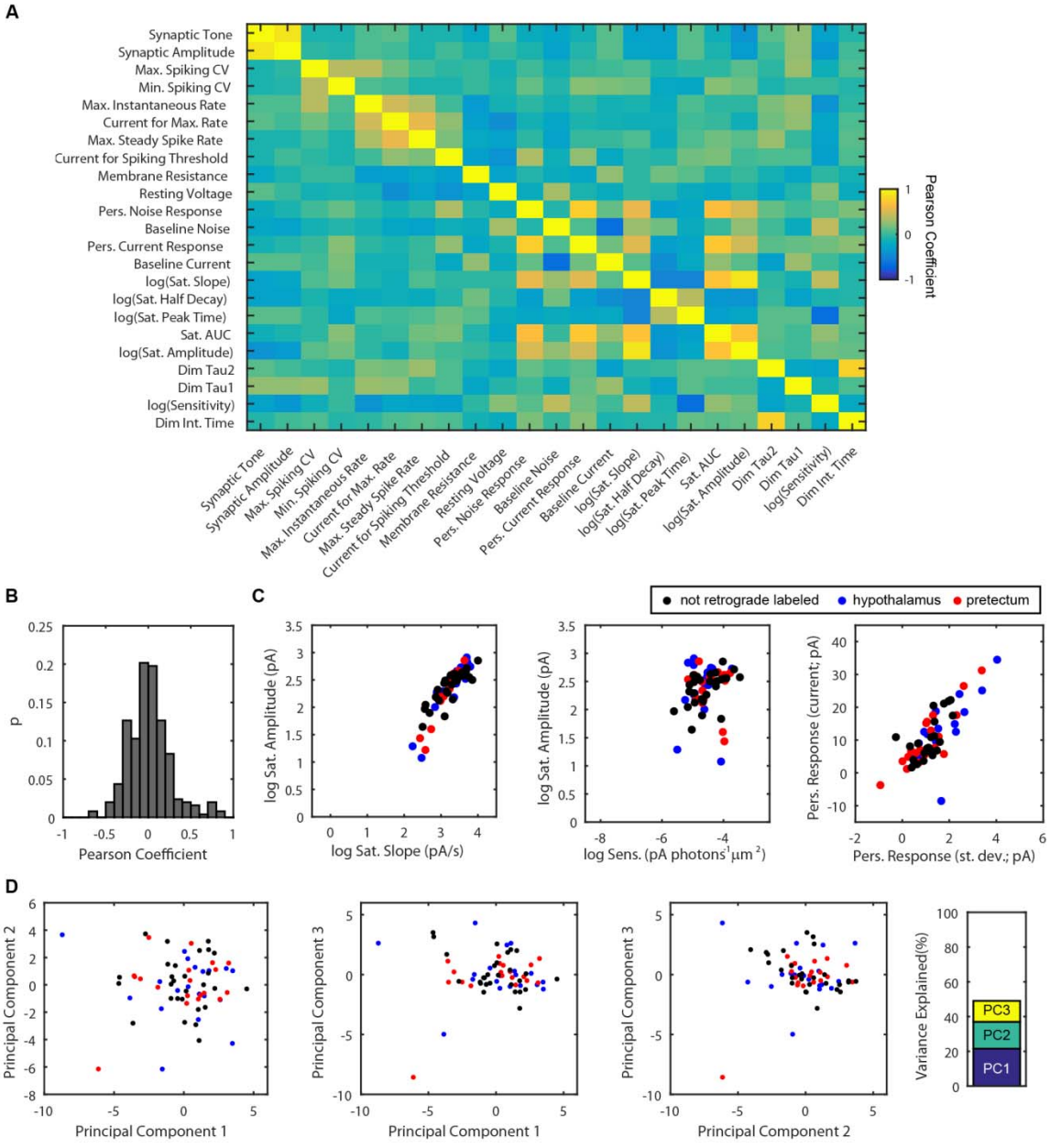

Figure 4.12 (Continued).

Discussion

Using systematic analysis of the physiological parameters of ipRGCs, we have observed a high degree of diversity within ipRGCs that is broadly consistent with variability observed in the light-driven spiking output of these cells. Many individual parameters span extensive ranges and are largely not correlated with each other. We also revealed a previously unrecognized high degree of diversity of physiological parameters within the M1 ipRGC population. In fact, we found that there was some overlap between the physiological properties of M1 and M2 ipRGCs. Furthermore, the diverse intrinsic membrane properties and light responses are not overtly tailored to downstream functions because the properties of ipRGCs that project to two brain regions that are responsible for distinct functions (the hypothalamus and pretectum) are highly overlapping.

A potential source of the variability we observed is the state of the cell or the retina. It has previously been demonstrated that the light responses of rat ipRGCs are mildly modulated in a circadian fashion (Weng et al., 2009) and previous light exposure produces long-lasting effects due to the tristability of the melanopsin molecule (Emanuel and Do, 2015) and adaptation of the light response (Do and Yau, 2013; Wong et al., 2005). We tried to limit these potential sources of variability by performing all recordings in the day (between zeitgeber times 3 and 10, where 0 is lights on) and with dark adaptation prior to recordings of light responses from every cell. Simultaneous recordings of multiple ipRGCs show diverse light responses at the level of spike output (Mawad and Van Gelder, 2008; Tu et al., 2005), which demonstrates variability across ipRGCs that have had the same lighting history. Therefore, we expect that the heterogeneity we have observed is due to actual differences among cells.

Our approach is subject to potential sampling biases. One is that retrograde labels might be taken up by only a subset of ipRGCs. However, this is unlikely to be a concern because we observed no systematic differences between cells labeled with different retrogradely-transported dyes (data not shown) and saw almost complete overlap between physiological properties of the sample of general ipRGCs and the sample of retrograde-labeled cells. Another potential source of sampling bias is that cells that have relatively low expression of melanopsin might not express enough tdTomato to be detected. A careful anatomical study of mouse ipRGCs has shown that the number of M1 ipRGCs is only slightly larger

than the number of M2 ipRGCs (Berson et al., 2010). In the present study, our sampling of M1 ipRGCs (17 confirmed with neurobiotin fills) was at a much higher frequency than M2 ipRGCs (7 confirmed). Though this is a potential consequence of lower tdTomato expression in M2 ipRGCs, it is more likely due to sampling from ipRGCs that target brain regions predominately innervated by M1 ipRGCs (Baver et al., 2008). Finally, our success rate in establishing a perforated-patch recording that is sufficiently stable to complete the protocol is relatively low (~25% of attempts are successful) and presents another potential sampling bias. Although unlikely, it is possible that stable recordings can only be made from a subset of ipRGCs.

We did not observe any differences in the physiological properties of hypothalamus- and pretectum-projecting ipRGCs and it is possible that a substantial proportion of ipRGCs that innervate the hypothalamus have axon collaterals that also innervate the pretectum. Dual innervation of the SCN and OPN has previously been documented in rat (Gooley et al., 2003), and bifurcated ipRGC axons innervating the ipsilateral and contralateral SCN have been observed in hamster (Morin et al., 2003). Therefore, it would not be surprising to find similar innervation patterns in mouse. However, the ablation of cells in mouse that express both melanopsin and the transcription factor, Brn3b, essentially eliminates ipRGC innervation of the OPN but not of the SCN and results in functional ablation of the pupillary light reflex but not circadian photoentrainment (Chen et al., 2011). This demonstrates that some ipRGCs that innervate the SCN do not innervate the OPN. The results of the present study demonstrate that similar information is transmitted through ipRGCs to each region, which suggests that they do not have substantial differences in their biophysical properties even if the cells are distinct.

It remains possible that the pretectal and hypothalamic injections performed in this study are too coarse to differentiate between ipRGCs that regulate discrete functions. The hypothalamic and pretectal injections were not confined to single retinorecipient nuclei as labeling was observed in multiple retinorecipient regions, such as the ventral subparaventricular zone and lateral hypothalamus for hypothalamic injections and the rostral region of the superior colliculus for pretectal injections. Furthermore, individual retinorecipient nuclei within the hypothalamus and pretectum contain multiple, intermingled cell types that themselves may regulate dissimilar functions (Lee et al., 2015; Mieda et al.,

2015; Okoyama and Moriizumi, 2001). Therefore, it would be useful to repeat the analyses performed here on ipRGCs labeled using genetic or circuit strategies that restrict labeling to ipRGCs that innervate particular subtypes of neurons within individual nuclei.

Transsynaptic viral tracing of ipRGCs is one method that can accomplish such restricted labeling. In fact, transsynaptic labeling with pseudorabies virus (PRV152) injected into the anterior chamber of the eye has previously been used to label ipRGCs that are upstream of the pupillary light reflex (Baver et al., 2008; Viney et al., 2007). While transsynaptic labeling customarily renders cells unfit for patch-clamp recording it is encouraging that some light-driven synaptic responses have been recorded in M2 ipRGCs labeled with PRV152 (Viney et al., 2007). Another potential transsynaptic labeling method could label ipRGCs that project to a specific SCN subtype, the vasoactive intestinal polypeptide (VIP) expressing neurons. These cells appear to be important for entrainment of circadian rhythms to light (An et al., 2013) and appear to receive direct retinal innervation (Lokshin et al., 2015). Furthermore, a well-characterized VIP-IRES-Cre mouse allows these neurons to be selectively manipulated (Taniguchi et al., 2011). Therefore, a valuable strategy may be to inject a Cre-dependent, modified rabies virus that retrograde labels cells monosynaptically (Wickersham et al., 2007) into the SCN of VIP-IRES-Cre mice. Again, the main concern is that neurons infected with glycoprotein-deleted rabies virus are not very healthy and may be unfit for patch-clamp electrophysiology, although recent modifications of rabies virus may make recording possible (Reardon et al., 2016). Completing experiments such as these could help clarify whether the physiological properties of ipRGCs are tailored to the functions that they regulate by refining the focus to specific circuits rather than broad brain regions.

Conventional retinal ganglion cells must tile the retina in order to encode spatial information. This is not a requirement of ipRGCs, given that they integrate information over space and time and are considered to be general irradiance encoders. In principal, only one ipRGC is required for irradiance encoding. However, there are many ipRGCs and they completely cover the retina (Berson et al., 2010). The diversity of the physiological properties of these cells might allow the population of ipRGCs to better encode irradiance by pooling over many cells with different properties. Future experiments could establish whether the response heterogeneity improves irradiance encoding. A possible avenue for

accomplishing this is to apply information analyses to the spike trains of ipRGCs, a strategy that has previously provided insights into the value of heterogeneity of physiological properties in other sensory systems (Padmanabhan and Urban, 2014). A similar analysis might help determine the extent to which the diversity we have observed in the properties that govern signal generation in ipRGCs contributes to the information content of the system.

Experimental Procedures

Animals and Stereotaxic Injections

Studies were performed on retinas isolated from wild type C57Bl6/J mice or BAC-transgenic mice that express tdTomato in ipRGCs on a C57Bl6/J background (Do et al., 2009). Mice were postnatal days 23-113, either male or female, and were housed in a 12-hr light/12-hr dark cycle. There was no systematic variation of the parameters with age or sex (data not shown). The Institutional Animal Care and Use Committee of Boston Children's Hospital approved all animal procedures.

For intracranial injection of retrogradely-transported dyes, mice were anesthetized with an intraperitoneal injection of a ketamine/xylazine cocktail (60-100 mg/kg ketamine and 5-10 mg/kg xylazine). Hair on the top of the head was removed by topically applying Nair. The animal was placed in the stereotaxic apparatus (Stoelting), and the surgical site was prepped with betadine and 70% ethanol. Lacrilube ointment was applied to the eyes for lubrication. A midline incision (about 1 cm in length) in the scalp was made with a scalpel, and the exposed skull was cleaned with 3% H_2O_2. The skull was leveled by measuring the z positions at bregma and lambda and adjusting the nose height to correct any difference. For hypothalamic injections, the coordinates were 0.1 mm posterior to bregma, 0.05 mm lateral to the midline, and 5.5 mm ventral to the dura. For pretectal injections, the coordinates were 2.8 mm posterior to bregma, 0.8 mm lateral from the midline, and 1.8 mm ventral to the brain surface. Dyes were injected through a glass pipette with a beveled, 30 μm opening. The injection took place over ~2 minutes, the needle was left in the injection site for 5 minutes, and was withdrawn over two minutes. Meloxicam (5 mg/kg) was administered subcutaneously for analgesia every 24 hours for two days. 100-200 nl of dye was injected into either area. The dyes used in this study were cholera toxin B subunit conjugated to Alexa 488 (Life Technologies, 5 μg/ml in 0.9% sterile saline and 2% dimethylsulfoxide), a

1:10 dilution of red retrobeads in sterile saline (Lumafluor), an undiluted solution of green retrobeads (Lumafluor), or 1:20 dilution of 3 kD dextran conjugated to Alexa 488 in sterile saline (Life Technologies).

Electrophysiology

Mice were dark adapted for at least 1.5 hr prior to anesthetization with Avertin. They were then enucleated and euthanized. The retina was flat-mounted onto a poly-l-lysine-coated coverslip and placed into a recording chamber. Cells were visualized using infrared transillumination (850-nm center wavelength and 30-nm width at half maximum) and differential interference contrast optics. To identify ipRGCs in the BAC-transgenic mice, a field of view of the retina was typically exposed to <1 s of tdTomato excitation light (25-nm bandpass centered on 545 nm, 6×10^9 photons μm^{-2} s^{-1}). GFP excitation light (25-nm bandpass centered on 470 nm, 6×10^9 photons μm^{-2} s^{-1}) was used to identify cells labeled with green beads, dextran, or cholera toxin subunit b. The same excitation light used for tdTomato fluorescence was used to identify cells labeled with red beads in wild-type animals. When GFP excitation light was used, tdTomato excitation light followed to minimize the persistent response (Emanuel and Do, 2015). After identification, cells were dark-adapted for at least 20 minutes prior to measuring light responses.

The inner limiting membrane, which overlies the retinal ganglion cell layer, was removed mechanically with an empty patch pipette. Recording pipettes (3-7 MΩ) were wrapped with parafilm to reduce their capacitance and series resistance was monitored, but not compensated (see below). Recordings were performed at 23 °C as well as 35 °C. The temperature was controlled using an in-line heater and was monitored with a thermistor in the bath. Voltage-clamp recordings were low-pass filtered at 4 kHz and sampled at 10 kHz. Current-clamp recordings were low-pass filtered at 10 kHz and sampled at 50 kHz. For analysis, voltage-clamp traces were digitally low-pass filtered at 10 Hz and resampled at 100 Hz. Analyses for extraction and measurement of parameters from raw traces were performed using Igor Pro and analyses on the extracted parameters were performed using Matlab.

Solutions

The *in vitro* retinas were bathed in ionic Ames solution, which was composed of (in mM) 120 NaCl, 22.6 $NaHCO_3$, 3.1 KCl, 0.5 KH_2PO_4, 6 glucose, 1.2 $CaCl_2$, and 1.2 $MgSO_4$ and equilibrated with

carbogen (95% O_2/5% CO_2). Loose-patch-clamp recordings were performed with HEPES-buffered Ames solution in the pipette. This solution was composed of (in mM) 140 NaCl, 3.1 KCl, 0.5 KH_2PO_4, 6 glucose, 1.2 $CaCl_2$, 1.2 $MgSO_4$, 10 HEPES, pH 7.4 with NaOH. Perforated-patch-clamp recordings were performed with an internal solution composed of (in mM) 110 K-Methanesulfonate, 13 NaCl, 2 $MgCl_2$, 10 EGTA, 1 $CaCl_2$, 10 HEPES, and 0.125-0.25 amphotericin B. The pH was adjusted to 7.2 with KOH. The final [K^+] was 139 mM. In some cases, 0.5% Neurobiotin (Vector Laboratories) was also included in the internal solution to fill cells.

Optical Stimulation

Light from a 75-W xenon arc lamp was filtered to deplete heat while selecting intensity and wavelength. Delivery through a 40× objective produced a spatially uniform, circular stimulus (350-μm diameter) centered on the soma. Electromechanical shutters controlled stimulus timing. Light stimuli were measured at the site of the preparation using a calibrated radiometer and spectrometer. Light delivered through 10-nm bandpass filters was assumed to be of the center wavelength; for broader filters, which were used to identify cells, photon flux was calculated from measured spectra. Photometric units were calculated for white light stimuli using the CIE standard photopic luminosity function (Sharpe et al., 2005). "Flashes" are impulse stimuli, which means that the duration and intensity can be interchanged to produce the same response.

Histology

To determine the location of the stereotaxically injected dye, mice were transcardially perfused with phosphate-buffered saline (PBS) followed by 4% paraformaldehyde after deep anesthesia with Avertin and enucleation. The brain was removed and post-fixed in 4% paraformaldehyde for 1 h. It was cryoprotected in 30% sucrose in PBS (typically 24 h for completion). The brain was frozen in Tissue Tek medium and stored at -20 °C until further processing. Brains were sliced into 35 μm sections on a cryostat (Leica). Every other section was mounted directly to a slide and the other sections were collected free-floating in PBS. Free-floating sections were processed immunohistochemically for structural location markers. Parvalbumin, a calcium binding protein, is expressed in a subset of cells in the OPN (Allen et al., 2011; Okoyama and Moriizumi, 2001). Therefore we used a rabbit anti-parvalbumin antibody

(Swant Pharmaceuticals, PV-25) to mark the location of the OPN in pretectum-injected brains. Free-floating brain sections were permeabilized with 0.1% Triton-X 100 in PBS with three 5-minute washes, then were placed in blocking solution (5% goat serum in PBS with 0.1% Triton-X 100). The sections were incubated in the primary antibody (1:10,000 dilution in the blocking solution) for 3 days at 4 °C. The antibody was removed with three 5-minute washes of 0.1% Triton-X 100-containing PBS. The sections were then incubated in a goat anti-rabbit antibody conjugated to an Alexa Fluor dye (either 555 or 488, depending on the spectrum of the injected dye) at a dilution of 1:500 in blocking solution for 4 h. This antibody was washed off with three 5-minute washes of 0.1% Triton-X 100-contianing PBS followed by three 5-minute washes of PBS. The sections were mounted on slides (Fisher), coverslipped with anti-fade medium (Vectashield), and imaged on an upright epifluorescence scope.

To visualize neurobiotin fills and dendritic stratification of ipRGCs, the retinas were fixed after recording in 4% paraformaldehyde for 30 min. The paraformaldehyde was washed off with two 15-minute washes of PBS, and the retina was permeabilized with two 15-minute washes of 0.1% Triton-X 100 in PBS. The retinas were incubated in Cy3-conjugated streptavidin (1:500 in 0.1% Triton-X 100 in PBS; Jackson Immunoresearch) and 3 μg/ml DAPI overnight at room temperature. The retinas were washed three times (15 minutes each) with 0.1% Triton-X 100 in PBS and then washed three times (15 minutes each wash) with PBS. The retinas were mounted ganglion cell side up on slides (Fisher), coverslipped with anti-fade medium (Vectashield), and imaged on a confocal fluorescence microscope. A spacer (150 μm thick) was included on the slide to prevent the coverslip from flattening the retina.

Principal Component and Linear Discriminant Analyses

Principal component analysis was performed on the extracted parameters using algorithms implemented in Matlab. The base 10 logarithm was taken for parameters with particularly skewed distributions, such as the dim-flash sensitivity and saturated-response amplitude (see variable labels in Figure 4.10 for the identity of these parameters). The observations for each parameter were centered to the mean and normalized by the standard deviation. Some parameters were missing for cells that only were stable partially through the protocol. To estimate missing values (7% of the total observations), an alternating least squares algorithm was used for principal component analysis. We arrived at similar

conclusions when principal component analysis was performed only on cells with no missing observations in any of the parameters (n = 61); we still observe overlap between M1 and M2 ipRGCs and there do not appear to be physiological subtypes within M1 ipRGCs.

Linear discriminant analysis was performed on the first two principal components using Matlab. The classifier was trained with Gaussian fits to the first two principal component scores of the filled M1 ipRGCs and M2 ipRGCs and the line that best differentiates the Gaussian fits was found. For prediction of the morphology of the full sample, the cost of misclassification and the prior probability was equal for M1 and M2 ipRGCs.

Quality Control

One of the main potential sources of technical variability in this study is the electrical access obtained to each cell. Cells recorded with an access resistance greater than 250 MΩ were excluded from the dataset (n = 2 cells). To test whether the access resistance affects the measured parameters across cells, we performed regression analysis. At a significance level of $p < 0.01$, access resistance does not correlate with any other measured parameter. Therefore, it appears that the biological variability supersedes the technical variability introduced by access resistance in these experiments.

Another potential source of technical variability is the potential effect of labeling on the physiology of the cells. We used multiple labeling methods, including fluorescent beads and conjugations of multiple labels were used in this set of experiments. No physiological parameter significantly differed between labels, suggesting that the labels do not differentially affect the physiological parameters we measures for this study. Furthermore, other groups have used these labels for electrophysiology of ipRGCs (Berson et al., 2002; Dacey et al., 2005; Estevez et al., 2012; Zhao et al., 2014) and have not reported deleterious effects.

References

Allen, A.E., Brown, T.M., and Lucas, R.J. (2011). A distinct contribution of short-wavelength-sensitive cones to light-evoked activity in the mouse pretectal olivary nucleus. J. Neurosci. 31, 16833-16843.

An, S., Harang, R., Meeker, K., Granados-Fuentes, D., Tsai, C.A., Mazuski, C., Kim, J., Doyle, F.J., 3rd, Petzold, L.R., and Herzog, E.D. (2013). A neuropeptide speeds circadian entrainment by reducing intercellular synchrony. Proc. Natl. Acad. Sci. USA 110, E4355-4361.

Baver, S.B., Pickard, G.E., and Sollars, P.J. (2008). Two types of melanopsin retinal ganglion cell differentially innervate the hypothalamic suprachiasmatic nucleus and the olivary pretectal nucleus. Eur. J. Neurosci. 27, 1763-1770.

Baylor, D.A., and Hodgkin, A.L. (1973). Detection and resolution of visual stimuli by turtle photoreceptors. J. Physiol. 234, 163-198.

Berson, D.M., Castrucci, A.M., and Provencio, I. (2010). Morphology and mosaics of melanopsin-expressing retinal ganglion cell types in mice. J. Comp. Neurol. 518, 2405-2422.

Berson, D.M., Dunn, F.A., and Takao, M. (2002). Phototransduction by retinal ganglion cells that set the circadian clock. Science 295, 1070-1073.

Chen, S.K., Badea, T.C., and Hattar, S. (2011). Photoentrainment and pupillary light reflex are mediated by distinct populations of ipRGCs. Nature 476, 92-95.

Dacey, D.M., Liao, H.W., Peterson, B.B., Robinson, F.R., Smith, V.C., Pokorny, J., Yau, K.-W., and Gamlin, P.D. (2005). Melanopsin-expressing ganglion cells in primate retina signal colour and irradiance and project to the LGN. Nature 433, 749-754.

Do, M.T.H., and Yau, K.-W. (2013). Adaptation to steady light by intrinsically photosensitive retinal ganglion cells. Proc. Natl. Acad. Sci. USA 110, 7470-7475.

Do, M.T.H., Kang, S.H., Xue, T., Zhong, H., Liao, H.W., Bergles, D.E., and Yau, K.-W. (2009). Photon capture and signalling by melanopsin retinal ganglion cells. Nature 457, 281-287.

Ecker, J.L., Dumitrescu, O.N., Wong, K.Y., Alam, N.M., Chen, S.K., LeGates, T., Renna, J.M., Prusky, G.T., Berson, D.M., and Hattar, S. (2010). Melanopsin-expressing retinal ganglion-cell photoreceptors: cellular diversity and role in pattern vision. Neuron 67, 49-60.

Emanuel, A.J., and Do, M.T.H. (2015). Melanopsin tristability for sustained and broadband phototransduction. Neuron 85, 1043-1055.

Estevez, M.E., Fogerson, P.M., Ilardi, M.C., Borghuis, B.G., Chan, E., Weng, S., Auferkorte, O.N., Demb, J.B., and Berson, D.M. (2012). Form and function of the M4 cell, an intrinsically photosensitive retinal ganglion cell type contributing to geniculocortical vision. J. Neurosci. 32, 13608-13620.

Franklin, K.B.J., and Paxinos, G. (2007). The Mouse Brain in Stereotaxic Coordinates, Third edn (New York, NY: Academic Press).

Gooley, J.J., Lu, J., Fischer, D., and Saper, C.B. (2003). A broad role for melanopsin in nonvisual photoreception. J. Neurosci. 23, 7093-7106.

Güler, A.D., Ecker, J.L., Lall, G.S., Haq, S., Altimus, C.M., Liao, H.W., Barnard, A.R., Cahill, H., Badea, T.C., Zhao, H.*, et al.* (2008). Melanopsin cells are the principal conduits for rod-cone input to non-image-forming vision. Nature 453, 102-105.

Hattar, S., Kumar, M., Park, A., Tong, P., Tung, J., Yau, K.-W., and Berson, D.M. (2006). Central projections of melanopsin-expressing retinal ganglion cells in the mouse. J. Comp. Neurol. 497, 326-349.

Jain, V., Ravindran, E., and Dhingra, N.K. (2012). Differential expression of Brn3 transcription factors in intrinsically photosensitive retinal ganglion cells in mouse. J. Comp. Neurol. 520, 742-755.

Katz, L.C., Burkhalter, A., and Dreyer, W.J. (1984). Fluorescent latex microspheres as a retrograde neuronal marker for *in vivo* and *in vitro* studies of visual cortex. Nature 310, 498-500.

Lee, I.T., Chang, A.S., Manandhar, M., Shan, Y., Fan, J., Izumo, M., Ikeda, Y., Motoike, T., Dixon, S., Seinfeld, J.E.*, et al.* (2015). Neuromedin S-producing neurons act as essential pacemakers in the suprachiasmatic nucleus to couple clock neurons and dictate circadian rhythms. Neuron 85, 1086-1102.

Lokshin, M., LeSauter, J., and Silver, R. (2015). Selective distribution of retinal input to mouse SCN revealed in analysis of sagittal sections. J. Biol. Rhythms 30, 251-257.

Luppi, P.H., Fort, P., and Jouvet, M. (1990). Iontophoretic application of unconjugated cholera toxin B subunit (CTb) combined with immunohistochemistry of neurochemical substances: a method for transmitter identification of retrogradely labeled neurons. Brain Res. 534, 209-224.

Mawad, K., and Van Gelder, R.N. (2008). Absence of long-wavelength photic potentiation of murine intrinsically photosensitive retinal ganglion cell firing *in vitro*. J. Biol. Rhythms 23, 387-391.

Mieda, M., Ono, D., Hasegawa, E., Okamoto, H., Honma, K., Honma, S., and Sakurai, T. (2015). Cellular clocks in AVP neurons of the SCN are critical for interneuronal coupling regulating circadian behavior rhythm. Neuron 85, 1103-1116.

Morin, L.P., Blanchard, J.H., and Provencio, I. (2003). Retinal ganglion cell projections to the hamster suprachiasmatic nucleus, intergeniculate leaflet, and visual midbrain: bifurcation and melanopsin immunoreactivity. J. Comp. Neurol. 465, 401-416.

Morin, L.P., and Studholme, K.M. (2014). Retinofugal projections in the mouse. J. Comp. Neurol. 522, 3733-3753.

Müller, L.P., Do, M.T.H., Yau, K.-W., He, S., and Baldridge, W.H. (2010). Tracer coupling of intrinsically photosensitive retinal ganglion cells to amacrine cells in the mouse retina. J. Comp. Neurol. 518, 4813-4824.

Nelson, D.E., and Takahashi, J.S. (1991). Sensitivity and integration in a visual pathway for circadian entrainment in the hamster (*Mesocricetus auratus*). J. Physiol. 439, 115-145.

Okoyama, S., and Moriizumi, T. (2001). Onset of calbindin-D 28K and parvalbumin expression in the lateral geniculate complex and olivary pretectal nucleus during postnatal development of the rat. Int. J. Dev. Neurosci. 19, 655-661.

Padmanabhan, K., and Urban, N.N. (2014). Disrupting information coding via block of 4-AP-sensitive potassium channels. J. Neurophysiol. 112, 1054-1066.

Reardon, T.R., Murray, A.J., Turi, G.F., Wirblich, C., Croce, K.R., Schnell, M.J., Jessell, T.M., and Losonczy, A. (2016). Rabies Virus CVS-N2c(ΔG) Strain Enhances Retrograde Synaptic Transfer and Neuronal Viability. Neuron 89, 711-724.

Schmidt, T.M., Alam, N.M., Chen, S., Kofuji, P., Li, W., Prusky, G.T., and Hattar, S. (2014). A role for melanopsin in alpha retinal ganglion cells and contrast detection. Neuron 82, 781-788.

Schmidt, T.M., and Kofuji, P. (2009). Functional and morphological differences among intrinsically photosensitive retinal ganglion cells. J. Neurosci. 29, 476-482.

Schmidt, T.M., and Kofuji, P. (2011). Structure and function of bistratified intrinsically photosensitive retinal ganglion cells in the mouse. J. Comp. Neurol. 519, 1492-1504.

Sharpe, L.T., Stockman, A., Jagla, W., and Jagle, H. (2005). A luminous efficiency function, V*(λ), for daylight adaptation. J. Vis. 5, 948-968.

Taniguchi, H., He, M., Wu, P., Kim, S., Paik, R., Sugino, K., Kvitsiani, D., Fu, Y., Lu, J., Lin, Y.*, et al.* (2011). A resource of Cre driver lines for genetic targeting of GABAergic neurons in cerebral cortex. Neuron 71, 995-1013.

Tu, D.C., Zhang, D., Demas, J., Slutsky, E.B., Provencio, I., Holy, T.E., and Van Gelder, R.N. (2005). Physiologic diversity and development of intrinsically photosensitive retinal ganglion cells. Neuron 48, 987-999.

Viney, T.J., Balint, K., Hillier, D., Siegert, S., Boldogkoi, Z., Enquist, L.W., Meister, M., Cepko, C.L., and Roska, B. (2007). Local retinal circuits of melanopsin-containing ganglion cells identified by transsynaptic viral tracing. Curr. Biol. 17, 981-988.

Weng, S., Wong, K.Y., and Berson, D.M. (2009). Circadian modulation of melanopsin-driven light response in rat ganglion-cell photoreceptors. J. Biol. Rhythms 24, 391-402.

Wickersham, I.R., Lyon, D.C., Barnard, R.J., Mori, T., Finke, S., Conzelmann, K.K., Young, J.A., and Callaway, E.M. (2007). Monosynaptic restriction of transsynaptic tracing from single, genetically targeted neurons. Neuron 53, 639-647.

Wong, K.Y., Dunn, F.A., and Berson, D.M. (2005). Photoreceptor adaptation in intrinsically photosensitive retinal ganglion cells. Neuron 48, 1001-1010.

Wouterlood, F.G., and Jorritsma-Byham, B. (1993). The anterograde neuroanatomical tracer biotinylated dextran-amine: comparison with the tracer *Phaseolus vulgaris*-leucoagglutinin in preparations for electron microscopy. J. Neurosci. Methods 48, 75-87.

Xue, T., Do, M.T.H., Riccio, A., Jiang, Z., Hsieh, J., Wang, H.C., Merbs, S.L., Welsbie, D.S., Yoshioka, T., Weissgerber, P.*, et al.* (2011). Melanopsin signalling in mammalian iris and retina. Nature 479, 67-73.

Zhao, X., Stafford, B.K., Godin, A.L., King, W.M., and Wong, K.Y. (2014). Photoresponse diversity among the five types of intrinsically photosensitive retinal ganglion cells. J. Physiol. 592, 1619-1636.

Chapter 5: Concluding Remarks

Alan Joseph Emanuel

The goal of my dissertation has been to better our understanding of intrinsically photosensitive retinal ganglion cells (ipRGCs), which form a class of sensory cells that are responsible for the regulation of many visual functions. The main role of these cells appears to be providing information about the overall light intensity to downstream functions. The experiments described in this thesis reveal that the pigment expressed in ipRGCs (melanopsin) has three thermally stable states and that this property of melanopsin helps ipRGCs generate signals tailored to its role in irradiance encoding. In particular, melanopsin tristability allows ipRGCs to integrate light over time and wavelength (Chapter 2; Emanuel and Do, 2015). Furthermore, the stability of the active state affects the activation and adaptation of the intrinsic response of ipRGCs (Chapter 3).

This dissertation has also focused on the diversification of signals generated by ipRGCs. In mouse, there are multiple anatomical subtypes of ipRGCs, which have been shown to have different physiological properties and play roles in distinct visual functions (Chen et al., 2011; Ecker et al., 2010; Estevez et al., 2012; Schmidt et al., 2014; Schmidt and Kofuji, 2009, 2011; Zhao et al., 2014) and some ipRGC subtypes, alone, regulate multiple functions with projections to multiple brain regions (Baver et al., 2008; Chen et al., 2011; Hattar et al., 2006). Chapter 4 of this thesis examined the diversity in ipRGC signal generation and demonstrated that both the spike output and the biophysical properties that contribute to signal generation in ipRGCs are highly variable from cell to cell, even within anatomically-defined ipRGC subtypes (Chapter 4). Furthermore, this variability is represented in ipRGCs that project to either of two regions that regulate behaviors that respond to light differently, suggesting that the purpose of the heterogeneity is not to provide distinct information to different downstream regions, but perhaps to help ipRGCs encode irradiance efficiently. The diversity also raises the possibility that other characteristics of visual stimuli are encoded by ipRGCs.

At this point in time, we are certainly far from having a comprehensive understanding of the functions of ipRGCs and the signals that they generate. These experiments point toward a number of future directions that could help us achieve that goal.

An unresolved issue, for example, is whether the tristability of melanopsin observed in ipRGCs using electrophysiology (Emanuel and Do, 2015) is the same as that observed of purified mouse

melanopsin biochemically (Matsuyama et al., 2012). The spectral properties of the states are similar between the two studies and a model based on biochemical parameters reliably predicts the physiological effects of light on ipRGCs. To confirm that the states observed in the two studies are one and the same, however, it would be important to determine whether melanopsin in ipRGCs uses the same chromophores observed in the biochemical experiments. This could be done by isolating 7-*cis* retinal, the chromophore associated with extramelanopsin (Matsuyama et al., 2012), from ipRGCs in the same conditions in which we observe the violet state, which has a similar spectrum to extramelanopsin. Accomplishing this is technically challenging due to the scarcity of ipRGCs and the low melanopsin expression within ipRGCs. However, it may be possible to isolate enough chromophore from melanopsin for detection of the various isomers by purifying large numbers of ipRGCs (via cell sorting; Walker et al., 2008) or by isolating chromophore from retinas that only have functional ipRGCs and not rods or cones. This might be possible by examining chromophore extracted from retinas of young mice that have not yet developed rods or cones or in genetically altered mice in which the outer retinas degenerate with age. We have collaborated with biochemists to conduct pilot experiments, but we expect that the technical challenges will make this line of research a long-term undertaking.

Another unresolved issue related to Chapters 2 and 3 is the way in which melanopsin reverts to the ground (cyan) state. After prolonged periods of dark adaptation, melanopsin in ipRGCs is only found in the ground state, both biochemically (Walker et al., 2008) and electrophysiologically (Emanuel and Do, 2015). This observation demonstrates the necessity of a light-independent process for regeneration of the ground state because we predict that the maximum fraction of the cyan state that can be obtained with any light exposure is ~20% (Emanuel and Do, 2015). This regeneration may be accomplished via bleaching, where the meta or violet states dissociate from their chromophores and are resupplied with 11-*cis* retinal. Alternatively, this may be accomplished by expression of new melanopsin molecules after recycling activated melanopsin molecules. These scenarios are not mutually exclusive and I would not be surprised if future research reveals that there are multiple mechanisms for regeneration of the ground state of melanopsin. The rate and method by which the ground state of melanopsin regenerates is expected to influence the signal generation of ipRGCs because the intrinsic photosensitivity depends on

the availability of melanopsin molecules to capture light (which would increase as melanopsin is regenerated). Hence, a thorough understanding of the melanopsin pigment cycle will help us better understand how ipRGCs generate signals.

The diversity observed in the physiological parameters underlying ipRGC signal generation (Chapter 4) also raises a number of questions, including what is the purpose of this diversity? From the retrograde-labeling studies, there is no evidence that signals are divergently relayed to particular brain regions, but the regions from which ipRGCs were labeled are broad and could be involved in many different functions. For example, the main retinorecipient nucleus of the hypothalamus, the suprachiasmatic nucleus (SCN), contains multiple, retinorecipient subtypes that could play different visual roles. These subtypes differentially receive retinal input (Karatsoreos et al., 2004; Lokshin et al., 2015; Morin and Allen, 2006). Likewise, the pretectal nucleus that receives ipRGC input is made up of multiple cell types (Okoyama and Moriizumi, 2001) and the functions regulated by each of these subtypes are currently unknown. Therefore, a more targeted experimental approach where the ipRGC input into specific circuits is investigated could reveal that the heterogeneity observed in ipRGC physiological properties divides among these specific circuits. However, it is also possible that the diversity serves other purposes. It may be more efficient to encode light intensity with diverse sensitivity tuning and physiological properties than with a stereotyped output. The value of diversity for efficient coding is realized in other sensory systems. For example, heterogeneity in the intrinsic physiological properties of mitral cells in the olfactory system enhance the robustness and efficiency of encoding dynamic olfactory stimuli (Padmanabhan and Urban, 2014; Tripathy et al., 2013). Another recent example suggests that heterogeneity in visual responses in mouse visual cortex is important for encoding behaviorally-detected tasks (Montijn et al., 2015).

In light of these observations, an intriguing future research direction would be to determine how the heterogeneity in ipRGC physiological properties contributes to their role in sensory encoding. One potential avenue for doing so is to artificially reduce the diversity in ipRGC output. Ideally, one would know the source of diversity so that it would be easy to manipulate. For example, if the expression level of melanopsin contributes to most of the heterogeneity, overexpressing melanopsin with a strong

promoter in all ipRGCs could result in a less diverse output. Another way to control diversity would be to directly drive spiking patterns in all ipRGCs, perhaps with optogenetic manipulations. With either approach, one could compare the functions regulated by ipRGCs with and without manipulations of the heterogeneity to observe the consequences of physiological diversity.

In all, the experiments described within this dissertation have revealed a new mechanism by which visual pigments can operate in physiological conditions and demonstrated a large degree of diversity within a molecularly-defined cell type. Lately, great interest has arisen in the optimal design of the lighting in our environment due to the increased recognition of the importance of melanopsin and ipRGC signaling for regulation of the circadian clock (Lucas et al., 2014) as well as for psychiatric health (Roecklein et al., 2009). I hope that the contributions of this dissertation to the understanding of melanopsin and ipRGC signaling, along with the past and future work on these topics, will help with the design of lighting for the optimization of individual and public health.

References

Baver, S.B., Pickard, G.E., and Sollars, P.J. (2008). Two types of melanopsin retinal ganglion cell differentially innervate the hypothalamic suprachiasmatic nucleus and the olivary pretectal nucleus. Eur. J. Neurosci. 27, 1763-1770.

Chen, S.K., Badea, T.C., and Hattar, S. (2011). Photoentrainment and pupillary light reflex are mediated by distinct populations of ipRGCs. Nature 476, 92-95.

Ecker, J.L., Dumitrescu, O.N., Wong, K.Y., Alam, N.M., Chen, S.K., LeGates, T., Renna, J.M., Prusky, G.T., Berson, D.M., and Hattar, S. (2010). Melanopsin-expressing retinal ganglion-cell photoreceptors: cellular diversity and role in pattern vision. Neuron 67, 49-60.

Emanuel, A.J., and Do, M.T.H. (2015). Melanopsin tristability for sustained and broadband phototransduction. Neuron 85, 1043-1055.

Estevez, M.E., Fogerson, P.M., Ilardi, M.C., Borghuis, B.G., Chan, E., Weng, S., Auferkorte, O.N., Demb, J.B., and Berson, D.M. (2012). Form and function of the M4 cell, an intrinsically photosensitive retinal ganglion cell type contributing to geniculocortical vision. J. Neurosci. 32, 13608-13620.

Hattar, S., Kumar, M., Park, A., Tong, P., Tung, J., Yau, K.-W., and Berson, D.M. (2006). Central projections of melanopsin-expressing retinal ganglion cells in the mouse. J. Comp. Neurol. 497, 326-349.

Karatsoreos, I.N., Yan, L., LeSauter, J., and Silver, R. (2004). Phenotype matters: identification of light-responsive cells in the mouse suprachiasmatic nucleus. J. Neurosci. 24, 68-75.

Lokshin, M., LeSauter, J., and Silver, R. (2015). Selective distribution of retinal input to mouse SCN revealed in analysis of sagittal sections. J. Biol. Rhythms 30, 251-257.

Lucas, R.J., Peirson, S.N., Berson, D.M., Brown, T.M., Cooper, H.M., Czeisler, C.A., Figueiro, M.G., Gamlin, P.D., Lockley, S.W., O'Hagan, J.B.*, et al.* (2014). Measuring and using light in the melanopsin age. Trends Neurosci. 37, 1-9.

Matsuyama, T., Yamashita, T., Imamoto, Y., and Shichida, Y. (2012). Photochemical properties of mammalian melanopsin. Biochemistry 51, 5454-5462.

Montijn, J.S., Goltstein, P.M., and Pennartz, C.M. (2015). Mouse V1 population correlates of visual detection rely on heterogeneity within neuronal response patterns. Elife 4.

Morin, L.P., and Allen, C.N. (2006). The circadian visual system, 2005. Brain Res. Rev. 51, 1-60.

Okoyama, S., and Moriizumi, T. (2001). Onset of calbindin-D 28K and parvalbumin expression in the lateral geniculate complex and olivary pretectal nucleus during postnatal development of the rat. Int. J. Dev. Neurosci. 19, 655-661.

Padmanabhan, K., and Urban, N.N. (2014). Disrupting information coding via block of 4-AP-sensitive potassium channels. J. Neurophysiol. 112, 1054-1066.

Roecklein, K.A., Rohan, K.J., Duncan, W.C., Rollag, M.D., Rosenthal, N.E., Lipsky, R.H., and Provencio, I. (2009). A missense variant (P10L) of the melanopsin (OPN4) gene in seasonal affective disorder. J. Affect. Disord. 114, 279-285.

Schmidt, T.M., Alam, N.M., Chen, S., Kofuji, P., Li, W., Prusky, G.T., and Hattar, S. (2014). A role for melanopsin in alpha retinal ganglion cells and contrast detection. Neuron 82, 781-788.

Schmidt, T.M., and Kofuji, P. (2009). Functional and morphological differences among intrinsically photosensitive retinal ganglion cells. J. Neurosci. 29, 476-482.

Schmidt, T.M., and Kofuji, P. (2011). Structure and function of bistratified intrinsically photosensitive retinal ganglion cells in the mouse. J. Comp. Neurol. 519, 1492-1504.

Tripathy, S.J., Padmanabhan, K., Gerkin, R.C., and Urban, N.N. (2013). Intermediate intrinsic diversity enhances neural population coding. Proc. Natl. Acad. Sci. USA 110, 8248-8253.

Walker, M.T., Brown, R.L., Cronin, T.W., and Robinson, P.R. (2008). Photochemistry of retinal chromophore in mouse melanopsin. Proc. Natl. Acad. Sci. USA 105, 8861-8865.

Zhao, X., Stafford, B.K., Godin, A.L., King, W.M., and Wong, K.Y. (2014). Photoresponse diversity among the five types of intrinsically photosensitive retinal ganglion cells. J. Physiol. 592, 1619-1636.

Appendix 1: Supplementary Information for "Melanopsin Tristability for Sustained and Broadband Phototransduction"

Supplemental Data

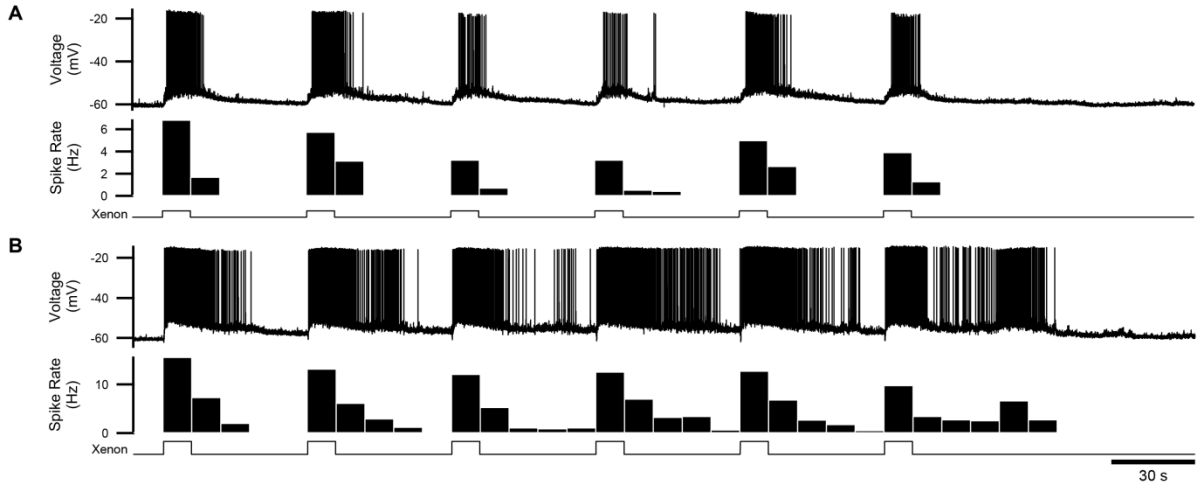

Figure S1, Related to Figure 2.1. Dependence of Temporal Integration on Light Intensity.

(A) Membrane voltage (top) and spike rate (bottom, in 10-s bins) of an ipRGC illuminated with six pulses of xenon light (10-s each, 2.0×10^{-6} $\mu W\ \mu m^{-2}$, equivalent to 2.6×10^{3} lux). (B) The same cell and protocol but with a higher intensity of xenon light (2.5×10^{-5} $\mu W\ \mu m^{-2}$, equivalent to 3.3×10^{4} lux). Recordings were made at 35 °C with synaptic transmission intact.

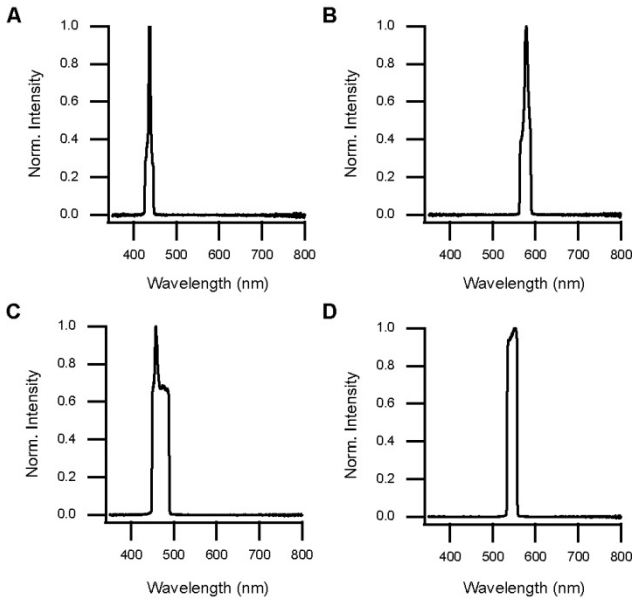

Figure S2, Related to Figures 2.2 and 2.3. Spectra and Intensities of Light Stimuli. (A) Short-wavelength stimulus used in Figures 2.2A, 2.2C, 2.2D, and 2.3A at an intensity of 4×10^{10} photons μm^{-2} s^{-1}. This stimulus was also used in the current-clamp experiments that tested for persistent responses during pharmacological block of synaptic transmission. (B) Long-wavelength stimulus used in Figures 2.2A, 2.2C, 2.2D, and 2.3A at an intensity of 7×10^{10} photons μm^{-2} s^{-1}. (C) Short-wavelength stimulus used in Figure 2.2B at an intensity of 3×10^{10} photons μm^{-2} s^{-1}. (D) Excitation light used to identify tdTomato-positive ipRGCs at an intensity of 5×10^{10} photons μm^{-2} s^{-1}. This is identical to the long-wavelength stimulus used in Figure 2.2B.

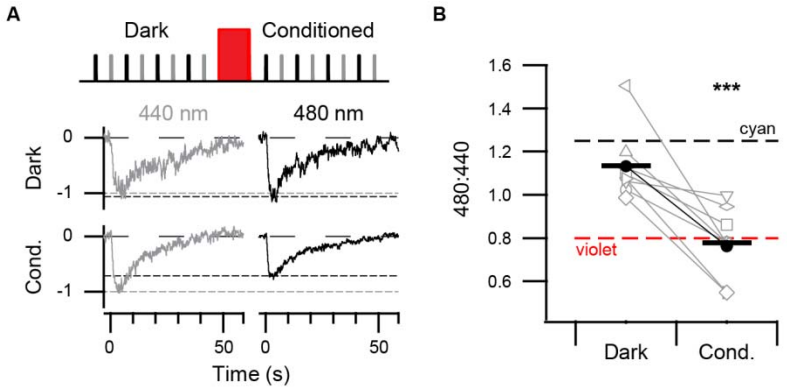

Figure S3, Related to Figure 2.4. Inducing the Violet State with a Period of Conditioning Light. (A) From the action spectra of the cyan and violet states, an ipRGC should be more sensitive to 480- than 440-nm light if all melanopsin is in the cyan state (ratio of sensitivities to 480- and 440-nm light of 1.25) but the opposite should be true for the violet state (ratio of 0.80). Illustrated is the protocol for measuring dim-flash sensitivities to 480-nm and 440-nm light before and after a 560-nm conditioning step (top). Representative dim-flash responses (bottom). All responses are normalized to the peak of the 440-nm responses. The peaks of the 440- and 480-nm responses are marked by gray and black dashed lines, respectively, for ease of comparison. (B) The 480:440 sensitivity ratio for all cells in each condition. Closed symbols denote the cell in A and bars are population means. Dashed black and red lines represent the ratio expected if all pigment is in the cyan and violet state, respectively. Asterisks signify statistical significance. Sensitivity ratios were 1.15 ± 0.05 during dark adaptation and 0.78 ± 0.05 following the conditioning light ($n = 9$ cells, $p < 0.001$). The slight deviation from the theoretical ratios is likely due to a small amount of the violet state remaining from the fluorescence-identification of ipRGCs; that is, incomplete dark adaptation. These experiments suggest that the violet state has a high degree of stability in ipRGCs (at 23 °C where these experiments were performed) because measuring it required a period of >10 min after the conditioning light ceased (Supplemental Experimental Procedures). Synaptic transmission was blocked in these experiments.

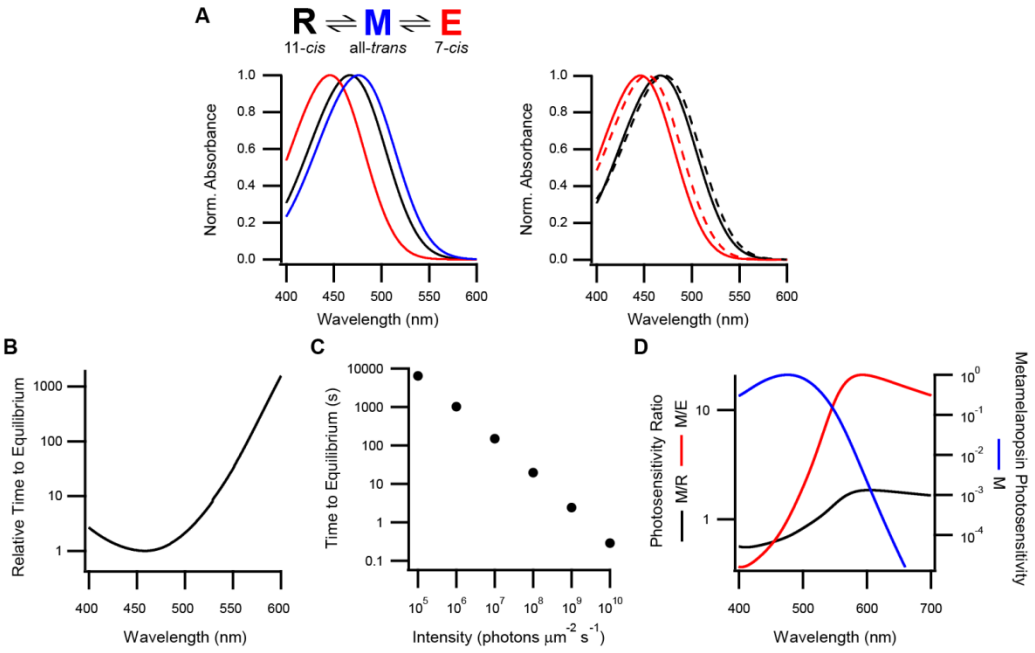

Figure S4, Related to Figure 2.7. Additional Details of the Melanopsin State Model. (A) State diagram (top) and normalized absorption spectra (bottom left) of the biochemically-defined melanopsin states (R, M, and E; Matsuyama et al., 2012). Bottom right: Normalized spectra of the R and E states (solid black and red lines, respectively) plotted with those of the cyan and violet states that we measured electrophysiologically from ipRGCs (dashed black and red lines, respectively; Figure 2.4). The slight deviation in λ_{max} may be due differences in the environments of the purified and native pigments. (B) Time required for the melanopsin state model to reach photoequilibrium as a function of wavelength, normalized to the minimum (which occurs at 456 nm). (C) Time to photoequilibrium as a function of light intensity for 480-nm light. Model parameters are as described for Figure 2.7. (D) Photosensitivity of the M state (normalized to the peak; right axis), compared with the photosensitivity of the M state relative to each of the silent states (i.e., M/R and M/E; left axis), all plotted as functions of wavelength.

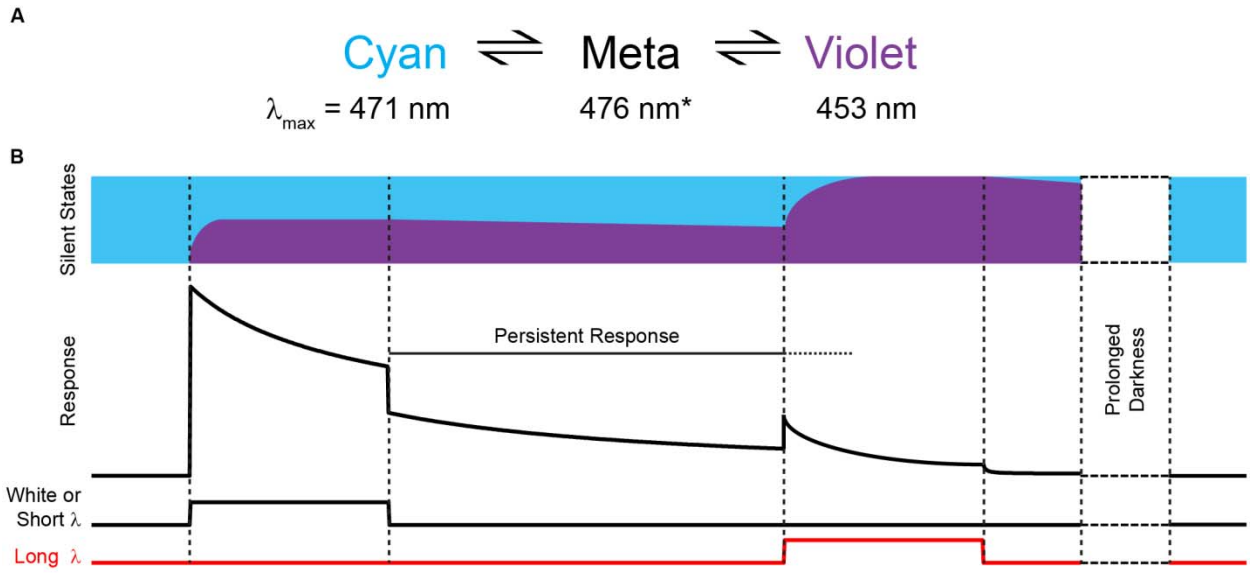

Figure S5. Summary Schematic. (A) State diagram of the three physiologically-defined melanopsin states and their light-driven transitions. The cyan and violet states are silent while the meta state is signaling. The wavelength of peak sensitivity (λ_{max}) of each silent state was measured from ipRGCs in the present study; that of the meta state was measured from purified melanopsin by Matsuyama and colleagues (2012). (B) Diagram illustrating fractional occupancy of the two silent states (top) and the cellular response (middle) produced by visual stimulation with different wavelengths (bottom), as functions of time. The depicted cellular response has features that are not overtly related to state transitions of the pigment, such as transient responses that accompany periods of illumination. Common sources of broadband ("white") light produce occupancy of both cyan and violet states, leading to a modest broadening of ipRGC spectral sensitivity. Monochromatic, short-wavelength illumination has a similar effect. Long-wavelength illumination produces a dominant fraction of the violet state, acutely decreasing the persistent response. Pigment states change gradually between periods of illumination due to dark regeneration. Prolonged darkness is required to fully deactivate the persistent response and restore all melanopsin to the cyan state.

Supplemental Experimental Procedures

Solutions. The intracellular solution for perforated-patch recordings was (in mM): 110 K-Methanesulfonate, 13 NaCl, 2 $MgCl_2$, 10 EGTA, 1 $CaCl_2$, 10 HEPES, 0.1 Lucifer Yellow (dipotassium salt), and 0.125-0.25 amphotericin B. The pH was adjusted to 7.2 with KOH for a final [K+] of 139 mM. Amphotericin B was stored in the dark at -20 °C for several weeks as a 100X stock in DMSO. Amphotericin-containing internal solution was sonicated before each recording. A liquid-junction potential of +7 mV has been corrected (Neher, 1992). The extracellular solution was bicarbonate-buffered Ames' medium, or ionic Ames' medium (in mM): 120 NaCl, 22.6 $NaHCO_3$, 3.1 KCl, 0.5 KH_2PO_4, 1.5 $CaCl_2$, 1.2 $MgSO_4$, 6 glucose, equilibrated with 95% O2 / 5% CO2 (Do et al., 2009). Fast synaptic transmission was blocked in most experiments by adding to the external solution (in mM): 3 kynurenate, 0.1 D,L-AP4, 0.1 picrotoxin, and 0.01 strychnine (Do et al., 2009).

Measurement of Subthreshold Membrane Voltage. Subthreshold membrane voltage was isolated by detecting spikes, excising a 20-ms interval surrounding the peak of each spike, and averaging the remaining voltage within the time window of interest. The decay of the persistent response was measured from subthreshold membrane voltage that was binned in 5-s intervals, to reduce the effect of biological noise.

Measurement of Gradations in Persistent Responses as a Function of Wavelength. Steps of light (60-s duration) were delivered every 280 s and the membrane current averaged from 150-160 s after each pulse. Test steps of various wavelengths alternated with a "reset" step of 560-nm light. The current following 560-nm light is used as a baseline rather than the dark-adapted holding current to correct for any drift over the extended time course of the experiment (>30 min). The persistent response that remains after 560-nm light is estimated to be slightly larger than 3 pA on average. Light intensities for all wavelengths were $1 \times 10^9 - 2 \times 10^9$ photons μm^{-2} s^{-1}, which was sufficient to produce a saturated persistent response at each wavelength.

Analysis in the Linear Range. "Dim-flash" responses are impulse responses. They are obtained in the linear range of the ipRGC intensity-response relation, where the response magnitude scales arithmetically with flash intensity while the response waveform remains invariant (Baylor and Hodgkin, 1973; Do et al., 2009; Do and Yau, 2013). Dim-flash responses are identical in waveform to single-photon responses (Do et al., 2009). Sufficient time was given between dim flashes (35 s at 35 °C and 70 s at 23 °C) for full, observable response decay and recovery from adaptation (Do et al., 2009; Do and Yau, 2013; Wong et al., 2005). For analysis, dim-flash responses were digitally refiltered to 2-10 Hz and resampled at 100 Hz. Baselines, measured in a 1-s window prior to flash onset, were subtracted. Measurements were made from the average of 3-6 responses, to reduce unavoidable Poisson variations in magnitude (Do et al., 2009), and amplitude was calculated as the mean current in a 400-ms window centered on the response peak. Dim-flash sensitivity is the amplitude (in pA) divided by flash intensity (in photons μm^{-2}). For a dark-adapted ipRGC, dim flash responses are evoked by delivery of ~10^5 photons μm^{-2} of 480-nm light (Do et al., 2009; Do and Yau, 2013; Xue et al., 2011); light-adapted ipRGCs require higher intensities (Do and Yau, 2013).

Measurement of Action Spectra. Action spectra were constructed by calculating dim-flash sensitivity for various wavelengths (Baylor and Hodgkin, 1973). Due to the extended time scale of the measurement, sensitivity was normalized to that of a periodic reference wavelength (480 nm) to correct for drift, then normalized to the maximum sensitivity. Action spectra were fit with standard, single-state nomograms (Govardovskii et al., 2000) using least-squares regression with λ_{max} as the only free parameter:

$$N(\lambda) = \frac{1}{\exp[69.7(0.88 - \lambda_{max}/\lambda)] + \exp[28(0.922 - \lambda_{max}/\lambda)] + \exp[-14.9(1.104 - \lambda_{max}/\lambda)] + 0.674}$$

$$+ 0.26 \times \exp[-\left(\frac{\frac{\lambda_{max}}{\lambda} - 189 - 0.315 \times \lambda_{max}}{-40.5 + 0.195 \times \lambda_{max}}\right)^2]$$

The action spectra obtained during ongoing xenon or 440-nm illumination were each fit with a weighted sum of two single-state nomograms, one describing the cyan state (λ_{max} = 471 nm) and the other describing the violet state (453 nm):

$$S(\lambda) = C \times \left(N(\lambda|\lambda_{max} = 471)\right) + V \times \left(N(\lambda|\lambda_{max} = 453)\right)$$

where $N(\lambda)$ are single-state nomograms with the λ_{max} parameter as designated and C and V are coefficients describing the weight of each single-state nomogram (constrained so that neither coefficient is less than 0). Applying this weighted-sum nomogram to the average action spectra measured in darkness (where we expect a dominant cyan state) and atop 600-nm (where we expect a dominant violet state) light yielded cyan/violet fractions of 0.90/0.10 and 0.00/1.00, respectively.

Interpretation of Action Spectra. Because the probability of photon absorption during a dim flash is low, any melanopsin molecule should isomerize only once (Do et al., 2009). In principle, the isomerization could occur from a silent or signaling state and result in activation or deactivation, respectively. Because dim flashes caused no detectable deactivation, isomerization of the signaling state is unlikely to contribute to our spectral measurements. Indeed, the action spectra we obtained for the cyan and violet states were each fit well by a single-state nomogram (Govardovskii et al., 2000; Makino et al., 1999).

The action spectra we measured from ipRGCs do not reflect the tdTomato that is expressed in these cells because these action spectra are well-described by the nomograms of pigments that employ retinaldehyde chromophores (Govardovskii et al., 2000). These nomograms are distinct from the excitation and emission spectra of tdTomato (Shaner et al., 2004). Indeed, electrophysiological measurements of the cellular action spectrum have consistently isolated the melanopsin absorption spectrum regardless of whether the cells expressed melanopsin alone or together with fluorophores that are as spectrally distinct as fluorescein and rhodamine (Berson et al., 2002; Dacey et al., 2005; Qiu et al., 2005; Tu et al., 2005).

Ratio of Sensitivities to 480- and 440-nm Light. The relative sensitivity of ipRGCs to 480- and 440-nm photons was measured from dim-flash responses. Wavelengths were interleaved, and the responses to five 50-ms flashes (separated by 70 s) were averaged for each; either 440- or 480-nm was given first (5 and 4 cells, respectively). This probe series was delivered after prolonged dark adaptation or a step of conditioning light (30 s, 560 nm, 2×10^9 photons μm^{-2} s^{-1}). 560-nm light is predicted to produce a similar

photoequilibrium to 600-nm light (Figure 2.7) but to do so ten-fold faster (Figure S4). Therefore, 560-nm light is preferable for use as a discrete conditioning step to generate a dominant fraction of the violet state. The first two dim flashes after the conditioning step were excluded from analysis because these were diminished by transient adaptation (Do and Yau, 2013; Wong et al., 2005). Measuring dim-flash responses required >10 min after illumination ceased because dim-flash responses are prolonged (i.e., having an integration time of ~20 s at 23 ºC) and need to be averaged to obtain a reliable measurement (due to Poisson variations in their amplitude; Do et al., 2009). Two cells were excluded from analysis because the 480:440 ratio in darkness was <0.95, indicating insufficient dark adaptation.

Comparison of Activation from the Cyan and Violet States. We evoked dim-flash responses atop backgrounds of 440- or 600-nm illumination. To compare these responses, we matched the background intensities to produce a similar level of steady, cellular activation. Because we found the dark-adapted, dim-flash sensitivity of ipRGCs to be 130-fold greater with 440- than 600-nm light, we delivered a background that was 111-fold lower in intensity at 440 than 600 nm; a closer match was not permitted by our optical instruments. The accuracy of matching would be further limited if there were a difference in photosensitivity between the cyan and violet states. Presently this information is not known. Nevertheless, we found that the steady-state photocurrents produced by the 440- and 600-nm backgrounds were similar, regardless of the order in which these backgrounds were given (Figure 2.6, n = 5 cells). The kinetics of dim-flash responses were measured by fitting the average response from each cell (calculated from 7-13 responses) to the convolution of two exponentials, $A(e^{-t/\tau_1} - e^{-t/\tau_2})$, as previously described (Do et al., 2009; Xue et al., 2011).

Supplemental References

Baylor, D.A., and Hodgkin, A.L. (1973). Detection and resolution of visual stimuli by turtle photoreceptors. J. Physiol. 234, 163-198.

Shaner, N.C., Campbell, R.E., Steinbach, P.A., Giepmans, B.N., Palmer, A.E., and Tsien, R.Y. (2004). Improved monomeric red, orange and yellow fluorescent proteins derived from *Discosoma* sp. red fluorescent protein. Nat. Biotechnol. 22, 1567-1572.

Tu, D.C., Zhang, D., Demas, J., Slutsky, E.B., Provencio, I., Holy, T.E., and Van Gelder, R.N. (2005). Physiologic diversity and development of intrinsically photosensitive retinal ganglion cells. Neuron 48, 987-999.

Appendix 2: Fitting the Spectral Sensitivity of Intrinsically Photosensitive Retinal Ganglion Cells

We found that dark-adapted ipRGCs have an action spectrum that is well-described by a single-state nomogram with a λ_{max} of 471 nm (Emanuel and Do, 2015), which agrees with the absorption spectrum of melanopsin's ground state measured biochemically by Shichida and colleagues (467 nm; Matsuyama et al., 2012). However, our spectrum appears to be blue-shifted compared with the consensus view (~480 nm; Lucas et al., 2014), albeit not as far as reported by some studies (Melyan et al., 2005; Newman et al., 2003). These discrepancies in λ_{max} may arise in part from differences in fitting data with nomograms. In Chapter 2 (Emanuel and Do, 2015), we fit the ipRGC spectral sensitivity using a least-squares algorithm on a linear scale (Figure 2.4), which preferentially weights values near the peak of photosensitivity. An alternative method is to fit on a semi-logarithmic scale, which gives more weight to the long-wavelength descent of the spectrum. Because this portion of the spectrum varies with temperature (Luo et al., 2011), and we sought to compare across temperatures within our experiments (23 – 35 ºC) and with those performed by others (as low as 0 ºC for biochemistry; Matsuyama et al., 2012), we used the linear scale.

Indeed, the fit of our data on a semi-logarithmic scale (Figure S2.1; λ_{max} = 492 nm) does not describe the data as well as the fit on the linear scale. This observation suggests that the deviation arises from the long-wavelength portion of the spectrum. In fact, the wavelengths at which the data deviate from the template nomogram on the linear scale are at or longer than the critical wavelength identified by Luo et al. (2011), in which thermal and light energy sum. λ_{max} can also be deduced from the wavelength that corresponds to the half-maximal sensitivity on the long-wavelength descent (Govardovskii et al., 2000); applying this method to our data provides a λ_{max} value (475 nm) that is similar to that from least-squares, linear fitting.

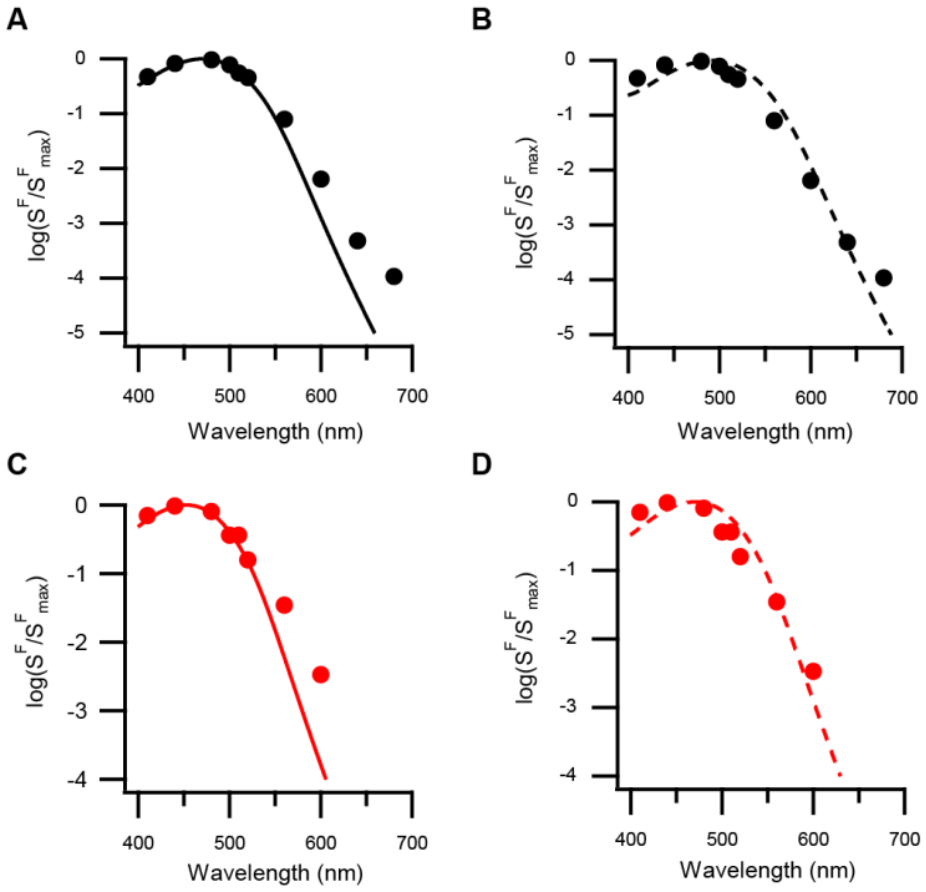

Figure S2.1. Fitting nomograms to action spectra.

(A) Average of action spectra measured from ipRGCs in darkness (markers, same data as Figure 2.4). Line is a single-state nomogram fit using a least-squares algorithm on a linear scale. Fit λ_{max} = 471 nm.

(B) As in (A), but fit was made on a semi-logarithmic scale. Fit λ_{max} = 492 nm.

(C) Average of action spectra measured from ipRGCs during background illumination with 600-nm light (markers, same data as Figure 2.4). Line is a single-state nomogram fit using a least squares algorithm on a linear scale. Fit λ_{max} = 453 nm.

(D) As in (C), but fit was made on a semi-logarithmic scale. Fit λ_{max} = 471 nm.

References

Emanuel, A.J., and Do, M.T.H. (2015). Melanopsin tristability for sustained and broadband phototransduction. Neuron 85, 1043-1055.

Govardovskii, V.I., Fyhrquist, N., Reuter, T., Kuzmin, D.G., and Donner, K. (2000). In search of the visual pigment template. Vis. Neurosci. 17, 509–528.

Lucas, R.J., Peirson, S.N., Berson, D.M., Brown, T.M., Cooper, H.M., Czeisler, C.A., Figueiro, M.G., Gamlin, P.D., Lockley, S.W., O'Hagan, J.B.*, et al.* (2014). Measuring and using light in the melanopsin age. Trends Neurosci. 37, 1-9.

Luo, D.-G., Yue, W.W., Ala-Laurila, P., Yau, K.-W. (2011). Activation of visual pigments by light and heat. Science 332, 1307-1312.

Matsuyama, T., Yamashita, T., Imamoto, Y., and Shichida, Y. (2012). Photochemical properties of mammalian melanopsin. Biochemistry 51, 5454-5462.

Melyan, Z., Tarttelin, E.E., Bellingham, J., Lucas, R.J., and Hankins, M.W. (2005). Addition of human melanopsin renders mammalian cells photoresponsive. Nature 433, 741-745.

Newman, L.A., Walker, M.T., Brown, R.L., Cronin, T.W., and Robinson, P.R. (2003). Melanopsin forms a functional short-wavelength photopigment. Biochemistry 42, 12734–12738.